DISSERTATION

NOWCASTING FOR A HIGH-RESOLUTION WEATHER RADAR NETWORK

Submitted by

Evan Ruzanski

Department of Electrical and Computer Engineering

In partial fulfillment of the requirements

for the Degree of Doctor of Philosophy

Colorado State University

Fort Collins, Colorado

Fall 2010

Doctoral Committee:

Department chair: Anthony Maciejewski

Advisor: V. Chandrasekar

Anura Jayasumana
Paul Mielke
Branislav Notaros

ABSTRACT

NOWCASTING FOR A HIGH-RESOLUTION WEATHER RADAR NETWORK

Short-term prediction (nowcasting) of high-impact weather events can lead to significant improvement in warnings and advisories and is of great practical importance. Nowcasting using weather radar reflectivity data has been shown to be particularly useful. The Collaborative Adaptive Sensing of the Atmosphere (CASA) radar network provides high-resolution reflectivity data amenable to producing valuable nowcasts. The high-resolution nature of CASA data requires the use of an efficient nowcasting approach, which necessitated the development of the Dynamic Adaptive Radar Tracking of Storms (DARTS) and sinc kernel-based advection nowcasting methodology. This methodology was implemented operationally in the CASA Distributed Collaborative Adaptive Sensing (DCAS) system in a robust and efficient manner necessitated by the high-resolution nature of CASA data and distributed nature of the environment in which the nowcasting system operates. Nowcasts up to 10 min to support emergency manager decision-making and 1–5 min to steer the CASA radar nodes to better observe the advecting storm patterns for forecasters and researchers are currently provided by this system. Results of nowcasting performance during the 2009 CASA IP experiment are presented. Additionally, currently state-of-the-art scale-based filtering methods were adapted and evaluated for use in the CASA DCAS to provide a scale-based analysis of nowcasting. DARTS was also incorporated in the Weather Support to Deicing Decision Making

system to provide more accurate and efficient snow water equivalent nowcasts for aircraft deicing decision support relative to the radar-based nowcasting method currently used in the operational system. Results of an evaluation using data collected from 2007–2008 by the Weather Service Radar-1988 Doppler (WSR-88D) located near Denver, Colorado, and the National Center for Atmospheric Research Marshall Test Site near Boulder, Colorado, are presented. DARTS was also used to study the short-term predictability of precipitation patterns depicted by high-resolution reflectivity data observed at microalpha (0.2–2 km) to mesobeta (20–200 km) scales by the CASA radar network. Additionally, DARTS was used to investigate the performance of nowcasting rainfall fields derived from specific differential phase estimates, which have been shown to provide more accurate and robust rainfall estimates compared to those made from radar reflectivity data.

ACKNOWLEDGMENTS

First and foremost I must try to find words to express my deepest and most humble thanks to God for blessing me with my talents, attributes, abilities, and guidance to overcome my short-comings and the many difficult challenges I faced throughout this journey of growth and self-discovery. I also thank Him for guiding me to pursue my studies at Colorado State University amongst amazing colleagues and professors and for the fulfillment I've found from living and working in the Front Range area of Colorado.

My sincerest appreciation goes to Prof. V. Chandrasekar not only for his support of my work and our fruitful discussions, but for his advice, patience with, and belief in me.

I would like to sincerely thank my colleagues Nitin Bharadwaj, Jason Fritz, Joseph Hardin, Minda Le, Sanghun Lim, Matthew Martinez, Vijay Mishra, Cuong Nguyen, Yanting Wang, Gang Xu, and Sean Zhang who have offered their generous technical or non-technical assistance to me in various ways during the course of my studies and to Andrew Crane and the staff of Engineering Network Services who solved many technical computing and network issues to make this work possible.

I also sincerely thank Profs. Anura P. Jayasumana, Paul W. Mielke, Jr., and Branislav Notaros for serving on my graduate committee.

This research was supported by the NSF ITR program and CASA ERC program.

TABLE OF CONTENTS

LIST OF FIGURES

LIST OF TABLES

CHAPTER I. INTRODUCTION

1.1 Introduction

The term "nowcasting" refers to short-term (0–6 h) automated weather forecasting. Nowcasts of high-impact weather events such as flood-producing rains, hail, and snow can be made with sufficient time and space specificity within this time frame such that appropriate action can be taken to effectively mitigate losses of life, property, and time and cost due to transportation delays. Thus the term "nowcasting" emphasizes specificity and short time nature of a weather event forecast (Browning 1982; Wilson 2004).

Modern meteorological radars provide favorable measurement resolution and range for nowcasting. Radar reflectivity or derived products such as Vertically Integrated Liquid (VIL; Greene and Clark 1972; Boudevillain and Andrieu 2003; Smalley et al. 2003) are useful for nowcasting high-impact weather events. While several different types of meteorological radars and radar networks are currently in operation worldwide, the Collaborative Adaptive Sensing of the Atmosphere (CASA) radar network is unique in that it provides high-resolution dual-polarized measurements of the atmosphere close to the ground with suitable spatial extent to facilitate better observation and study of severe weather events. The CASA network consists of four dual-polarized X-band Doppler radar nodes and provides high- resolution reflectivity observations covering an approximate area of 7000 km^2 over central Oklahoma amenable to producing valuable nowcasts.

The high resolution of CASA radar data over a relatively large spatial extent allows for observation of microalpha scale (0.2–2 km) meteorological phenomena including wind circulations, cloud patterns, tornadoes, and deep convection (Orlanski 1975; National Weather Service 2009) and misoscale (0.04–4 km) meteorological phenomena including microbursts and rotation within thunderstorms (Fujita 1981; National Weather Service 2009). While observations of such phenomena are beneficial to operational forecasters and researchers, implementation of an accurate and computationally efficient nowcasting method is required to produce nowcasts useful for operational or research use. A nowcasting method consisting of the Fourier-based Dynamic Adaptive Radar Tracking of Storms (DARTS) algorithm for motion estimation in conjunction with an analytic sinc kernel-based advection scheme has been developed and evaluated for nowcasting and potential inclusion in the CASA radar network with positive results.

1.2 Research challenges and opportunities

Currently in the CASA Distributed Collaborative Adaptive System (DCAS; McLaughlin et al. 2005), radar observations are collected and processed at the local site, namely the Systems Operations Control Center (SOCC) located in Norman, Oklahoma, and sent via a Transmission Control Protocol/Internet Protocol (TCP/IP)-based peer-to-peer file transfer network to a central facility at Amherst, Massachusetts, approximately 2600 km away where the nowcasting software runs. Thus, operational nowcasting in the CASA DCAS provides several unique challenges. The system implementation of a nowcasting method must generate nowcasts of desired lead times before data files containing new observations become available. The system must also be robust to data anomalies such as network latency and unpredictable delays in data transfer leading to

dropped or mistimed data transfer or long periods of inactivity. The nowcasting system must also run on different processing platforms. Thus, the operational nowcasting system in CASA DCAS must use a nowcasting method that is inherently computationally efficient and the implementation of such a method must also be computationally efficient, robust, and portable.

Naturally it is desired to implement the most accurate nowcasting system possible. Selective filtering of precipitation pattern scales depicted by radar observations has been shown in previous research to enhance nowcasting accuracy. One currently operational method filters volatile scales from predicted continental-scale reflectivity observations via a wavelet-based filtering approach (Turner et al. 2004). Another method uses a spatial elliptical filtering procedure applied to High-Resolution VIL (HRVIL; Smalley et al. 2003) fields estimated from WSR-88D observations used as input to a cross-correlation-based nowcasting technique. This filtering method seeks to extract a large-scale precipitation pattern envelope whereby translation due to intensification of precipitation at one end of the pattern and dissipation at the opposite end can be detected (Wolfson et al. 1999). The DARTS model incorporates a provision for Fourier filtering of the observed data sequence used for motion estimation. The determination of the filtering approach or combination of approaches that yields the most accurate nowcasts in the CASA DCAS environment has yet to be determined.

The nowcasting methodology used in CASA DCAS can also be incorporated in other operational decision support systems to improve performance. The Weather Support to Deicing Decision Making (WSDDM; Rasmussen et al. 2001, 2003) system calibrates the *Z-S* equation in real-time to provide snow water equivalent (SWE) nowcasts to support

decisions made by airport managers responsible for determining the type and application frequency of aircraft deicing fluid (Stefl and George 1992). WSDDM is currently deployed at several major airports in the U.S. and uses reflectivity fields observed by a radar or radars covering the airspace over the deployment site as input to a cross-correlation-based nowcasting method currently used to provide reflectivity (Z) nowcasts. These nowcasts are converted to SWE values using the Z-S relationship calibrated by surface SWE measurements (S) and observed reflectivity values most likely producing the surface measurement. It has been observed that this cross-correlation-based nowcasting method is the main source of computational cost in the system and fails to provide accurate motion estimates in the presence of radar data anomalies, specifically artificially stationary regions of reflectivity due to the presence of a zero velocity isodop (i.e., the area of estimated zero velocity caused by the scan radial being perpendicular to the wind direction) resulting from ground clutter mitigation.

The predictability of precipitation patterns observed by meteorological radar is an important concept in the development of effective nowcasting systems by establishing a means to characterize precipitation patterns and features and provide an upper limit on the extent and utility of nowcasting. Previous studies investigating the predictability of precipitation patterns considered continental-scale reflectivity observations (Germann and Zawadzki 2002, 2006) and data collected by a single WSR-88D (Grecu and Krajewski 2000). These studies were practically significant in three ways. First, they provided insight as to what is achievable in terms of nowcasting. Second, they provided a reference against which the progress of any nowcasting technique can be evaluated. Third, they gave insight into the predictability as a function of space and time scales. Such

studies have yet to be extended to investigate the predictability of microscale scale precipitation patterns represented by CASA radar observations.

While nowcasting of precipitation has traditionally been done using radar reflectivity data, research over the last decade indicates that using the specific differential phase (K_{dp}), defined as one-half the range derivative of the two-way differential phase (Φ_{dp}), has several advantages over using reflectivity for estimating rainfall accumulation including being robust to radar calibration error, attenuation, beam blockage, variations in drop size distribution, anomalous propagation, and the presence of dry, tumbling hail. A new method for K_{dp} estimation has been developed (Wang and Chandrasekar 2009) that provides more accurate and robust estimates of K_{dp} relative to previous methods. Such estimates can be converted to rainfall rates using an R-K_{dp} relationship for X-band radar and integrated to produce rainfall accumulation estimates. Studies investigating the feasibility of nowcasting rainfall fields based on K_{dp} estimates calculated in this manner have yet to be performed.

1.3 Research objectives

This research aimed to address the specific challenges and opportunities associated with nowcasting in CASA DCAS introduced in the preceding subsection. The DARTS and sinc kernel-based advection methodology was implemented operationally in the CASA DCAS in a robust and efficient manner necessitated by the high-resolution nature of the data and distributed nature of the environment in which the nowcasting system operates. Nowcasts up to 10 min to support emergency manager decision-making and 1–5 min nowcasts to steer the CASA radar nodes to better observe the advecting storms for forecasters and researchers are currently provided by this system. Additionally, the

currently state-of-the-art scale-based filtering methods described in the preceding subsection were evaluated for potentially improving the operational performance of nowcasting in CASA DCAS. DARTS was also incorporated in the WSDDM system to provide more efficient SWE nowcasts relative to the radar-based nowcasting method currently used in the operational system.

The DARTS and sinc kernel-based nowcasting methodology was also used as a tool to study the short-term predictability of precipitation patterns represented by reflectivity fields observed at microalpha to mesobeta scales by the CASA radar network. Additionally, the DARTS and sinc kernel-based nowcasting methodology was used to investigate the extent of nowcasting rainfall fields based on K_{dp} estimates and an R-K_{dp} relationship applicable for X-band radar where nowcasts were verified by rain gauge observations.

1.4 Organization of the dissertation

This dissertation is organized as follows.

Chapter II introduces current nowcasting approaches and a presents a review of current methods. The DARTS motion estimation and sinc kernel-based advection methods are introduced and placed in the context of other nowcasting approaches.

Chapter III presents the rationale behind using an area-based nowcasting method in CASA DCAS, discusses the concepts of Eulerian and Lagrangian persistence, and describes the DARTS and sinc kernel-based advection methods in detail.

Chapter IV describes the operational implementation of nowcasting in the CASA DCAS and presents a performance assessment of successful operation during the 2009 CASA Integrative Project 1 (IP1) experiment (Chandrasekar et al. 2010).

Chapter V describes the methodology and results of an evaluation of Fourier, wavelet, and elliptical spatial filtering approaches seeking to improve nowcasting performance within the CASA DCAS.

Chapter VI describes the WSDDM system and presents results demonstrating the successful implementation of DARTS in WSDDM to provide more accurate and efficient SWE nowcasts. Radar data collected by the KFTG WSR-88D located outside Denver, Colorado, and surface measurements from a World Meteorological Organization (WMO) Geonor Double Fence Intercomparison Reference (DFIR) standard reference gauge located at the National Center for Atmospheric Research (NCAR) Marshall Field Site outside of Boulder, Colorado, are used for evaluation.

Chapter VII presents a study of the short-term predictability of precipitation patterns observed at microalpha (0.2–2 km) to mesobeta (20–200 km) scales by the CASA IP1 network. In this context, results from a preliminary investigation of the dependence of predictability on precipitation event type are presented, the spatio-temporal scale dependence of predictability is quantified, an estimated upper-bound on nowcasting using the Lagrangian persistence paradigm represented by the DARTS and sinc kernel-based nowcasting methodology is established, and a connection of predictability to larger scales is made.

Chapter VIII exhibits an evaluation of the DARTS and sinc kernel-based methodology to nowcast rainfall fields based on K_{dp} estimates made using a new algorithm (Wang and Chandrasekar 2009). Short-term predictability characteristics of such fields are also investigated.

Chapter IX summarizes the dissertation and presents suggestions for future work.

CHAPTER II. BACKGROUND

2.1 Overview of current nowcasting methods

In current operational nowcasting systems, extrapolation of radar echoes, satellite imagery of clouds, and/or lightning location data is the primary mechanism used to generate forecasts in the 0–3 h time frame, with such forecasts gradually combined with numerical weather prediction (NWP) model forecasts made during the 3–6 h forecast lead time period (Bowler et al. 2004; Dupree et al. 2009; Li and Lai 2004; Wolfson et al. 2008). The underlying assumption that relatively predictable translation of precipitation patterns dominates relatively less predictable growth and decay of precipitation intensity forms the basis for using extrapolation-based nowcasting methods for such short prediction periods. Although studies have shown the accuracy of extrapolation-based nowcasts decreases rapidly during the 0–1 h forecast window with a rate closely related to the scale of the precipitation pattern and the associated forcing mechanism (Browning 1980; Wilson et al. 1998), extrapolation-based nowcasts of radar data up to 30 min have lead to significant improvement in warnings and advisories resulting in substantial savings of life and property (National Research Council 1995).

Currently, strictly radar-based nowcasting methods belong to one of four general categories (or a combination thereof): area-based, object-based, statistical, and probabilistic approaches. These categories and methods are introduced in Figure 1, summarized in Figure 2, and further explained in this section.

Area-based nowcasting approaches estimate a motion vector field over the entire radar observation domain and have shown effectiveness in estimating translation of a variety of precipitation pattern types. Additionally, the motion vector fields generated by area-based nowcasting methods not only provide a means for tracking internal storm motions (e.g., rotation and vortices) but also vector convergence (representing areal decay) and divergence (representing areal growth). Thus, area-based nowcasting methods provide a means to track storm motion and require a separate advection algorithm to suitably (and recursively) advect the latest observed (or predicted) radar data field according to the estimated motion vector field to produce future estimated data fields up to a desired lead time (Sawyer 1963; Robert 1981; Rood 1987; Germann and Zawadzki 2002). The estimation of a distributed motion vector field and the advection process can make such approaches computationally expensive. Examples of area-based, image template-matching methods include Tracking of Radar Echoes by Correlation (TREC; Rinehart and Garvey 1978; Rinehart 1981; Tuttle and Foote 1990; Chornoboy et al. 1994), where locations maximum cross-correlation coefficients between subgrids of successive radar data fields are determined to estimate motion, COntinuity of TREC vectors (COTREC; Li et al. 1995), where a variational constraint is applied to smooth the TREC-derived motion vector field, and the Growth and Decay Storm Tracker (GDST; Wolfson et al. 1999), where radar data fields are pre-filtered with a directional elliptical filter to separate precipitation pattern envelope motion from internal motion prior to estimation using a cross-correlation-based approach.

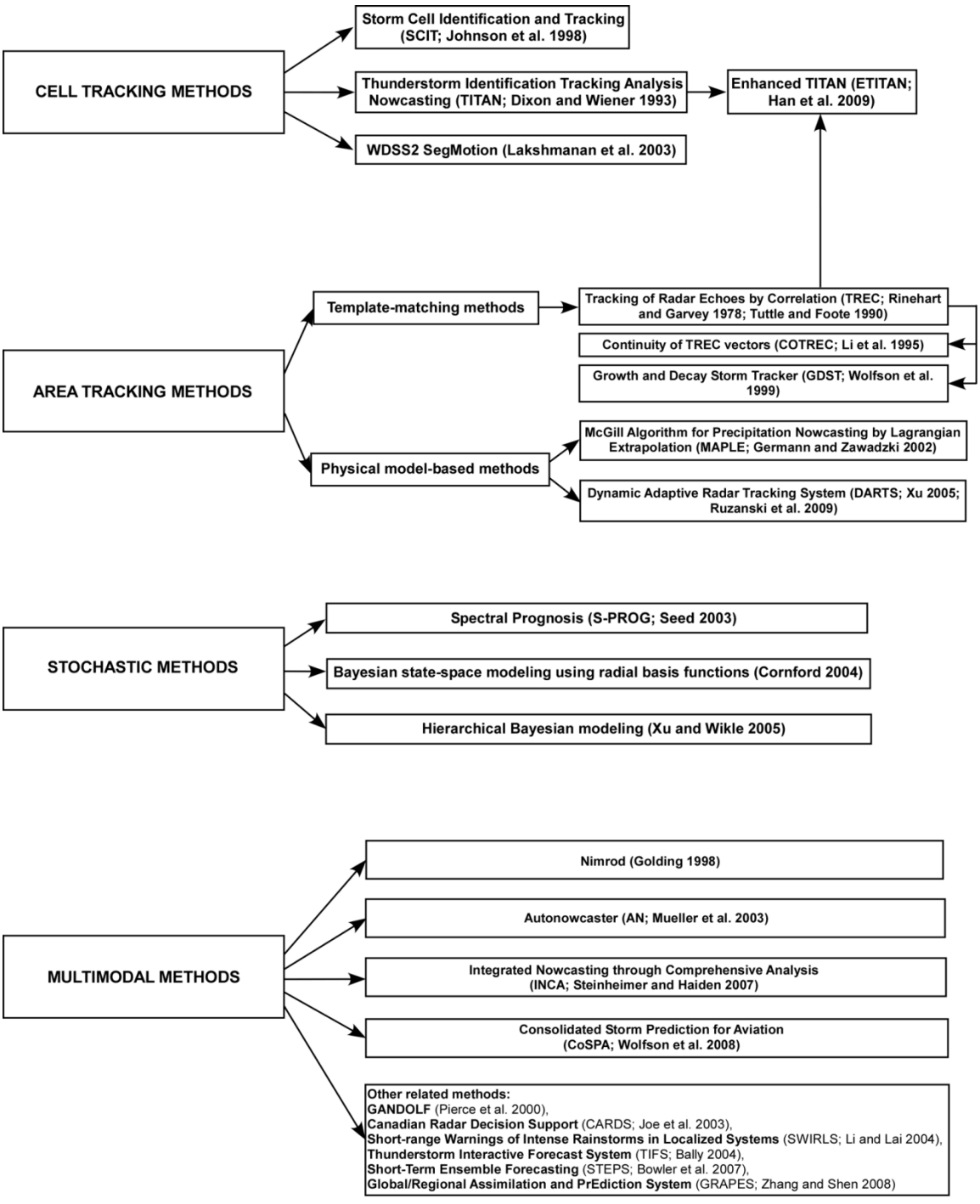

Figure 1. Overview of current nowcasting methods.

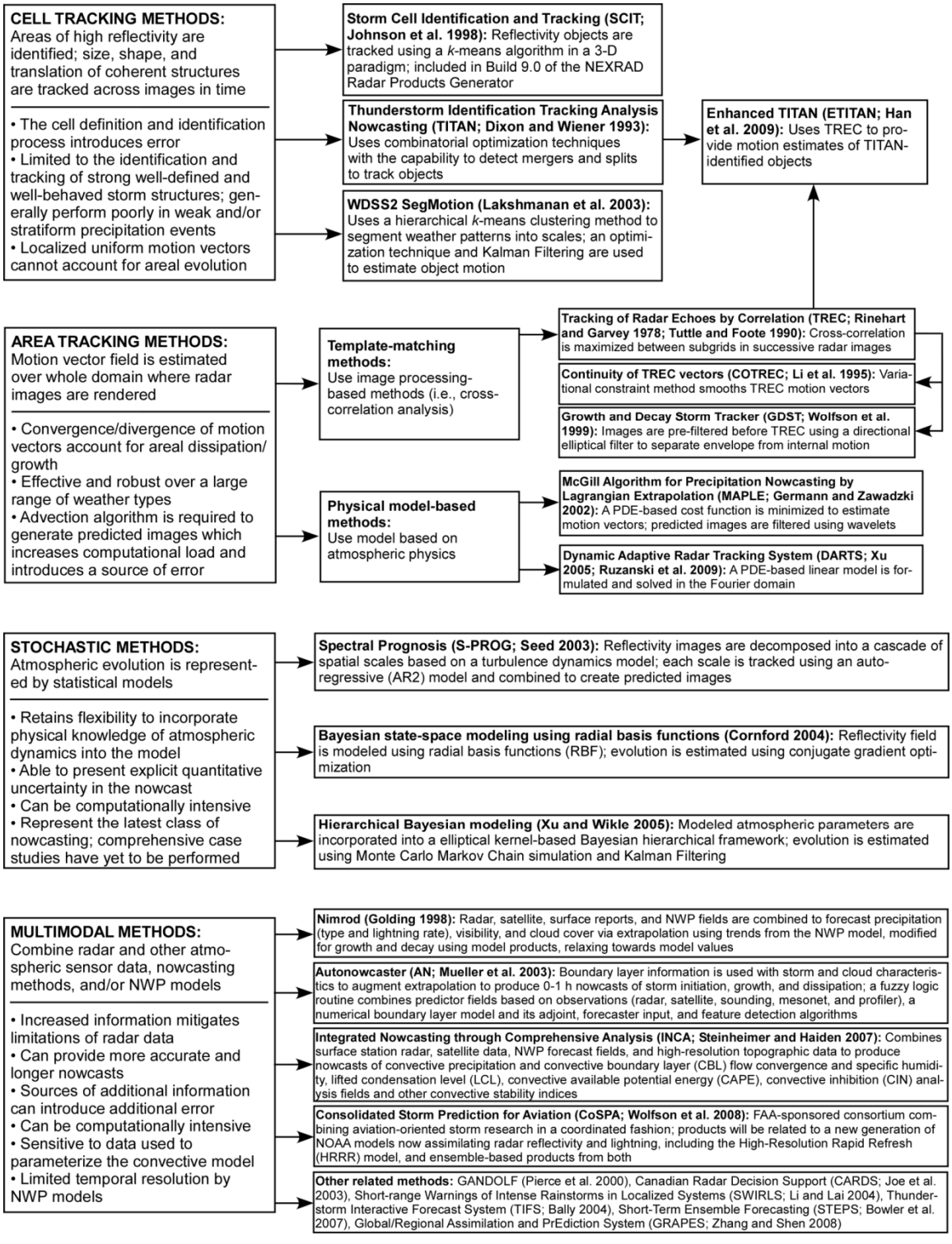

Figure 2. Summary of current nowcasting methods.

An example of an area-based approach predicated on an atmospheric model is the McGill Algorithm for Precipitation Nowcasting by Lagrangian Extrapolation (MAPLE; Germann and Zawadzki 2002), where a cost function based on atmospheric physics is minimized to estimate the motion vector field and a wavelet-based filtering method is applied to the resulting predicted reflectivity fields to remove unpredictable scales (Turner et al. 2004).

Object-based nowcasting schemes attempt to identify areas of high reflectivity in radar observations and track the size, shape, and translation of coherent features in time across successive observations. Object-based nowcasting methods have been shown to work very well with strong, well-defined and well-behaved storm structures. Additionally, the object identification process introduces error. Examples of current object-based nowcasting methods include the Thunderstorm Identification Tracking, Analysis, and Nowcasting algorithm (TITAN; Dixon and Wiener 1993), where combinatorial optimization techniques with the capability to detect cell mergers and splits are used to track reflectivity objects, the Storm Cell Identification and Tracking (SCIT; Johnson et al. 1998) method, where reflectivity objects are tracked using a *k*-means algorithm in a 3D paradigm, TRACE3D (Handwerker 2002), where a two-stage cell detection method is combined with a tracking procedure similar to that used in SCIT to account for cell splitting and merging and track crossings, and the approach used in the Weather Decision Support System 2 (WDSS2) "SegMotion" module (Lakshmanan et al. 2003), where a hierarchical *k*-means algorithm is used to identify reflectivity objects in a 3D paradigm and an optimization technique with Kalman filtering are used to estimate object motion. The Enhanced TITAN method (ETITAN; Han et al. 2009) combines the TREC and TITAN approaches.

Nowcasting methods also exist where atmospheric evolution is represented by statistical models able to incorporate knowledge of atmospheric dynamics. Radar reflectivity fields are modeled as random processes using radial (Cornford 2004) or parameterized elliptical basis functions (Xu et al. 2005; Fox and Wikle 2005). Future fields are then predicted within a Bayesian hierarchical model framework using Markov Chain Monte Carlo (MCMC; Jones and Hobert 2002) simulation techniques where the mean field of the resulting posterior distribution is taken to be the nowcast and the standard deviation field the measure of forecast uncertainty. Physical characteristics of precipitation patterns are modeled as parameters for which a range is pre-selected based on meteorological expertise. Although each level of the Bayesian hierarchical model can be parameterized, computational complexity of such models is high and a comprehensive evaluation of such methods has yet to be performed. Another statistical approach is called Spectral Prognosis (S-PROG; Seed 2003), where a radar reflectivity field is decomposed into a cascade of random fields using a notch filter in the frequency domain. Nowcasts are generated by extrapolating each level in the cascade of precipitation scales by a single motion vector estimated by maximizing cross-correlation over similar levels in successive reflectivity fields and by modeling the temporal development at each level in the cascade using a second-order autoregressive (AR) model. Radar-based nowcasting models based on Artificial Neural Networks (ANN) also exist (Otsuka et al. 1999; Grecu and Krajewski 2000; Montanari et al. 2006; Tomasetti et al. 2008; Dutta et al. 2010).

Germann and Zawadzki (2004) introduced a probabilistic nowcasting approach where the probability of encountering a precipitation rate above a certain threshold at each point in the field of radar coverage is computed for a given lead time. For example, it may be

quite certain a thunderstorm will develop but the exact future position in time and space is less certain. In this case, a probability forecast can be generated. Such probability forecasts are generally complementary to predictions of expected point rainfall rates and the requirements for a specific application or end-user will dictate the utility of probability forecasts. Similar probabilistic nowcasting methods have been proposed by other researchers (Megenhardt et al. 2004; Schmeits et al. 2008; Dance et al. 2010).

Other current nowcasting methods combine radar with other atmospheric sensor data, NWP models, or nowcasting methods. The Nimrod (Golding 1998) system combines radar, satellite, surface reports, and NWP model fields to forecast precipitation (type and lightning rate), visibility, and cloud cover via extrapolation using trends from the NWP model, modified for growth and decay using model products, relaxing towards model values with extended lead time. The Autonowcaster (AN; Mueller et al. 2003) uses boundary layer information with storm and cloud characteristics to augment extrapolation to produce 0–1 h nowcasts of storm initiation, growth, and dissipation. A fuzzy logic routine combines predictor fields based on observations (radar, satellite, sounding, mesonet, and profiler), a numerical boundary layer model and its adjoint, forecaster input, and feature detection algorithms. The Integrated Nowcasting through Comprehensive Analysis (INCA; Steinheimer and Haiden 2007) system combines surface station radar and satellite data, NWP model forecast fields, and high-resolution topographic data to produce nowcasts of convective precipitation, convective boundary layer (CBL) flow convergence, specific humidity, lifted condensation level (LCL), convective available potential energy (CAPE), convective inhibition (CIN) analysis fields, and other convective stability indices. The Consolidated Storm Prediction for Aviation (CoSPA;

Wolfson et al. 2008) is an FAA-sponsored consortium combining aviation-oriented storm research in a coordinated fashion whose products will be related to a new generation of National Oceanic and Atmospheric Association (NOAA) models now assimilating radar reflectivity and lightning, including the High-Resolution Rapid Refresh (HRRR; Weygandt et al. 2009) model, and ensemble-based products from both. Other such multi-modal systems include Adjustment of Rain Models with Radar (ARMOR; DuFran et al. 2009), Atmospheric Motion Vector (AMV; Hohti et al. 2000), Canadian Radar Decision Support (CARDS; Joe et al. 2003), GANDOLF (Pierce et al. 2000), Global/Regional Assimilation and PrEdiction System (GRAPES; Zhang and Shen 2008), Short-range Warnings of Intense Rainstorms in Localized Systems (SWIRLS; Li and Lai 2004), Short-Term Ensemble Forecasting (STEPS; Bowler et al. 2007), Thunderstorm Interactive Forecast System (TIFS; Bally 2004), Thunderstorms Radar Tracking (TRT; Hering et al. 2004) system, and the nowcasting system developed by the Czech Hydrometeorological Institute (CHMI; Novák 2007). Despite the relative complexity of such systems, their performance has been shown to be mixed (Pierce et al. 2004; Wilson et al. 2004; Wilson 2009).

Motivated by the ability to estimate motion vectors over the entire space where radar observations are rendered to provide deterministic nowcasts desired by end-users, an efficient area-based nowcasting method was developed for use in the CASA nowcasting system. The area-based Dynamic and Adaptive Radar Tracking of Storms (DARTS) nowcasting method represents the general continuity equation describing the flux and evolution of an observed precipitation pattern as a discrete spatiotemporal linear model that is formulated in the Fourier domain and solved using linear least-squares estimation.

Thus DARTS is “dynamic” in the sense it is built upon a dynamic equation and is considered “adaptive” because the smoothness of the estimated motion field, tracking scale, and computational efficiency are regulated by truncating model coefficients. Fourier low-pass filtering can be conveniently implemented by truncating the number of these coefficients in the model.

2.2 Advection in nowcasting

Development of accurate and computationally efficient advection methods has historically been a major area of research in fluid dynamics, atmospheric transport, and chemistry models and finds an important application in nowcasting (Rood 1987; Staniforth and Cote 1991). In its simplest form (i.e., “straight” advection) the motion vector field forms a mapping where data points in the current field are simply moved to locations designated by the estimated motion vectors to form the predicted data field. The problem with this simple method is the condition where the mapping described by the vectors in a distributed motion vector field is not one-to-one and dictates that two points in the current field occupy the same location in the predicted field. This creates a situation of two overlapping data points as well as an empty data point in the predicted field. This is illustrated in Figure 3, which shows the motion vectors, (U_1,V_1) and (U_2,V_2), both direct values (gray) at points P_1 and P_2 to Q_1. This creates an overlap (black) of values at Q_1 and vacancy (white) at Q_2. Thus, an advection algorithm is needed to smooth values where vector convergence exists (i.e., overlapping data) and interpolate regions of missing data where vector divergence exists.

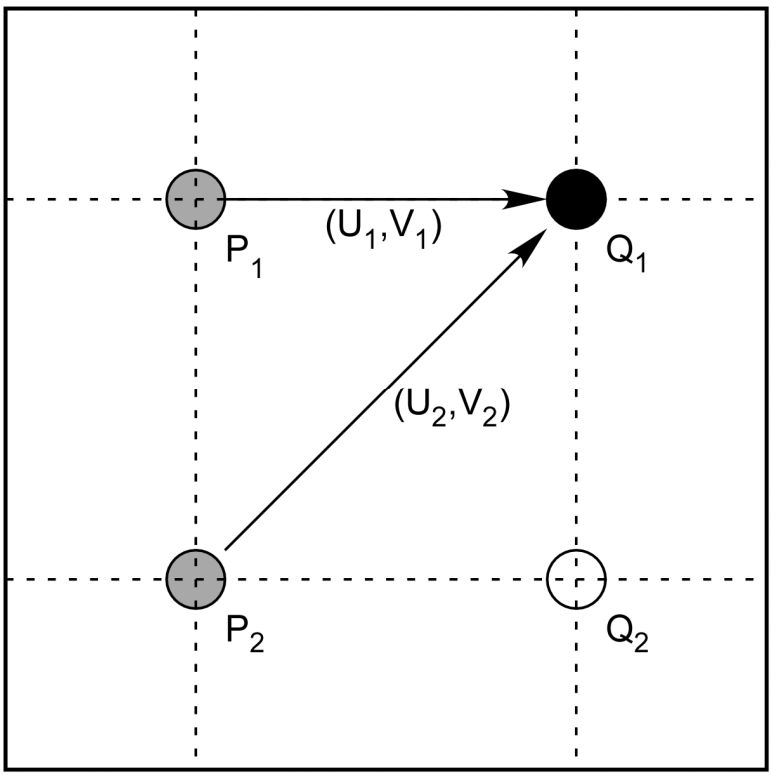

Figure 3. Illustration of the advection problem.

Germann and Zawadzki (2002) categorized advection schemes as forward (where data are advected forward in time and downstream in space), backward (where the origin of a data point predicted to occupy a certain location is found by a backward search), constant vector (where motion vectors are extended to match the desired lead time), and semi-Lagrangian (where data points in predicted data fields are traced along trajectories of motion vector fields). Therefore, in a forward advection scheme, the advected value is redistributed to the neighboring grid points while in a backward scheme interpolation is required to determine the value at the predicted origin. Both redistribution and interpolation result in a loss of power at small scales. Additionally, only forward schemes maintain mass conservation (i.e., the mean of the advected field is conserved). The challenge associated with forward schemes is choosing the optimum radius of influence

when redistributing (spreading) the advected value to the neighboring grid points. The radius must be large enough to smooth ripples caused by divergence, but small enough to limit the loss of power at small scales. When using high-resolution CASA data, the semi-Lagrangian scheme is preferred over the constant vector scheme to adequately represent prediction of internal rotations within precipitation patterns.

The two most common problems in numerical advection schemes are numerical diffusion and numerical dispersion. Numerical diffusion refers to the loss of peak power resulting from the redistribution or the interpolation, for example, in the semi-Lagrangian scheme (Ostiguy and Laprise 1990; Germann and Zawadzki 2002) and causes a loss of power at small scales. Numerical dispersion refers to the phenomena of oscillations resulting from different phase speeds among different Fourier components in numerical schemes and leads to erroneous variance in the advected field (Ostiguy and Laprise 1990).

Several types of advection methods are used in current nowcasting systems. The MAPLE nowcasting method (Germann and Zawadzki 2002) uses a modified semi-Lagrangian backward advection scheme that allows for rotation, is nearly conservative in mass, and limits the loss of power at small scales that results from interpolation. The SWIRLS nowcasting method (Li and Lai 2004) uses a two-time-level semi-Lagrangian method described by Staniforth and Cote (1991) exhibiting unconditional stability, absence of serious dispersion effects, and computational efficiency. The basic idea of the method is to temporally extrapolate the precipitation field to time $t + \Delta_t/2$, where Δ_t is the time spacing between data frames, using the motion vector fields derived at times t and $t - \Delta_t$ using two iterations to solve a displacement equation via linear interpolation for the first half-step and cubic interpolation for the second half-step. The advection algorithm

used in the CoSPA system (Dupree et al. 2009) uses two steps to advect separate scales. First, semi-Lagrangian advection is applied according to the small-scale motions (cell and envelope), and then an Eulerian (i.e., constant vector) advection step is applied according to the synoptic scale motion. For the small-scale step, the synoptic motion is subtracted from the cell- and envelope- scale motion and the resulting field is applied in a pseudo-Lagrangian sense to the data field. The cell-scale and envelope-scale motion vectors are used out to lead times of 30 and 90 min, respectively. Because the cell- and envelope-scale motion estimates don't accurately represent motion at longer time scales, the cell and envelope scale vectors are reduced over time up to a 90-min lead time. Once the final lead time is reached, the Eulerian step is applied where data are advected using the synoptic-scale motion vectors.

An efficient advection technique based on a sinc kernel expansion has been developed for use within the CASA nowcasting system. This scheme belongs to the forward semi-Lagrangian class of advection schemes and is similar to the spectral and pseudo-spectral schemes using functional expansions (Germann and Zawadzki 2002) which have been shown to provide the highest degree of accuracy at the cost of more computational expense and difficulties associated with the Gibbs phenomenon. The DARTS and sinc kernel-based advection methodology facilitates accurate and efficient predictions of storm motion, areal evolution, and position using high-resolution data in the CASA DCAS. A more detailed presentation on these approaches is given in the next section.

CHAPTER III. CASA NOWCASTING METHODOLOGY

3.1 Selection of an area-based nowcasting approach

Storm motion is driven by winds at some steering level and this motion is well captured by tracking radar echoes using a nowcasting algorithm that describes motion of the radar data field by a distributed motion vector field where rotation, stretching, and shearing of steering level winds resulting in changes in echo patterns can be observed. Storms also propagate through development and dissipation (i.e., when propagation occurs through new development of convection at the front of the system while there is dissipation at the rear, the result is an apparent displacement) that is also well captured by such a nowcasting method. If this propagation is systematic and relatively persistent, the resulting motion vector field will show skill in nowcasting based on this motion. What is not captured is neither new development of convection in a region, separate from the old pattern where none was present before nor the dissipation of entire regions of precipitation. Thus, Lagrangian persistence, in the sense used here could include a good deal of systematic and persistent growth and decay and the degree that this is effective depends on the skill of the nowcasting algorithm (Germann et al. 2006).

Grecu and Krajewski (2000) found that larger-scale precipitation features were more persistent in both in Eulerian and Lagrangian systems of reference than smaller scales. However, in time, the mass distribution within such features was shown to change rather quickly. Their results showed reasonable nowcasting skill for a lead time of 1 h relative

to 30 min when using WSR-88D data degraded to 4 km resolution. One hour was shown to be longer than the lifetime of an individual storm cell, which is generally less than 30 min. This suggests a complex interaction among storm cells responsible for the mass organization in large-scale precipitation volumes. That is, a cell dying in less than 30 min at a certain location must be accompanied by storm intensification at some relatively close location within the resolution of the data to maintain predictability. Even in the case of complex, multicell storms (Weisman and Klemp 1986), changes in small scale features not expected to show predictability in terms of nowcasting skill beyond 30 min were shown to be strongly coupled at larger scales where the predictability extended over longer time scales.

Area-based nowcasting methods produce a distributed motion vector field and are capable of providing useful predictions of areal growth and decay of precipitation patterns, a capability desired by the users of the CASA nowcasting system. Necessary conditions for useful performance of this capability include the presence of such evolution in the observed data used to make predictions and that such observed evolution is relatively consistent. Thus, the distributed motion vector field generated by area-based nowcasting methods not only provides a means for tracking internal storm motions (e.g., rotation and vortices) but vector convergence within the vector field is a means to represent areal decay and vector divergence is a means to represent areal growth. Such capability depends on the radar coverage area and the resolution of the motion vector field. Current cell tracking methods are inherently limited by the identification of such cells and the ability to estimate the motion of only the centroid of such cells. This precludes the ability to estimate areal growth and decay in the manner described.

Additionally, area-based nowcasting methods are able to account for the complex interactions between neighboring smaller-scale features by the distributed motion vector field they produce. Thus, an accurate and efficient area-based nowcasting method was chosen for use in the CASA nowcasting system and for this research.

3.2 Eulerian and Lagrangian persistence

The term *Eulerian persistence* (or simply *persistence* as used throughout this work) refers to keeping the most recent observation frozen in space and considering it as all predictions up to a desired lead time. This is shown mathematically as (Zawadzki 1973)

$$\hat{\Psi}(t_0 + \tau, \mathbf{x}) = \Psi(t_0, \mathbf{x}), \tag{3.1}$$

where $\Psi(t_0, \mathbf{x})$ is the observed data field, t_0 is the start time of the forecast, τ is the forecast lead time, $\mathbf{x}$ is the position, and $\hat{\Psi}(t_0 + \tau, \mathbf{x})$ is the forecasted data field at time $t_0 + \tau$. Eulerian persistence represents the simplest forecast and is typically used a reference for more sophisticated nowcasting methods (Pierce et al. 2004; Ebert et al. 2004).

A forecast in which the precipitation field is advected by an estimated velocity (motion vector) field, leaving the total intensity unchanged, is referred to as *Lagrangian persistence*. In other words, Lagrangian persistence refers to keeping the last estimate of motion constant and considering the latest observation (and subsequently prediction) advected according to this motion estimate as predictions up to a desired lead time, shown by (Zawadzki 1973)

$$\hat{\Psi}(t_0 + \tau, \mathbf{x}) = \Psi(t_0, \mathbf{x} - \boldsymbol{\alpha}), \tag{3.2}$$

where $\boldsymbol{\alpha}$ is the estimated displacement vector. In the constant-vector advection scheme, the displacement vector is shown to be

$$\boldsymbol{\alpha} = \tau \cdot \mathbf{u}(t_0, \mathbf{x}_p), \tag{3.3}$$

where $\mathbf{u}(t_0, \mathbf{x}_p)$ is the echo motion at the grid point p and τ is the forecast lead time. Thus, the constant-vector approach uses one constant translation vector for each grid point and does not allow for rotation. To overcome this drawback, a semi-Lagrangian scheme can be used where the advection is divided into N steps of length Δt, with $N\Delta t = \tau$, and for each time step $\boldsymbol{\alpha}$ is iteratively determined and represented by

$$\boldsymbol{\alpha} = \Delta t \cdot \mathbf{u}\left(t_0, \mathbf{x} - \frac{\boldsymbol{\alpha}}{2}\right), \tag{3.4}$$

starting with $\alpha = 0$. The final displacement vector is the sum of the N vectors of the individual time steps. Thus in the semi-Lagrangian scheme the trajectory of a data point is determined by following the motion vectors either upstream or downstream assuming stationarity, that is $\mathbf{u}(t, \mathbf{x}) = \mathbf{u}(t_0, \mathbf{x})$. In meteorological situations where rotation is not negligible and the shape of the precipitation pattern must be conserved in the presence of such rotation, semi-Lagrangian advection is obviously preferred.

Eq (3.1) can be expressed in differential form using the 2D conservation equation of Ψ, as

$$\frac{\partial u\Psi}{\partial x} + \frac{\partial v\Psi}{\partial y} + \frac{\partial \Psi}{\partial t} = \frac{d\Psi}{dt}. \tag{3.5}$$

Neglecting the compressibility term, $\Psi(\partial u/\partial x + \partial v/\partial y)$, (Acheson 1990) gives

$$u\frac{\partial \Psi}{\partial x} + v\frac{\partial \Psi}{\partial y} + \frac{\partial \Psi}{\partial t} = \frac{d\Psi}{dt}. \tag{3.6}$$

In the Eulerian persistence paradigm, the local rate of change, $\partial\Psi/\partial t$, is set to zero. In the Lagrangian persistence paradigm, the total intensity is unchanged, represented mathematically by

$$u\frac{\partial \Psi}{\partial x} + v\frac{\partial \Psi}{\partial y} + \frac{\partial \Psi}{\partial t} = 0 \text{ or} \tag{3.7}$$

$$\mathbf{v} \cdot \nabla \Psi + \dot{\Psi} = 0, \tag{3.8}$$

where $\mathbf{v} = (u, v)$.

Additionally, intensification and dissipation of intensity can be accounted for by including a source/sink term, $S = d\Psi/dt$, and transformation (e.g., filtering or spatial averaging) of Ψ, $\tilde{\Psi}$, can be included in Eq (3.2), shown as

$$\hat{\Psi}(t_0 + \tau, \mathbf{x}) = \tilde{\Psi}(t_0, \mathbf{x} - \boldsymbol{\alpha}) + S(t_0, \mathbf{x} - \boldsymbol{\alpha}) \tag{3.9}$$

and subsequently shown in Eq (3.6).

The inclusion of the S-term in the nowcasting model is discussed in the next section.

3.3 Nowcasting growth and decay of precipitation intensity

While both cell-based and area-based nowcasting methods can predict short-term growth and decay of precipitation intensity based on intensity trends in past radar observations, studies have shown that doing so does not provide significant improvement in nowcasting performance. The study performed by Tsonis and Austin (1981), which investigated the use of several statistical regression techniques to track intensity growth and decay trends in precipitation cells, showed that extrapolating such trends in growth and decay provided no improvement in nowcasting performance using a cross-correlation tracking method to extrapolate rainfall fields estimated from reflectivity data collected by a ship-borne radar (4 km/5 min resolution) when compared to solely nowcasting translation for lead times out to 75 min This assertion was supported in a more recent study performed by Wilson, et al. (1998) using TITAN and KFTG Weather Surveillance Radar-1988 Doppler (WSR-88D) data. Li et al. (1995) did show some skill in nowcasting

growth and decay trends for up to 20 min using the TREC method and data from 2 storm cases observed in complex orography over the Swiss Alps. However, the authors also state such a small sample set cannot be used to generalize such results.

The study by Grecu and Krajewski (2000) examined the use of a neural network-based precipitation intensity growth and decay tracking method applied to approximately one year of WSR-88D data to make nowcasts up to 3 h into the future. They also found no improvement was gained by nowcasting evolution based on past radar observations. Like earlier studies, they found an extrapolative nowcasting scheme should consider advection but that statistical modeling of growth and decay of precipitation patterns using neural network-based methods showed no measurable improvement in nowcasting performance. Their study focused primarily on radar echoes of weak to moderate intensity (i.e., 15–25 dBZ).

Montanari et al. (2006) evaluated neural network and AR models to represent storm evolution using rainfall fields estimated from radar observations (1 km/15 min resolution) covering an area of 256 km × 256 km collected during eight rainfall events (approximately 26 h) over Northern Italy. They found using ANN and AR techniques in addition to Lagrangian persistence did not provide an appreciable improvement of the forecasts for lead times of 15–60 min and varying grid spacing from 1–30 km.

Germann et al. (2006) stated a compromise must be made between the desire of capturing as much of growth and dissipation as possible and the stability of the motion vector field. Too much sensitivity to growth and dissipation of intensity may result in decrease of skill if the captured growth and dissipation is not persistent. Since most of the growth and dissipation is not persistent over short time scales, too much sensitivity may

improve the very short term nowcasting but degrade longer term performance. The period over which the motion vector field is determined and the resolved scales of the motion field determine the compromise. Germann and Zawadzki (2002) considered the inclusion of a source-sink term in the Variational Echo Tracking (VET; Laroche and Zawadzki 1994) nowcasting model using the Lagrangian persistence paradigm to study the predictability of continental-scale radar data. They concluded that the inclusion of the source-sink term provided mixed and inconsistent results and did not consider the source-sink term in their analysis.

Similar results were observed when including such capability in the DARTS and thus the provision for nowcasting growth and decay of precipitation intensity was not considered in the operational nowcasting implementation or research.

3.4 The Dynamic Adaptive Radar Tracking of Storms algorithm

The DARTS nowcasting algorithm is built upon the general continuity equation modified for nowcasting describing the flux and evolution of a precipitation pattern represented by a temporal sequence of radar reflectivity fields, $F(x, y, t)$, given by (Jacobson 2005)

$$\frac{\partial}{\partial t}F(x,y,t) = -U(x,y)\frac{\partial}{\partial x}F(x,y,t) - V(x,y)\frac{\partial}{\partial y}F(x,y,t) + S(x,y,t), \tag{3.10}$$

where $F(x, y, t)$ is the sequence of radar reflectivity fields, $U(x, y)$ is the east-west component of the velocity field, $V(x, y)$ is the north-south component of the velocity field, and the source-sink term, $S(x, y, t)$, includes additive evolutionary mechanisms such as growth and decay of intensity. DARTS estimates precipitation pattern motion in terms of

a motion vector field consisting of components $U(x, y)$ and $V(x, y)$ by representing (3.10) as a discrete spatiotemporal linear model, given by (Xu and Chandrasekar 2005)

$$
\begin{aligned}
& k_t F_{\mathrm{DFT}}(k_x, k_y, k_t) = \\
& -\left[\frac{1}{N_x N_y}\right] \sum_{k'_x = N_x^-}^{N_x^+} \sum_{k'_y = N_y^-}^{N_y^+} \left[\frac{U_{\mathrm{DFT}}(k'_x, k'_y)}{T_x / T_t}\right] \left(k_x - k'_x\right) F_{\mathrm{DFT}}(k_x - k'_x, k_y - k'_y, k_t) \\
& -\left[\frac{1}{N_x N_y}\right] \sum_{k'_x = N_x^-}^{N_x^+} \sum_{k'_y = N_y^-}^{N_y^+} \left[\frac{V_{\mathrm{DFT}}(k'_x, k'_y)}{T_y / T_t}\right] \left(k_y - k'_y\right) F_{\mathrm{DFT}}(k_x - k'_x, k_y - k'_y, k_t) \\
& -\left(\frac{i}{2\pi}\right)\left[T_t S_{\mathrm{DFT}}(k_x, k_y, k_t)\right] ,
\end{aligned}
\tag{3.11}
$$

where $F_{\mathrm{DFT}}(k_x, k_y, k_t)$ represents the 3D Discrete Fourier Transform (DFT) coefficients of the observed radar data field sequence $F(i, j, k)$, $U_{\mathrm{DFT}}(k'_x, k'_y)$ represents the 2D DFT coefficients of the field of estimated east-west motion vector components $U(i, j)$, $V_{\mathrm{DFT}}(k'_x, k'_y)$ represents the 2D DFT coefficients of the field of estimated north-south motion vector components $V(i, j)$, and $S_{\mathrm{DFT}}(k_x, k_y, k_t)$ represents the 3D DFT coefficients of the sequence of estimated evolution (i.e., growth and decay) fields $S(i, j, k)$, T_x and T_y are the lengths of the east-west and north-south dimensions of the observed gridded reflectivity fields, respectively, T_t is the number of reflectivity fields considered for motion estimation (i.e., the temporal span of the sequence of gridded reflectivity fields), N_x and N_y are the maximum harmonic numbers of $F_{\mathrm{DFT}}(k_x, k_y, k_t)$ in the horizontal and vertical dimension, respectively, and $N_x^+ = N_x/2$, $N_x^- = -N_x/2$, $N_y^+ = N_y/2$, and $N_y^- = -N_y/2$.

Eq (3.11) can be written in linear form as

$$\mathbf{y} = \mathbf{H}\mathbf{x}, \tag{3.12}$$

where

$$\mathbf{y}_{\mathrm{m}\times 1} \equiv \left[Y_0, Y_K^r, Y_K^i\right]^{\mathrm{T}}, \tag{3.13}$$

$$Y_K \equiv k_t F_{\mathrm{DFT}}(K), \tag{3.14}$$

$$Y_0 \equiv Y(0,0,0), \tag{3.15}$$

$$Y_K^r \equiv \mathrm{Re}\{Y_K\}, \tag{3.16}$$

$$Y_K^i \equiv \mathrm{Im}\{Y_K\}, \tag{3.17}$$

$$K \equiv k_x \in [1, N_x] \times k_y \in [1, N_y] \times k_t \in [1, N_t], \tag{3.18}$$

where × represents the Cartesian product and noting the conjugate symmetric harmonics have been excluded,

$$N = \{N_x, N_y, N_t\}, \tag{3.19}$$

is the integer set of selected maximum harmonic numbers of $F_{\mathrm{DFT}}(k_x, k_y, k_t)$,

$$m = (2N_x + 1)\,(2N_y + 1)(2N_t + 1) + 1, \tag{3.20}$$

$$\mathbf{x}_{\mathrm{n}\times 1} \equiv \left[U_0, V_0, S_0, U_{K'}^r, U_{K'}^i, V_{K'}^r, V_{K'}^i, S_{K''}^r, S_{K''}^i\right]^{\mathrm{T}}, \tag{3.21}$$

where

$$U_{K'} \equiv U_{\mathrm{DFT}}(K'), \tag{3.22}$$

$$V_{K'} \equiv V_{\mathrm{DFT}}(K'), \tag{3.23}$$

$$S_{K''} \equiv S_{\mathrm{DFT}}(K''), \tag{3.24}$$

$$U_0 = U(0,0), \tag{3.25}$$

$$V_0 = V(0,0), \tag{3.26}$$

$$S_0 = S(0,0,0), \tag{3.27}$$

$$U_{K'}^r \equiv \mathrm{Re}\{U_{\mathrm{DFT}}(K')\}, \tag{3.28}$$

$$U_{K'}^i \equiv \mathrm{Im}\{U_{\mathrm{DFT}}(K')\}, \tag{3.29}$$

$$V^{r}_{K'} \equiv \mathrm{Re}\left\{V_{\mathrm{DFT}}\left(K'\right)\right\}, \tag{3.30}$$

$$V^{i}_{K'} \equiv \mathrm{Im}\left\{V_{\mathrm{DFT}}\left(K'\right)\right\}, \tag{3.31}$$

$$S^{r}_{K''} \equiv \mathrm{Re}\left\{S_{\mathrm{DFT}}\left(K''\right)\right\}, \tag{3.32}$$

$$S^{i}_{K''} \equiv \mathrm{Im}\left\{S_{\mathrm{DFT}}\left(K''\right)\right\}, \tag{3.33}$$

$$K' \equiv k'_x \in \left[1, M_x\right] \times k'_y \in \left[1, M_y\right], \tag{3.34}$$

$$K'' \equiv k''_x \in \left[1, L_x\right] \times k''_y \in \left[1, L_y\right] \times k''_t \in \left[1, L_t\right], \tag{3.35}$$

$$M = \left\{M_x, M_y\right\} \text{ and} \tag{3.36}$$

$$L = \left\{L_x, L_y, L_t\right\} \tag{3.37}$$

are the integer sets of selected maximum harmonic number for the DFTs of the estimated motion vector fields, $U_{\mathrm{DFT}}(k_x, k_y)$ and $V_{\mathrm{DFT}}(k_x, k_y)$, and the evolution term, $S_{\mathrm{DFT}}(k_x, k_y, k_t)$, respectively, and

$$n = 2(2M_x + 1)(2M_y + 1) + (2L_x + 1)(2L_y + 1)(2L_t + 1). \tag{3.38}$$

The matrix, **H,** is constructed according to Eq (3.11) such that Eq (3.12) is satisfied. The DFT coefficients of the components of the motion vector field can then be estimated efficiently using linear least squares estimation by

$$\mathbf{x} = \left(\mathbf{H}^{\mathrm{T}}\mathbf{H}\right)^{-1}\mathbf{H}^{\mathrm{T}}\mathbf{y} = \mathbf{H}^{+}\mathbf{y}, \tag{3.39}$$

where $^{+}$ represents the matrix pseudoinverse operation. For implementation in the CASA system, $N = \{30, 30, 4\}$, $M = \{1, 1\}$, $L = \{0, 0, 0\}$ were the selected parameters sets determined from empirical studies.

The nature of the continuity equation [Eq (3.10)] upon which the nowcasting model is based imposes continuity of motion vectors over the entire grid, even where no

reflectivity is observed (missing data points and reflectivity values below a pre-determined threshold are set to a value of zero). This is important because while observations may not exist in a particular region at time t_0, observations (and subsequent predictions) may be advected into these regions at times up to $t_0+\tau$, where τ is the maximum lead time for prediction.

3.5 The sinc kernel-based advection method

An advection technique based on a sinc kernel expansion has been developed for use within the CASA nowcasting system. In this scheme, the reflectivity field $F(x, y, t)$ is approximated according to the Whittaker-Shannon-Kotelnikov sampling theorem (Whittaker 1915; Shannon 1949; Higgins 1996) as

$$F(x, y, t) = \sum_{k=1}^{N_x} \sum_{l=1}^{N_y} F_{kl}(t)\,\mathrm{sinc}(x/\Delta x - k)\,\mathrm{sinc}(y/\Delta y - l)\,, \tag{3.40}$$

where the equidistant samples of $F(x, y, t)$, $F_{kl}(t) = F(k\Delta x, l\Delta y, t)$, may be interpreted as the coefficients of the 2D product basis that are obtained by appropriate translation and rescaling of the sinc kernel function, $\mathrm{sinc}(x) = \sin(\pi x)/(\pi x)$. The discrete approximation of Eq (3.16) can be written as

$$\frac{\partial}{\partial t} F_{kl}(t) = -\frac{U_{kl}}{\Delta x} \cdot \left[\mathbf{A}\mathbf{F}(t)\right]_{kl} - \frac{V_{kl}}{\Delta_y} \cdot \left[\mathbf{F}(t)\mathbf{Z}\right]_{kl} \text{ and} \tag{3.41}$$

$$F_{kl}(t+\delta_t) = F_{kl}(t) - \left\{ \frac{U_{kl}}{\Delta x}\left[\mathbf{A}\mathbf{F}(t)\right]_{kl} + \frac{V_{kl}}{\Delta y}\left[\mathbf{F}(t)\mathbf{Z}\right]_{kl} \right\} \delta_t, \tag{3.42}$$

where

$$\mathbf{A} \equiv \left[A_{km}\right] = \left[\mathrm{Dsinc}(k-m)\right], \tag{3.43}$$

$$\mathbf{Z} \equiv \left[Z_{nl}\right] = \left[\mathrm{Dsinc}(n-l)\right], \tag{3.44}$$

$$\mathbf{F}(t) \equiv \left[F_{ml}(t)\right] \text{ or } \mathbf{F}(t) \equiv \left[F_{kn}(t)\right], \tag{3.45}$$

$$\mathrm{Dsinc}(x) \equiv \frac{d}{dx}\mathrm{sinc}(x) = \begin{cases} \dfrac{1}{x}\left[\cos(\pi x) - \mathrm{sinc}(x)\right] & x \neq 0 \\ 0 & x = 0. \end{cases} \tag{3.46}$$

Eqs (3.41)–(3.46) show that numerical advection is conducted by a matrix computation where the temporal integration is done by recursion of matrix computations relative to the temporal resolution of the data determined by the choice of δ_t in Eq (3.42).

The implementation of the DARTS and sinc kernel-based nowcasting methodology is described in the next section.

CHAPTER IV. REAL-TIME IMPLEMENTATION IN CASA DCAS

4.1 Introduction

The National Science Foundation (NSF) Engineering Research Center (ERC) for the Collaborative Adaptive Sensing of the Atmosphere (CASA) is a consortium of four universities [Colorado State University, University of Massachusetts (lead university), University of Oklahoma, and University of Puerto Rico at Mayaguez] and a partnership with industry and government laboratories. CASA aims to lay the fundamental and technological foundations for dense, adaptive radar networks; conduct proof-of-concept demonstrations using field-scale test beds deployed in hazard-prone areas; and ultimately transition the concepts and technologies into practice through commercialization and technology transfer mechanisms (McLaughlin et al. 2009). The common objective of CASA is to change the weather sensing paradigm through Distributed Collaborative Adaptive Sensing (DCAS; McLaughlin et al. 2005), improving the coverage of the lowest portion of the atmosphere through coordinated scanning of low-power, short-range networked radars. Junyent and Chandrasekar (2009) developed a framework to study the coverage characteristics of such radar networks.

DCAS represents a new paradigm in remote sensing based on low-cost, dense networks of radars that operate at short ranges, communicate with one another, and adjust their sensing strategies in direct response to the evolving weather and to changing user needs (McLaughlin et al. 2005; Kurose et al. 2006; Philips et al. 2007). The overarching

DCAS concept is illustrated in Figure 4. Current operational meteorological radar networks, such as the Next Generation Radar Network (NEXRAD) in the U.S., sample the atmosphere with "sit-and-spin" volume coverage patterns where such a pattern is predetermined. DCAS is an end-user driven approach that targets sensitivity when and where the needs of its end-users are greatest. The advantages gained by adaptively allocating sensitivity of short-range weather radars with overlapping coverage include higher quality measurements due to the ability to dwell longer in volumes where echoes are weak, faster sampling of volumes with rapidly evolving dynamics, mitigating spatial resolution degradation due to broadening of the radar beam at farther ranges, and multi-Doppler looks for high accuracy wind field retrieval. Additionally, effects of the earth's curvature and terrain-induced blockage that diminish coverage at low altitudes and thus prevent the observation of low-altitude phenomena such as tornadoes and limit the accuracy of precipitation estimates near the ground are reduced (National Research Council 2002; Junyent et al. 2010). These features enable the network to comprehensively map damaging winds and heavy rainfall from the tops of storms down to the boundary layer and maximize the radar system's capability to best fulfill each particular user's expectations (McLaughlin et al 2009).

The first DCAS demonstration test bed, the CASA Integrated Project 1 (IP1), was deployed in southwestern Oklahoma in a region frequented by tornadoes and severe thunderstorms during the winter and spring of 2006.

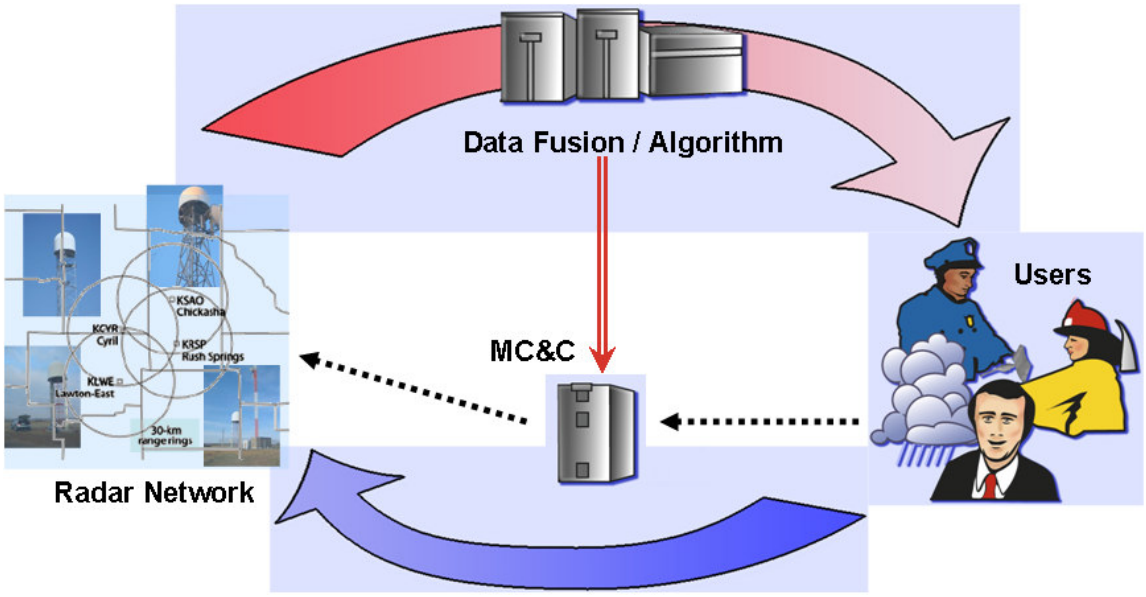

Figure 4. Illustration of the CASA DCAS concept.

The IP1 radar nodes (Figure 5) are installed along U.S. Interstate 44, southwest of Oklahoma City, Oklahoma, located at Chickasha (KSAO; 35.0314^{o} lat, -97.9561^{o} lon, 355 m alt), Rush Springs (KRSP; 34.8128^{o}, -97.9306^{o}, 436 m), Cyril (KCYR; 34.8740^{o}, -98.2512^{o}, 445 m), and Lawton (KLWE; 34.6239^{o}, -98.2708^{o}, 396 m), Oklahoma. They are separated by approximately 30 km and cover approximately 7000 km^{2} (Figure 6).

The IP1 network consists of a computer cluster called the System Operation and Control Center (SOCC; SOCC 2010) that runs a suite of network control algorithms known as Meteorological Command and Control (MCC) providing a closed-loop software control system to coordinate interaction between the radar nodes. The SOCC, which contains the scan rules and algorithms responsible for automated network operation, is located in the National Weather Center building in Norman, Oklahoma. The SOCC (or multiple SOCCs) can be physically located wherever there is an adequate network connection to provide connectivity between the radar node sites and the SOCC.

Figure 5. The four polarimetric radars forming the CASA radar network.

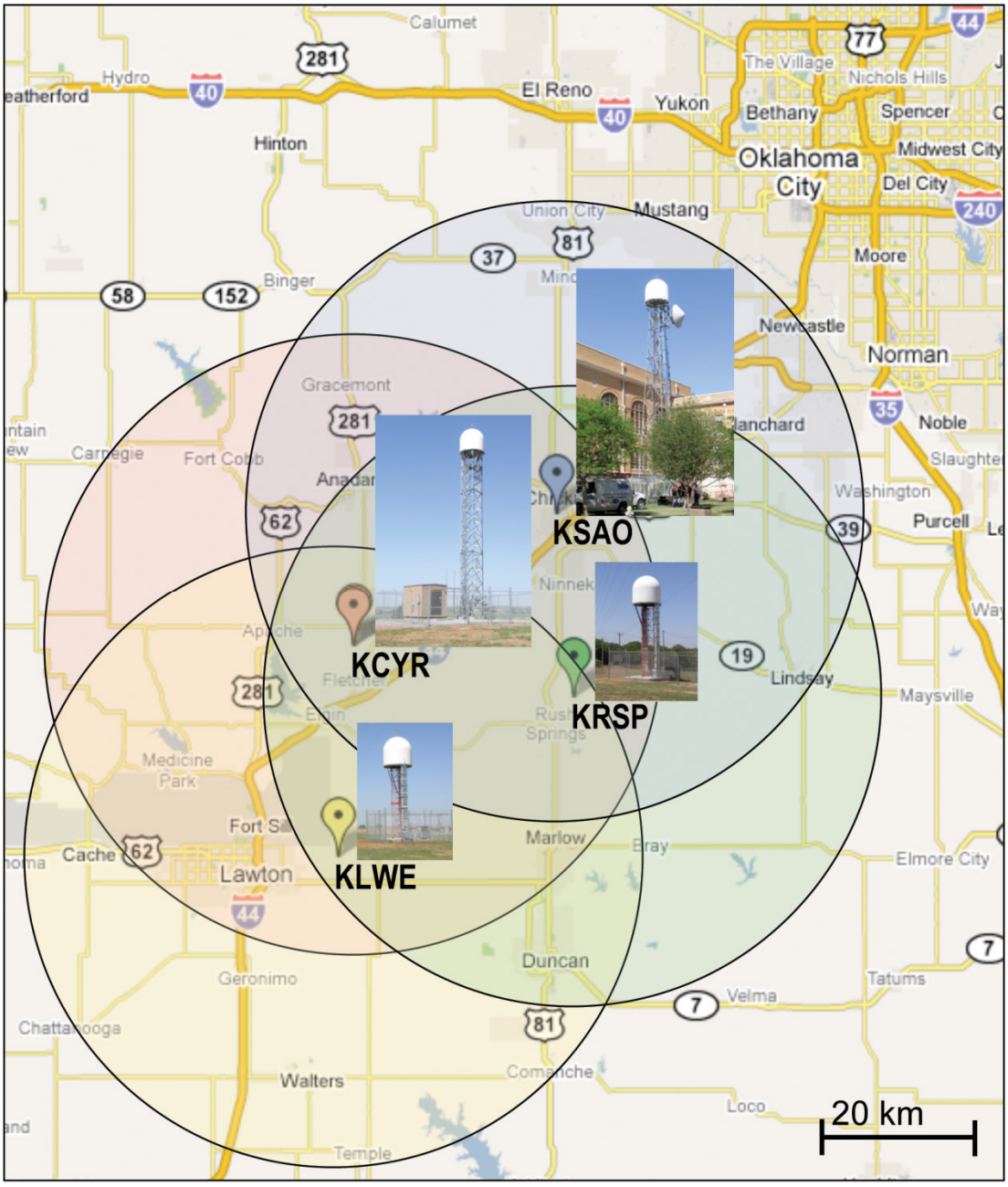

Figure 6. The CASA radar network coverage area map. Coverage circles are 40 km in radius [from Junyent et al. (2010)].

The MCC continuously ingests and stores data files received from the radar nodes, detects the relevant weather features in the individual and overlapping radar data, and creates a list of tasks associated with the detected features (Zink et al. 2005). The detected features and their associated tasks are then used to generate optimized scan strategies that are fed back to the radar nodes with a 1-min period (i.e., the system heartbeat). During each heartbeat, each radar performs a 360^{o} PPI surveillance sweep at an elevation angle of 2^{o} (20 s) followed by a multiple-elevation PPI sector scan targeted on one or more important meteorological phenomenon (40 s). The orientation and width of the sector in azimuth is determined by the MCC to cover the meteorological features of interest to the users, whereas the number of elevations scanned within the sector varies with the width of the sector. For example, a 60° sector includes seven elevations, whereas a 180° sector includes only four elevations. The elevation angles used are 1°, 3°, 5°, 7°, 9°, 11°, and 14° for coverage from less than 600 m to more than 10 km above ground level (McLaughlin et al. 2009). Based on client-server architecture, the radar user (i.e., the MCC algorithms running at the SOCC or any other authorized entity connecting to it) can send high-level commands specifying radar parameters and actions. Further details of the IP1 radar network are given by McLaughlin et al (2009) and Junyent et al. (2010).

A nowcasting system was implemented in the CASA DCAS to produce predictions of radar reflectivity fields up to 10 min into the future to support emergency manager decision-making and in a novel manner to support researchers and operational forecasters where 1–5-min nowcasts are used to steer the radar nodes to better observe moving precipitation systems. The nowcasting system implemented in the CASA DCAS is described in the next sub-section.

4.2 Architecture of the operational nowcasting system

The nowcasting system development and maintenance are done by Colorado State University located at Fort Collins, Colorado. The MCC located at the SOCC at the University of Oklahoma at Lawton, Oklahoma, ingests data from the radars, identifies meteorological features in the data, and determines each radar's future scan strategy based on detected feature contours and end-user requirements. The data are converted to Network Common Data Format (NetCDF; Rew and Davis 1990a) and sent to the SOCC located at the University of Massachusetts at Amherst via a Local Data Manager (LDM; Rew et al., 1990b; Fulker et al. 2000). The overall system architecture illustrating this process is depicted in Figure 7. While the entire nowcasting process could have been performed at the SOCC located at Norman, Oklahoma, this process was established as a demonstration experiment to understand the challenges related to distributed processing as part of the CASA network scaling (Jogalekar and Woodside 2000) operation.

After the radar data files are suitably synchronized by the ingester, the individual radar data files are gridded and merged. These gridded and merged data files are input to the DARTS nowcasting module, which generates predicted reflectivity fields that are presented to the end-user via an Internet-based display. The diagram of the operational DARTS software module is shown in Figure 8 with an example observed reflectivity field and corresponding 10-min prediction as shown on the Internet-based display depicted in Figure 9.

Evaluation of the performance of the DARTS nowcasting system during the 2009 IP1 experiment is described in the next section.

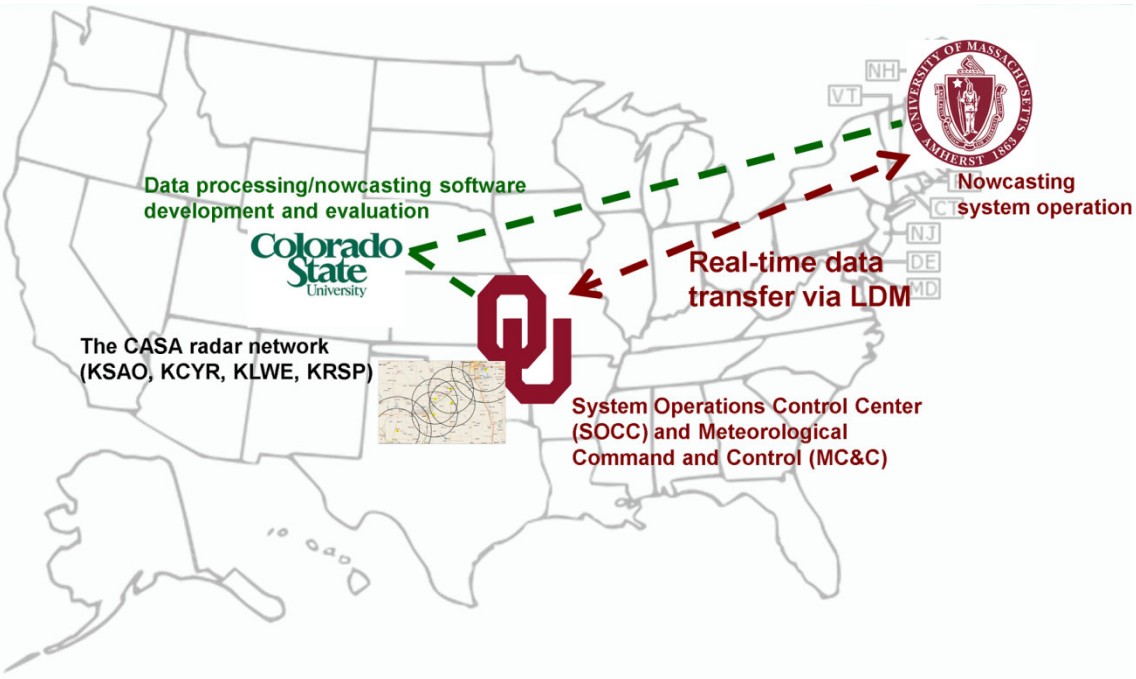

Figure 7. Operational CASA nowcasting system architecture.

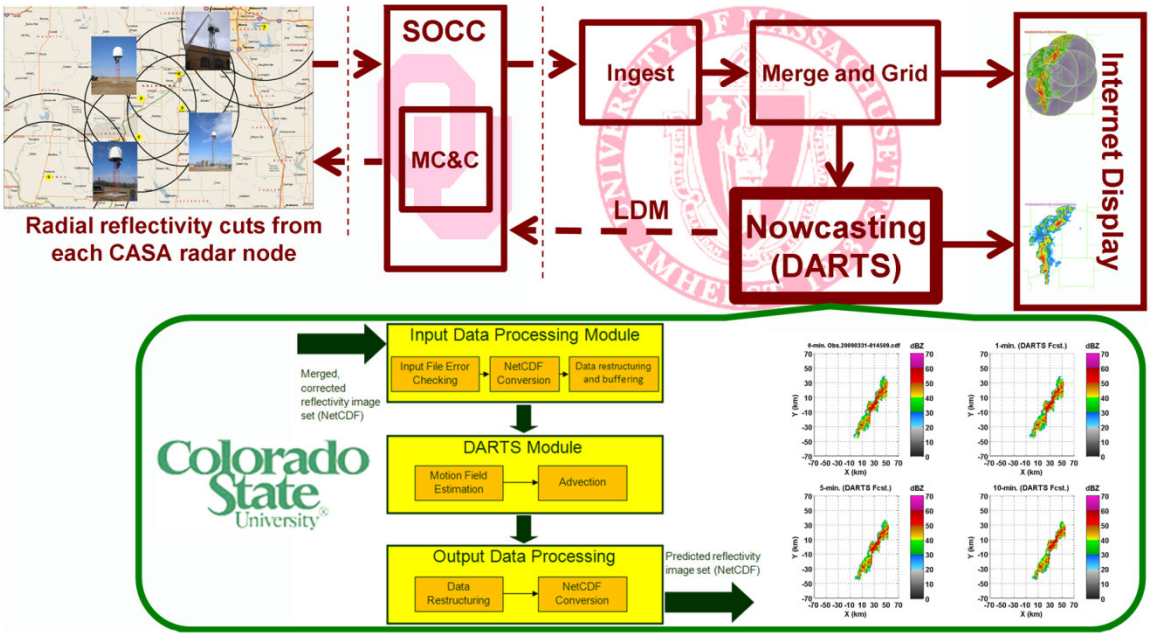

Figure 8. Operational CASA nowcasting software architecture.

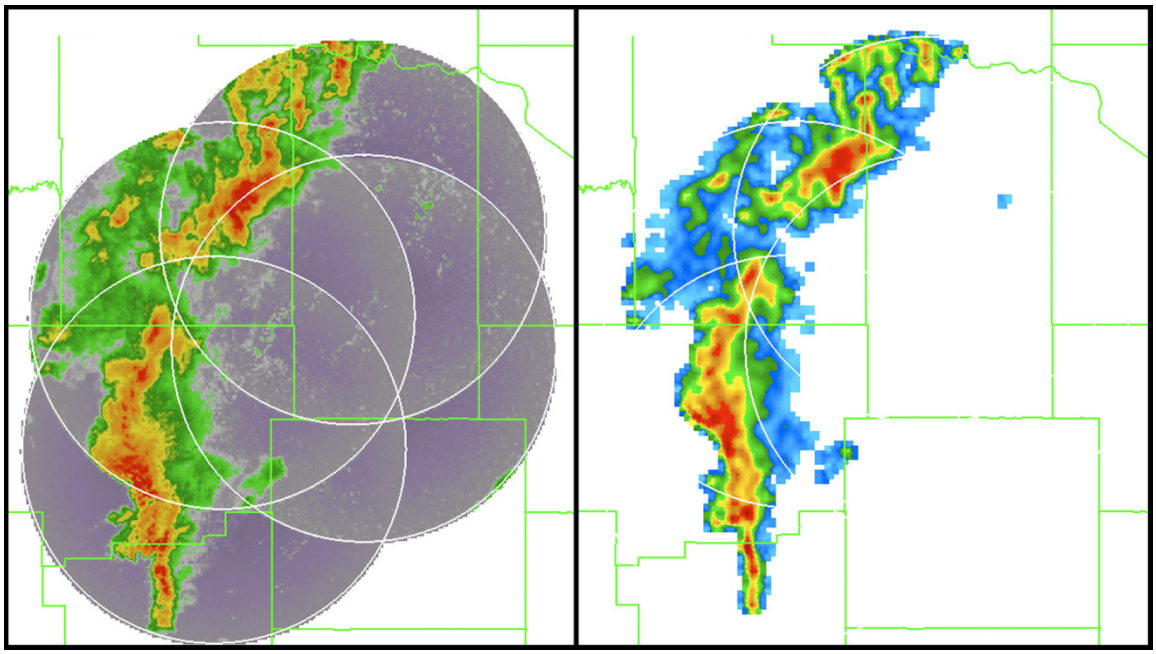

Figure 9. Example CASA operational Internet display of an observation from the 10 Feb event.

4.3 Assessment of nowcasting performance during the CASA 2009 IP1 experiment

4.3.1 Data

Radar reflectivity data collected during 17 events through the 2009 CASA IP1 experiment were considered for evaluation. The average duration of each event in the dataset was approximately 3.9 h for a total of approximately 66 h of data (approximately 3960 data frames). The set of events covered a wide range of precipitation pattern types, consisting of super-cellular, strong and steady quasi-linear, and disorganized multi-cellular events (Byers and Braham 1949; Weisman and Klemp 1986). Details of the events are given in Table 1.

Table 1. Summary of precipitation event data collected during the CASA IP1 experiment used for nowcasting evaluation.

Event No.	Start time	Approximate duration (h)	Type
1	2111 UTC 10 Feb	5.75	Supercell
2	0014 UTC 10 Mar	4.75	Line
3	2307 UTC 23 Mar	6.00	Multicell
4	0025 UTC 31 Mar	2.00	Line
5	2236 UTC 16 Apr	3.00	Multicell
6	2347 UTC 18 Apr	1.00	Single-cell
7	2337 UTC 26 Apr	5.00	Line
8	0721 UTC 29 Apr	8.00	Multicell
9	0251 UTC 30 Apr	6.00	Multicell
10	0858 UTC 02 May	6.75	Multicell
11	1422 UTC 05 May	3.00	Multicell
12	0334 UTC 09 May	1.50	Single-cell
13	0907 UTC 11 May	1.75	Multicell
14	0930 UTC 12 May	2.50	Multicell
15	0319 UTC 13 May	3.25	Supercell
16	0430 UTC 14 May	2.50	Supercell
17	0234 UTC 16 May	3.00	Line

Constant Altitude Plan Position Indicator (CAPPI) grids at an altitude of 1 km above ground level (AGL) with grid spacing of 0.5 km covering an area of dimension ±70 km in the east-west and north-south directions were generated by merging attenuation-corrected reflectivity data from each of the four network radar nodes during each 1-min volume scan. The reflectivity resolution is 1 dBZ and a threshold of 20 dBZ was applied. Figure 10 shows examples of the reflectivity and DARTS motion vector fields for four of the 17 events (one for each of the storm types identified: line, multicell, single cell, and supercell) illustrating the differences in structure between the weather event types and the corresponding estimated motion vector fields.

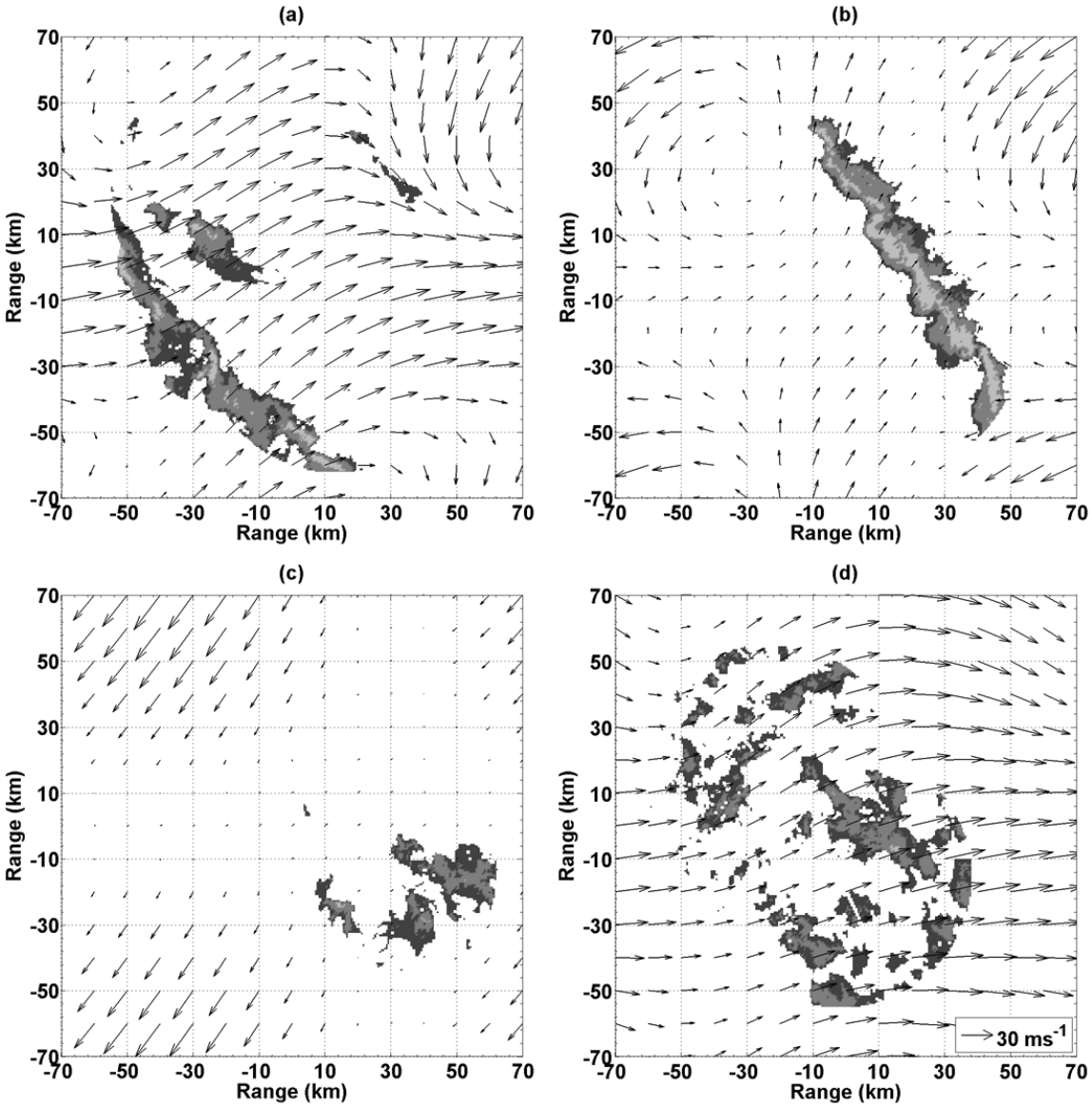

Figure 10. Example observed reflectivity field and corresponding DARTS-estimated motion vector field depicting spatial variability between events for (a) 2225 UTC 10 Feb (supercell), (b) 0103 UTC 31 Mar (line), (c) 2352 UTC 18 Apr (single-cell), and (d) 0918 UTC 11 May (multicell) events. Levels of gray shading correspond to reflectivity values 20-35 dB*Z*, 35-50 dB*Z*, and larger than 50 dB*Z*, respectively.

4.3.2 Quantitative performance assessment

Nowcasting applications involving warning decision support for detection of potentially severe weather typically measure nowcasting performance in terms of categorical yes/no (e.g., rain/no-rain) detection relative to a predetermined measurement threshold representative of a desired threat (Doswell et al. 1990; Ebert and McBride 2000; Schaefer 1990; Stensrud and Wandishin 2000). Three widely used attributes to assess categorical nowcasting performance are the Threat Score or Critical Success Index (CSI), False Alarm Ratio (FAR), and Probability of Detection (POD), each defined as (Donaldson et al. 1975; Wilks 2006)

$$\mathrm{CSI} = \frac{A}{A+B+C}, \tag{4.1}$$

$$\mathrm{FAR} = \frac{B}{A+B}, \text{ and} \tag{4.2}$$

$$\mathrm{POD} = \frac{A}{A+C}, \tag{4.3}$$

where A represents the intersection of the areas over which the event was forecast and subsequently occurred (i.e., a "hit"), B represents the area over which the event was forecasted and subsequently did not occur (i.e., a "false alarm"), and C is the area over which the event occurred but was not forecast to occur (i.e., a "miss"). Values of the CSI, POD, and FAR range from 0 to 1, with a value of 1 representing perfect CSI and POD scores and a value of 0 representing a perfect FAR score.

Nowcasting for hydrological applications is typically assessed using continuous scalar measures of forecast accuracy such as Mean Absolute Error (MAE; Vivoni et al. 2007). The MAE is defined as (Wilks 2006)

$$\mathrm{MAE} = \frac{1}{N}\sum_{i=1}^{N}\left|F_i - O_i\right|, \tag{4.4}$$

where (F_i, O_i) is the ith pair of N forecasts and observations. Both categorical (CSI, FAR, and POD) and continuous (MAE) scores were used to assess performance of the CASA nowcasting system during the 2009 IP1 experiment.

A study was performed to determine the optimal parameter settings for the DARTS model [Eq (3.11)] using CASA reflectivity data. DARTS was run with several lengths of the reflectivity data sequence used for assimilation [i.e., the temporal span of $F(x, y, t)$ in Eq (3.10) hereby referred to as the "history length"] and combinations of parameters N_x, N_y, and N_t using data from the 10 Feb (supercell), 31 Mar (line), and 11 May (multicell) events. The results depicted in Figure 11 and Figure 12 show DARTS to be relatively insensitive to the history length and N_x, N_y, and N_t parameters, with nearly identical performance when considering history lengths between 10 and 25 data frames and slightly better performance when considering $N_x = N_y = 30$ and $N_t = 4$. These settings and an assimilation window of 10 min (10 data frames) were adopted for operational use.

Another study was performed to investigate the effect of scoring area (box) size and reflectivity threshold on CSI, FAR, and POD scores. Scoring box sizes of 1 km × 1 km to 4 km × 4 km and thresholds of 20–45 dBZ were considered. The results depicted in Figure 13 and Figure 14 show a large difference in scores over different choices of box size and reflectivity thresholds. It was decided to use the smallest box size (1 km × 1 km) for assessment of nowcasting performance in the CASA network to coincide with the resolution of the data.

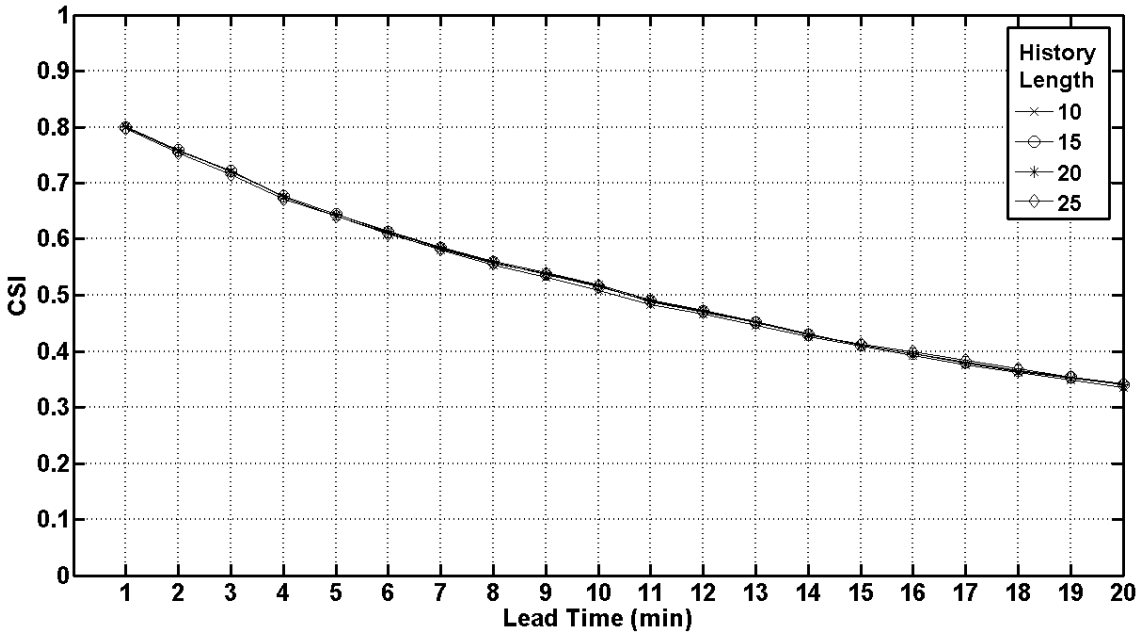

Figure 11. Effect of variation of the assimilation window length (history length) on nowcasting performance using the DARTS model.

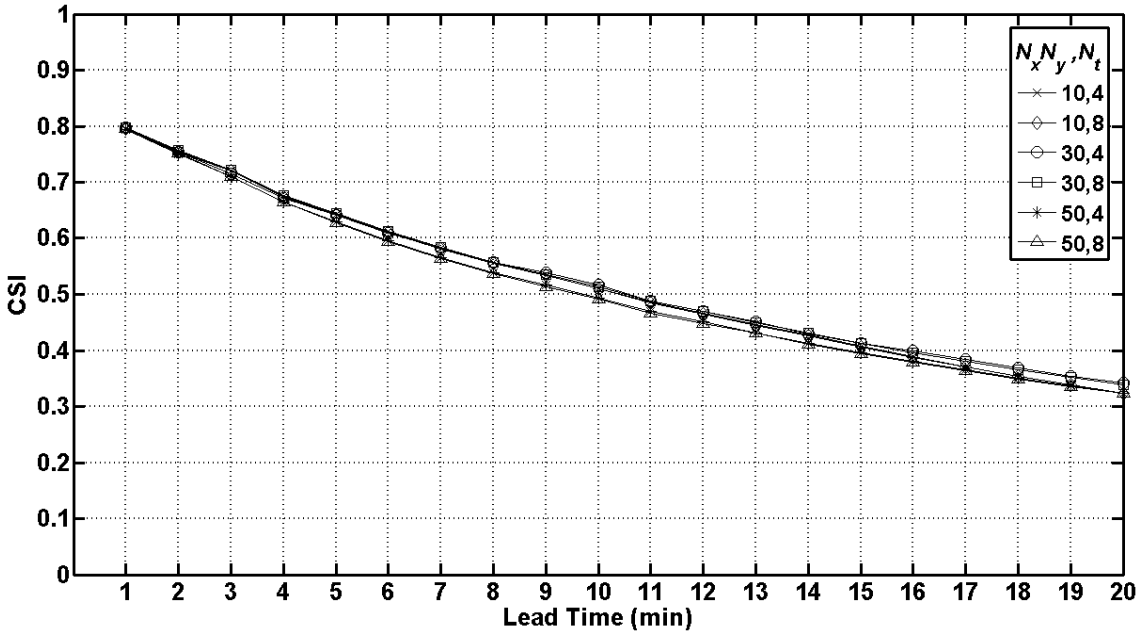

Figure 12. Effect of variations of spectral parameter values on nowcasting performance using the DARTS model.

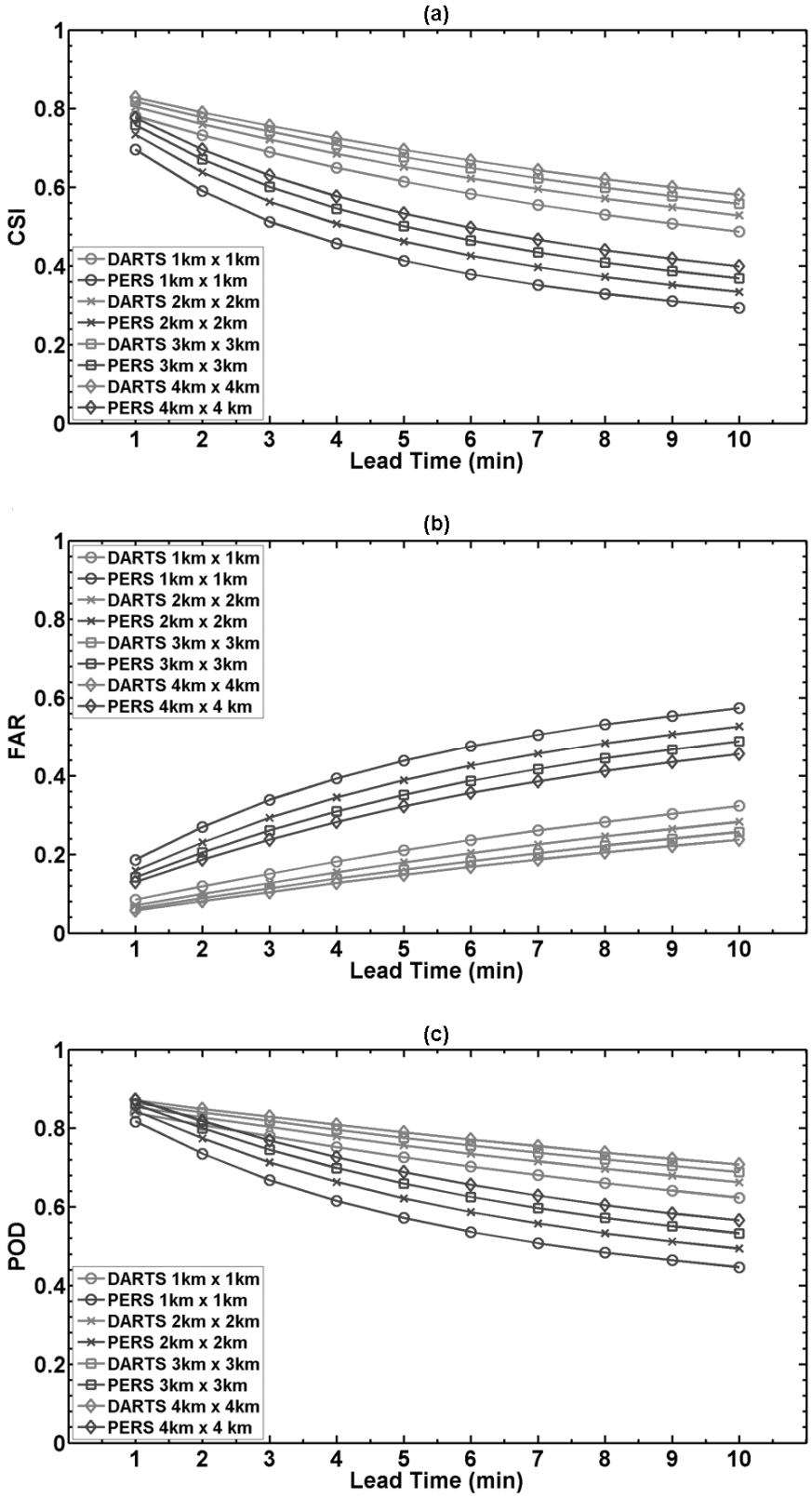

Figure 13. Effect of variation scoring box size values on nowcasting scores (a) CSI, (b) FAR, and (c) POD for DARTS and persistence (PERS) nowcasts.

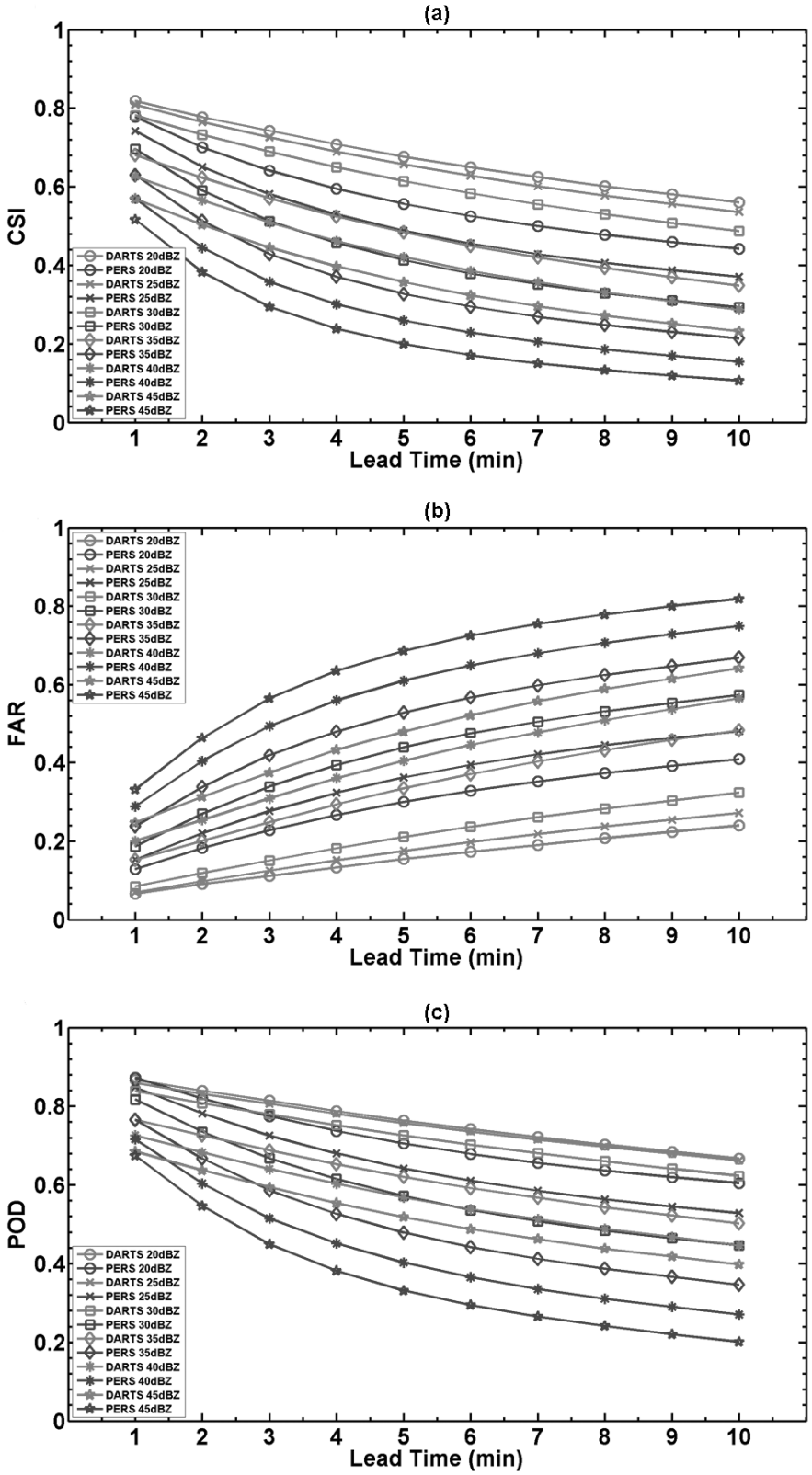

Figure 14. Effect of variation of scoring threshold values on nowcasting scores (a) CSI, (b) FAR, and (c) POD for DARTS and persistence (PERS) nowcasts.

A threshold of 30 dBZ was chosen as this level typically demarcates convective from stratiform rain (Hilgendorf and Johnson 1998).

The effect of including the S-term in Eq (3.11) was investigated. Figure 15 depicts an example prediction from the 31 Mar event comparing a 20–min prediction including the S-term to a corresponding prediction excluding the S-term. Figure 16 compares the CSI scores for the prediction model with and without inclusion of the S-term using data from the 10 Feb, 31 Mar, and 11 May events. The results are consistent with previous studies that showed no improvement in performance by including the S-term in the nowcasting model (Section 3.3).

The CSI, FAR, POD, and MAE score statistics for lead times up to 10 min averaged over all events are shown in Figure 17. The scores corresponding to nowcasting using the DARTS and sinc kernel-based advection methodology are favorable, with mean CSI scores above 0.5 and for the entire forecast period and improvement of approximately 1 standard deviation at a lead time of 10 min vs nowcasting using persistence. As expected, mean values decrease and standard deviation values increase with increasing lead time for both methods.

High computational efficiency of the DARTS algorithm is critical when running in the CASA radar network with scan update rates of 1 min. Average motion field generation and advection times were approximately 0.30 s and 47 s, respectively, when running the nowcasting system on a standard Linux-based compute server.

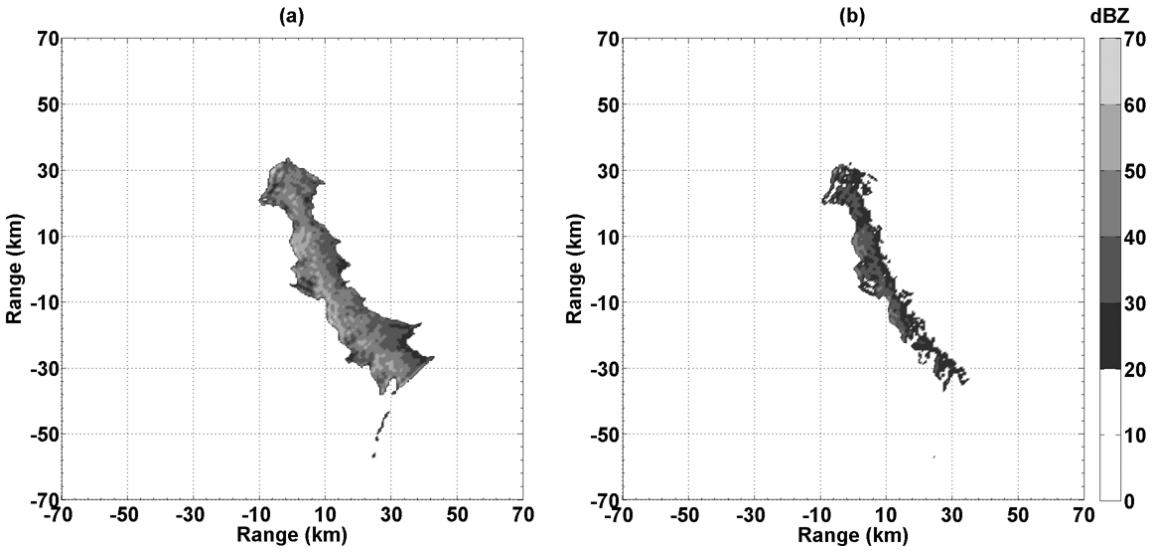

Figure 15. Example 20-min prediction corresponding to the 012311 UTC 31 Mar 2009 observation (a) without including the S-term and (b) including the S-term in the prediction model.

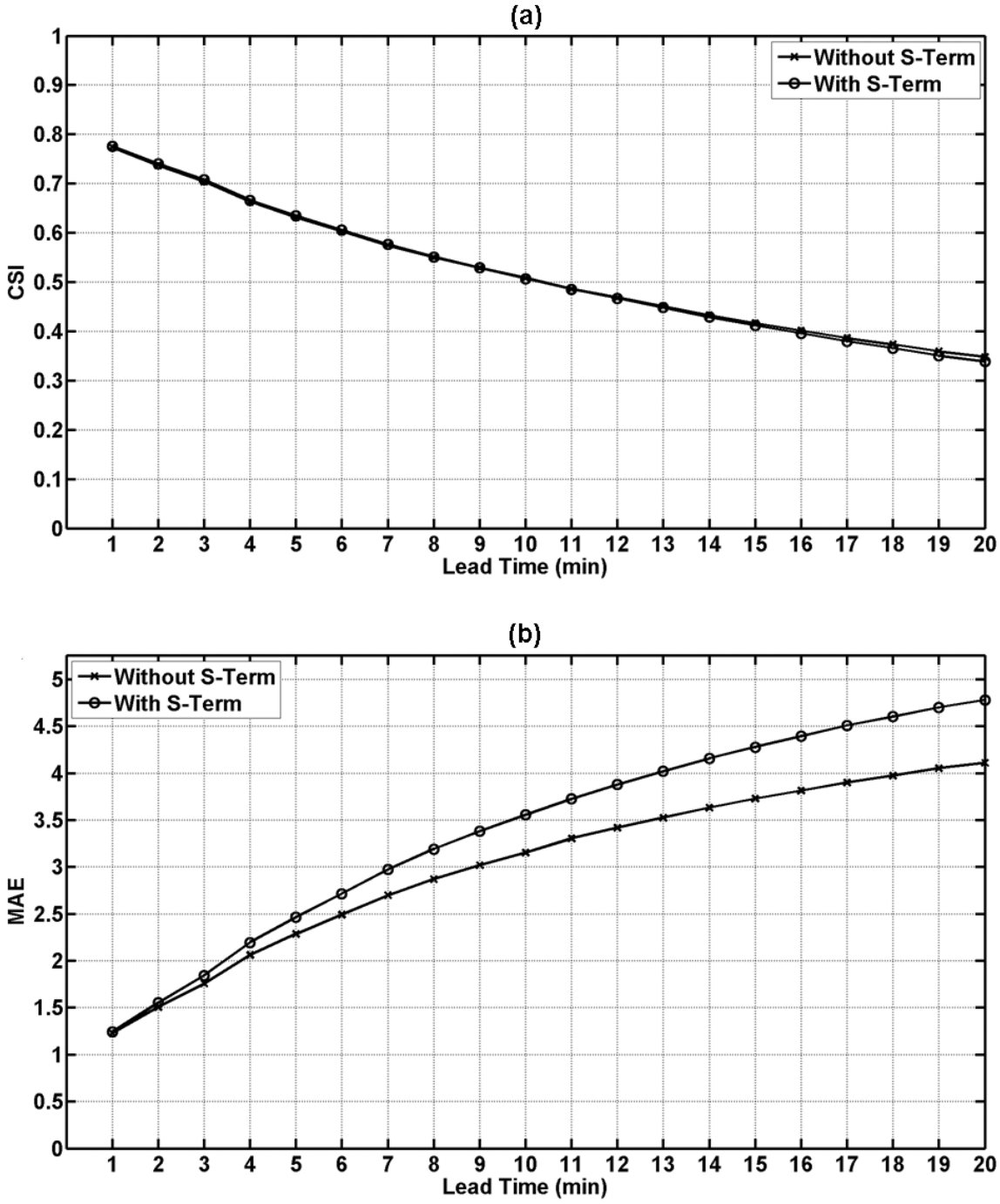

Figure 16. Comparison of (a) CSI and (b) MAE scores including and excluding the S-term in the prediction model.

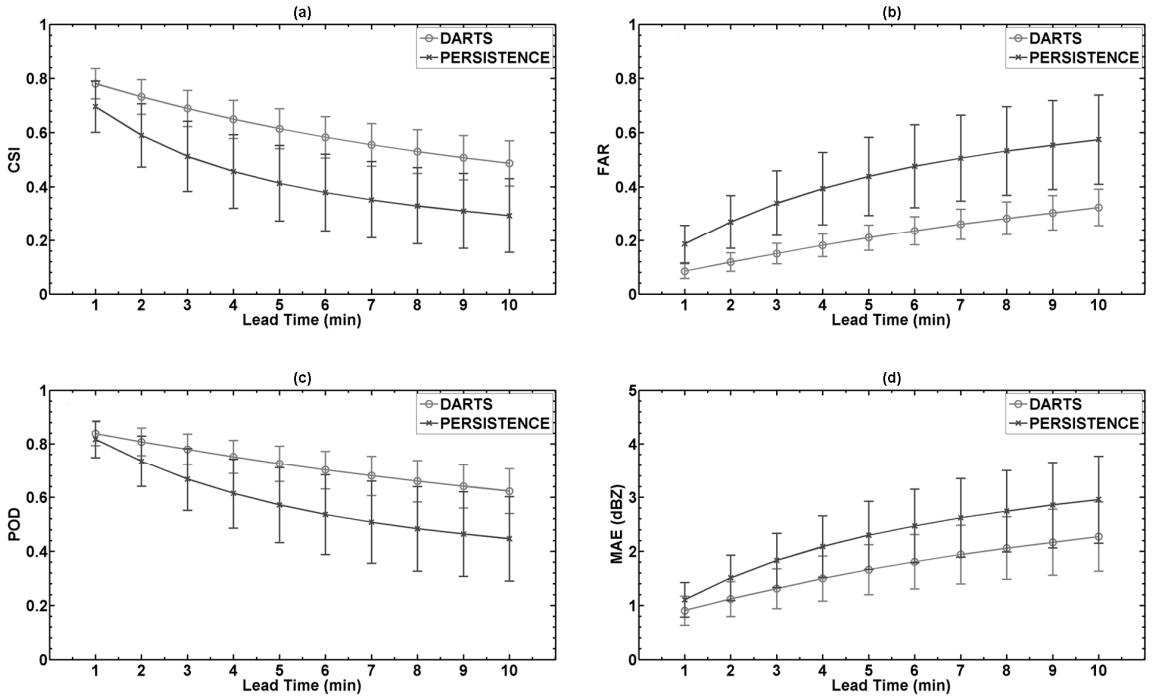

Figure 17. (a) CSI, (b) FAR, (c) POD, and (d) MAE score statistics comparing the performance of the DARTS and sinc-kernel-based advection nowcasting method vs persistence forecasts during the 2009 CASA IP1 experiment. The markers depict the mean scores over all 17 events in the dataset and each associated whisker represents one standard deviation above and below the mean value.

4.3.3 Improved radar observations via adaptive scanning

Until the 2009 IP1 experiment, the CASA system was optimized to scan based on observations from past scans. This latency was found to be detrimental in fast-moving weather systems and was significant enough that the automated scans occasionally cut off the leading edges of moving storms. To mitigate this condition, nowcasting was introduced into the DCAS closed-loop to generate fields of predicted reflectivity to provide better estimates of storm location for scanning purposes. In this sense, the motion vector field estimates generated by DARTS can be used to schedule future scanning strategies based on predicted motion (and thus future location) of storms. This information can be used to generate specific warning areas and allow for precise

deployment of spotters and first responders during severe weather events. Such capability also allows for faster sampling of important weather features as the radars are not scanning relatively unimportant regions throughout the entire 360^{o} sweep.

The ability of nowcasting to adjust the CASA radar scan strategy to observe the leading edge of a moving storm is illustrated in Figure 18, which depicts an image of the MCC display of the 0246 UTC 17 May observation comparing coverage afforded by radar node steering using previous observations vs steering using 5-min nowcasts. In this case, the storm was advecting towards the northeast. It is apparent the leading edge of the storm is observed when steering based on 5-min nowcasts and is missed when steering using previous observations.

The utility of the adaptive scanning capability was assessed by NWS forecasters, local emergency managers, and researchers during the 2009 IP1 experiment via end-user surveys (Phillips et al. 2008). End-user impact was considered to be the most valued performance appraisal in the CASA IP1 experiment and end-user feedback on radar scanning strategy adaptation was unanimously positive.

4.4 Summary and conclusions

Operational nowcasting capability was successfully incorporated into the CASA IP1 radar network. The DARTS and sinc kernel-based nowcasting methodology was implemented to mitigate the concern of computational efficiency given the 0.5 km/1 min data resolution and distributed nature of the system.

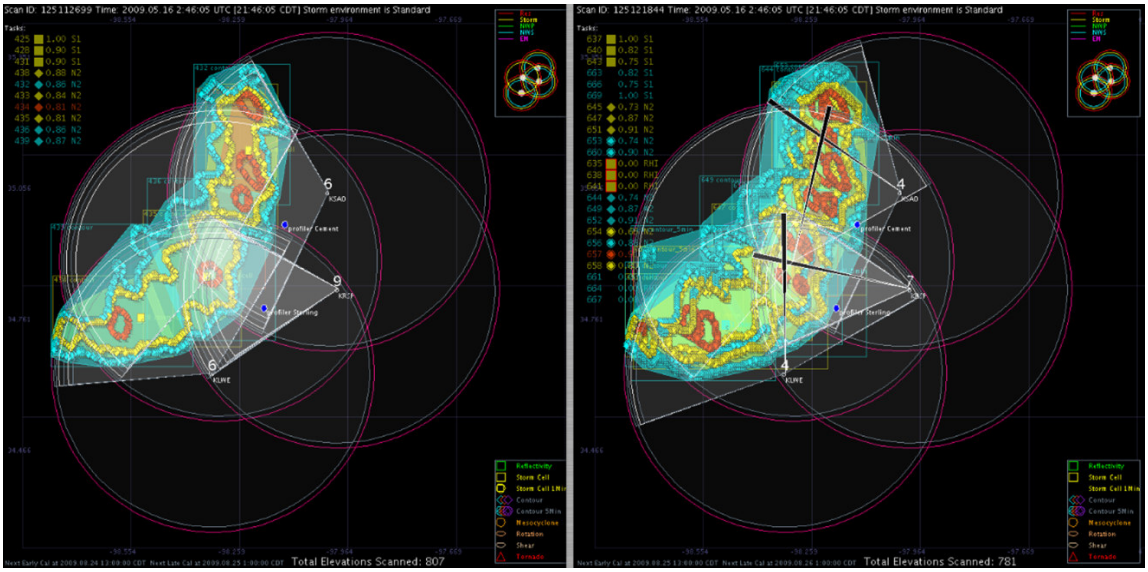

Figure 18. Example operational MCC display of the 0246 UTC 17 May observation comparing coverage afforded by radar node steering using previous observations (left) vs adaptive scanning using 5-min nowcasts (right). The observed reflectivity field is depicted with identified contours of interest shown by the blue, yellow, and red shaded areas. Radar coverage is depicted by the white shaded areas. The storm was advecting towards the northeast and it is apparent the leading edge of the storm is missed on the left and observed on the right.

Nowcasting out to 10 min provides emergency decision-making support to end-users of the CASA system. In this context, DARTS was evaluated quantitatively in a categorical (i.e., rain/no rain above a desired threshold) sense using CSI, FAR, and POD scores and in a continuous sense using MAE. The DARTS model was tuned for optimal performance in the CASA system and results were favorable regarding operational nowcasting during the 2009 IP1 experiment. The efficient and robust nowcasting methodology and implementation allowed for successful operation given the 1 min temporal resolution of the data and the distributed nature of the system architecture.

Nowcasting was also used at 1–5 min time scales to set up the radar network scanning strategy where steering the radar using nowcasting allowed the radar network to better

observe the atmosphere. Operational forecaster surveys were unanimously favorable regarding the use of nowcasting in this context.

CHAPTER V. SCALE-BASED FILTERING METHODS FOR OPTIMIZATION OF NOWCASTING PERFORMANCE

5.1 Introduction

Precipitation patterns include features over a range of scales where generally small-scale features have shorter lifetimes than larger-scale features [e.g., small, isolated thunderstorms typically have lifetimes of a few 10s of minutes, whereas continental-scale systems can have lifetimes of several hours or days (Orlanski 1975)]. Thus, each scale has a maximum lead time up to which variation at that scale can be predicted and attempting to predict scales past this maximum lead time can degrade nowcasting performance. Current nowcasting approaches account for scale-dependency by either building scale-dependency into the nowcasting model itself (Johnson et al. 1998; Lakshmanan et al. 2003; Seed 2003; Xu and Chandrasekar 2005) or by applying separate scale filters as either a pre-processing step to the input data (Wolfson et al. 1999) or as a post-processing step to predictions (Turner et al. 2004).

Selective scale-based filtering of radar data has been shown to improve nowcasting performance. Wilson (1966) determined that small-scale features in reflectivity or rainfall fields need not be forecast beyond their correspondingly short temporal scales. Browning (1979) used a large-scale filtering step in his FRONTIERS forecasting process, where data resolution was degraded from 5 km × 5 km to 20 km × 20 km and major storm cores were reintroduced after the patches had been advected. Bellon and Zawadzki (1994) showed that a consistent reduction in root mean square forecast errors could be obtained

by eliminating the small-scale perishable information by spatially averaging rainfall maps collected by a single radar (1 km/5 min resolution). Their results showed that optimum forecasts of hourly rainfall accumulations were achieved if the forecasted data field was smoothed by an 11 km × 11 km moving-average filter after a lead time of 23 min. A power-law related the length scale of the spatial filter to the forecast lead time and thus prevented structures from being reproduced beyond their lifetimes by increasing the smoothing window for increasing lead times. This power-law relationship was found to be nearly independent of the characteristics of the precipitation field. The S-PROG nowcasting model uses Fourier bandpass filtering to decompose observed reflectivity fields into a spatial scale-based cascade and a second-order autoregressive model to smooth forecast fields as various scales evolve through their life cycles (Seed 2003).

These studies considered filters with an isotropic region of support, but Wolfson et al. (1999) noted that boundary layer forcing for convection tends to organize storms in regions that are often several times longer than they are wide. To attempt to match this geometry, they used a filter with an elliptical region of support where the major axis of the ellipse was about four times longer than the minor axis to extract the large-scale signal from observed WSR-88D High-Resolution Vertically Integrated Liquid (HRVIL; Greene and Clark 1972; Boudevillain and Andrieu 2003; Smalley et al. 2003) fields (1 km/5 min/0.3 kg m^{-2} resolution). Smalley et al. (2003) stated VIL, which ranges from 0–80 kg m^{-2}, is preferred over composite reflectivity for air traffic control concerns as VIL is less susceptible to anomalous propagation breakthrough and provides depiction of an integrated 3D structure of the atmosphere that more accurately represents storm structure and intensity. The filtered HRVIL fields, which are related to reflectivity fields by a non-

linear function, are then used as input to a cross-correlation-based nowcasting method (Chornoboy et al. 1994) to compute an estimated motion vector field. Since the direction of the front was not known a priori, several filters with the ellipse at different orientations were used and the filter that yielded the maximum response at a particular location was assumed to be the one aligned with the front direction at that location. They stated while a large square filter would over-filter in the cross-front direction, the elliptical filter having a support area that is elongated along the front direction would allow extraction of these long narrow large-scale regions with a high degree of long-front filtering. They showed an approximate 20% improvement in CSI scores over a set of five storm events (approximately 26 h total) represented by HRVIL fields by applying this spatial elliptical filtering technique. Cartwright (1999) performed a comprehensive study to determine the optimal parameters of the elliptical filter kernel to maximize average CSI scores over a large dataset. Lakshmanan (2000) presented a fast algorithm to facilitate operational use. Van Horne et al. (2006) showed an approximate 3–14% improvement in CSI scores over three rainfall events (72 h) by pre-filtering NOWrad rainfall fields (4.8 km/15 min/1.27 mm resolution; Grassotti et al. 2003) using a square moving average filter before nowcasting using the cross correlation tracker used by Wolfson et al. (1999).

Turner et al. (2004) considered the localized pulse functions of the wavelet transform to better represent the often localized and intermittent characteristics of rainfall fields by providing many wavelet coefficients at each wavelet scale and position instead of a single Fourier coefficient for each Fourier scale (wavenumber). They used the wavelet transform to develop measures of predictability at each wavelet scale and used these measures to design an adaptive filter to remove scales deemed unpredictable from the

forecasts. They did so by weighting the wavelet scales representing the reconstructed predicted reflectivity fields according to the level of similarity in the wavelet cospectra between the observed and predicted fields at a given lead time. They showed the average correlation at a lead time of 4 h was increased from 0.50 for the original forecasts to 0.62 with this filtering method using four precipitation events (78 h total) depicted by NOWrad composite continental-scale reflectivity fields (4 km/15 min/5 dB*Z* resolution; Grassotti et al. 2003) using a variational nowcasting method (Laroche and Zawadzki 1994). Due to mathematical tractability, this adaptive filter was built to minimize mean squared error so they employed a rescaling technique to reverse the spreading effects from filtering to improve CSI scores that showed an approximate 12% improvement in CSI scores over a 20 h period of a single storm event. Germann et al. (2006) used this methodology to investigate the predictability of precipitation depicted by continental-scale reflectivity composites using a large dataset and affirmed that normally the scale weights at each scale become larger with increasing scale at a given lead time suggesting small scales are less predictable and decorrelate faster than larger-scale features.

This section presents a study to determine the optimal filtering strategy for nowcasting in the CASA DCAS system. This section provides an assessment of the elliptical, wavelet, and Fourier filtering methods for improving nowcasting performance using a common dataset of high spatial and temporal resolution reflectivity and the DARTS nowcasting method. Thus, the contribution of this work is to perform a direct comparison between the elliptical, wavelet filtering, and Fourier filtering methods for nowcasting performance improvement using the DARTS nowcasting model and high-resolution CASA radar reflectivity data. Consequently, understanding of the space-time

scale structure of precipitation patterns depicted by high-resolution radar reflectivity data can be inferred.

5.2 Filtering Methodology

The flowchart depicting the system-level implementation of each of the three filtering methods is shown in Figure 19. Further details of each of the three filtering strategies evaluated in this study are given in the following subsections. Since the purpose of the study was to determine the best operational filtering scheme for nowcasting in the CASA network, each filter was individually tuned for optimal performance based on results from empirical preliminary studies before comparison.

5.2.1 Fourier filtering

The DARTS algorithm provides a convenient means to perform ideal Fourier low-pass filtering on the observed input data. Fourier filtering is implemented by choosing the number of Fourier coefficients in the linear system representing Eq (3.11) to be less than the size of the input fields. In this manner, wavenumbers larger than N_x and N_y in each respective dimension are not considered in the motion vector field estimation process. Such filtering also truncates the size of the linear system (i.e., the linear system becomes overdetermined) facilitating faster computation necessary given the rapid scan rates of the CASA radars. In this context, scale is represented by Fourier wavenumbers, where high wavenumbers correspond to small scales and vice versa.

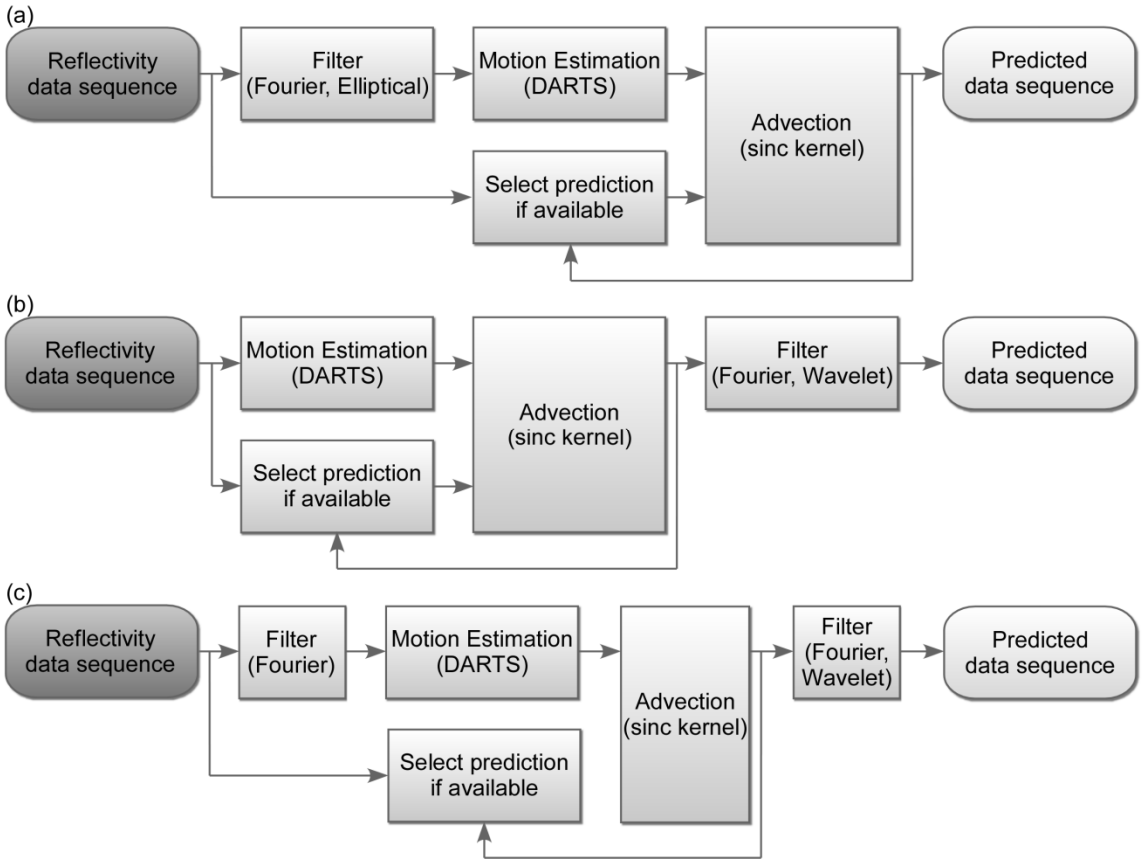

Figure 19. Illustration of the three filtering processes assessed for potential nowcasting performance improvement in CASA DCAS: (a) filtering before prediction (pre-filtering), (b) filtering after prediction (post-filtering), and (c) both pre- and post-filtering.

Results from a preliminary study using CASA reflectivity data determined truncating the Fourier space with a normalized cut-off frequency of about 0.2 in each direction yielded the best CSI scores (Figure 12). This parameter setting was considered in this research for filtering both observed and predicted data fields.

5.2.2 Spatial elliptical filtering

The elliptical filter used by Wolfson et al. (1999) was designed to match the geometry of observations where boundary layer forcing for convection tends to organize storms in regions that are often 3–4 times or more long than they are wide.

The motion of the small and large-scale storm components can be very different [for the example given in (Wolfson et al. 1999), the large-scale component was moving to the south-southeast at about 17.5 m s^{-1} while the small-scale component was moving to the east-northeast at about 10.8 m s^{-1}). Filtering the input data to remove small-scale components before motion estimation also allows for the estimation of storm motion due to cellular growth and decay within the storm envelope. Storm motion is driven by environmental wind at some steering level. This motion is well captured by radar echo tracking (cross-correlation in this case). They also propagate through development and dissipation. When propagation occurs through new development of convection at the front of the system while there is dissipation at the rear, it results in an apparent displacement. If this propagation is systematic and persistent, the resulting motion vector field will carry it as a skill in nowcasting. It must be persistent and systematic in order to be captured during the period over which the motion vectors are determined (Germann et al. 2006). The elliptical filter seeks to extract the envelope of the precipitation area by matching the shape of this area and better detect this motion driven by growth and dissipation. In this context, scale is represented by the area and dimensions of the filter kernel where a larger area removes more smaller-scale features organized by the major and minor axes specifications of the ellipse.

The elliptical filtering algorithm is described by the following steps:

1) The center point of the 2D elliptical filter is placed over a point, *p*, in the data field to be filtered. The average of all data points that lie in the region of support is computed.

2) The filter is rotated by 10^o (through 180^o) and the average value for each orientation is computed.

3) The value at p in the filtered data field is set to the maximum of the average values computed at each filter orientation.

4) Steps 1–3 are repeated for each location in the data field.

The elliptical filtering method is illustrated in Figure 20.

Results from a preliminary study considering CASA reflectivity data collected during the 10 Feb, 31 Mar, and 11 May events showed that a filter kernel with a major axis of 21 points (11 km) and a minor axis of 5 points (3 km), the same size filter kernel used by Wolfson et al. (1999), yielded the best nowcasting performance in terms of CSI scores (Figure 21). These parameters were used in this study and N_x and N_y were set equal to T_x and T_y in the DARTS model given by Eq (3.11) when applying this filtering procedure to the observed data sequence used for motion estimation.

5.2.3 Wavelet filtering

Because radar reflectivity regularly exhibit highly localized features with sharp spatial gradients, Turner et al. (2004) employed an adaptive filtering method based on the wavelet transform whose localized pulse functions are believed to better represent such localized intermittent fields. Instead of a single Fourier transform coefficient for each Fourier scale, many wavelet coefficients are obtained at each wavelet scale for each position. A wavelet filter was designed to selectively weaken or remove less predictable precipitation features from a forecast.

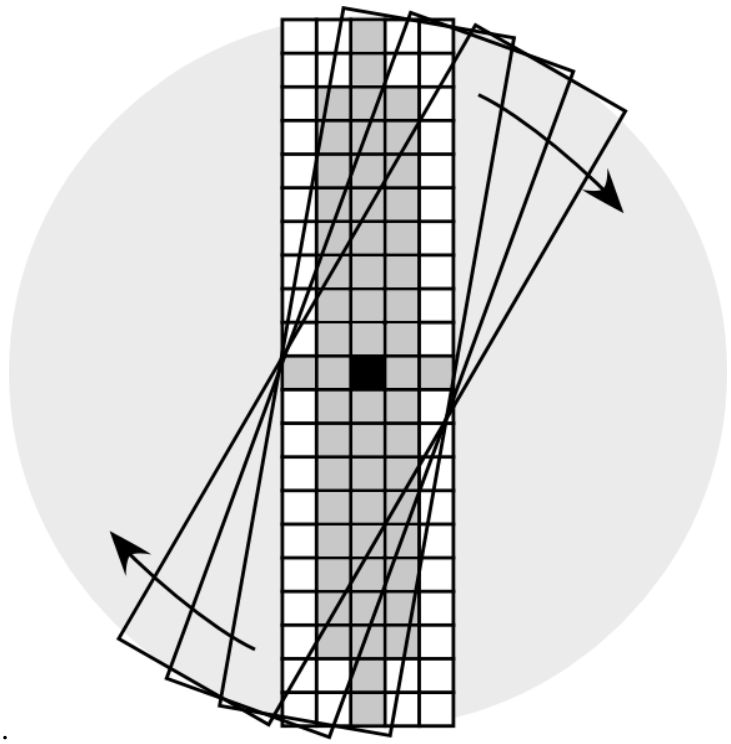

Figure 20. Illustration of elliptical filtering process using a 21 × 5 point filter kernel. The point, *p*, is represented by the black square and the region of support of the filter is represented by the gray squares.

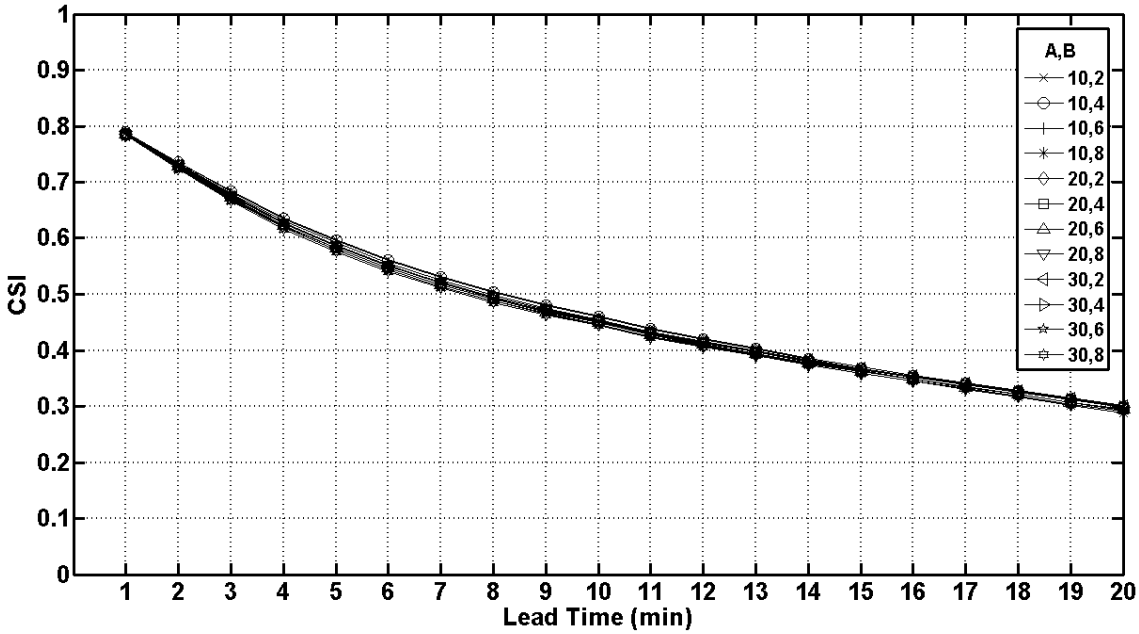

Figure 21. Effect of variation of elliptical filter parameter values on nowcasting performance using DARTS. The parameters A and B represent the major and minor axis diameters (in grid points) of the filter kernel, respectively.

In this context, the filtered forecast field, I_{ff}, is given by

$$w(m,T)W_f(m,x,y), \overline{f(x,y)} \xrightarrow{WT^{-1}} I_{ff}, \tag{5.1}$$

where $W_f(m, x, y)$ are the wavelet coefficients of the forecasted reflectivity field, $f(x,y)$, at each wavelet scale, m, and position, (x, y). Here, WT^{-1} represents the inverse wavelet transform and the overbar denotes the spatial (areal) average. The weight, $w(m, T)$, at each m and lead time, T, is given by

$$w(m,T) = \frac{Co_{fo}(m)}{S_f(m)}, \tag{5.2}$$

where,

$$S_f(m) = \overline{2^{-m}[W_f(m,x,y)]^2} \text{ and} \tag{5.3}$$

$$Co_{fo}(m) = \overline{2^{-m}W_o(m,x,y)W_f(m,x,y)}. \tag{5.4}$$

The wavelet coefficients of the observed field are given by $W_o(m, x, y)$. The spectrum of the forecasted field, $S_f(m)$, is thus a measure of the importance of each interval (or band) of scales in the forecasted field. The cospectrum, $Co_{fo}(m)$, indicates the level of similarity between the spectra of observed and predicted fields. In this study, $S_f(m)$ and $Co_{fo}(m)$ were based on the Haar wavelet as used by Turner et al. (2004) and a maximum scale index, m_{max}, beyond which wavelet coefficients were not calculated, was set equal to 3.

The rescaling procedure used by Seed (2003) to enhance CSI scores by counteracting the smoothing effects of the wavelet filtering procedure was implemented in this study. The forecast reflectivity field was renormalized to preserve the fraction of the field that exceeds a threshold (25 dB*Z* was considered in this study). The fraction of the observed reflectivity field that exceeded 25 dB*Z*, f_{25},

was calculated. The cumulative probability distribution for the forecast field was calculated and used to find the threshold in the forecast field, Z_f, which had probability to exceed 25 dBZ equal to f_{25}. Each data point in the original forecast field, $\Omega_{i,j}$, was then normalized to yield the rescaled forecast field, $\Omega'_{i,j}$, according to

$$\Omega'_{i,j} = \begin{cases} \Omega_{i,j} + (25 - Z_f) & \text{if } \Omega_{i,j} > Z_f \\ 0 & \text{otherwise.} \end{cases} \tag{5.5}$$

5.3 Assessment methodology

5.3.1 The radially averaged power spectral density

The radially averaged power spectrum (RAPSD) is a useful tool for objectively illustrating relative differences in spatial scale structure in 2D radar data fields. The RAPSD converts the coordinates of the power spectrum of 2D data from Cartesian to polar and removes the angular dependence through averaging to yield a 1D representation of the spectrum. The method was first made popular in the field of digital image processing, namely, used to quantify anisotropies in binary output images resulting from halftoning (Ulichney 1988). Sinclair and Pegram (2005) used the RAPSD to illustrate the effectiveness of the Empirical Mode Decomposition (EMD) to decompose spatial rainfall fields into their intrinsic spatial scale components and Germann and Zawadzki (2002) used the RAPSD to illustrate the effects of advection procedures on the suppression of power in reflectivity fields according to scale (i.e., spatial wavelength). The RAPSD finds utility in this study to provide a tractable and convenient means to illustrate the relative quantitative effects of scale filtering methods.

The RAPSD used in this study is defined as follows. The power spectrum of a 2D image, $f(x, y)$, of dimension $M \times N$, is defined as (Gonzalez and Woods 2002)

$$P(f) \equiv \left|F(u,v)\right|^2, \tag{5.6}$$

where,

$$F(u,v) = \frac{1}{MN}\sum_{x=0}^{M-1}\sum_{y=0}^{N-1} f(x,y)e^{-j2\pi(\frac{ux}{M}+\frac{vy}{N})}. \tag{5.7}$$

Figure 22 shows how spectral estimates $P(f)$ can be partitioned into annuli of width Δ for regular rectangular grids. Each annulus has a central radius, f_r, the radial frequency, and $N_r(f_r)$ frequency samples. The sample mean of the frequency samples of $P(f)$ in the annulus $||f| - f_r| = \Delta/2$ about f_r, is defined as the RAPSD (Ulichney 1988)

$$\overline{P}_r(f_r) = \frac{1}{N_r(f_r)}\sum_{i=1}^{N_r(f_r)} P(f_{r,i}), \tag{5.8}$$

where,

$$f_r = \left[\sqrt{u^2+v^2}\right] \tag{5.9}$$

and $[\bullet]$ represents the nearest integer operator. Spatial radial wavelength (in km) is then given by $\lambda = s/f_r$, where s represents the grid spacing of the data. According to the Nyquist Theorem, the smallest resolvable scale in the data is equal to twice the grid spacing (Su and Clemens 2003). Since the grid spacing of the reflectivity fields used in this study is 0.5 km, the smallest resolvable meteorological scale is 1 km. The maximum radial frequencies corresponding to the radius producing the largest circle wholly contained within the grid are considered.

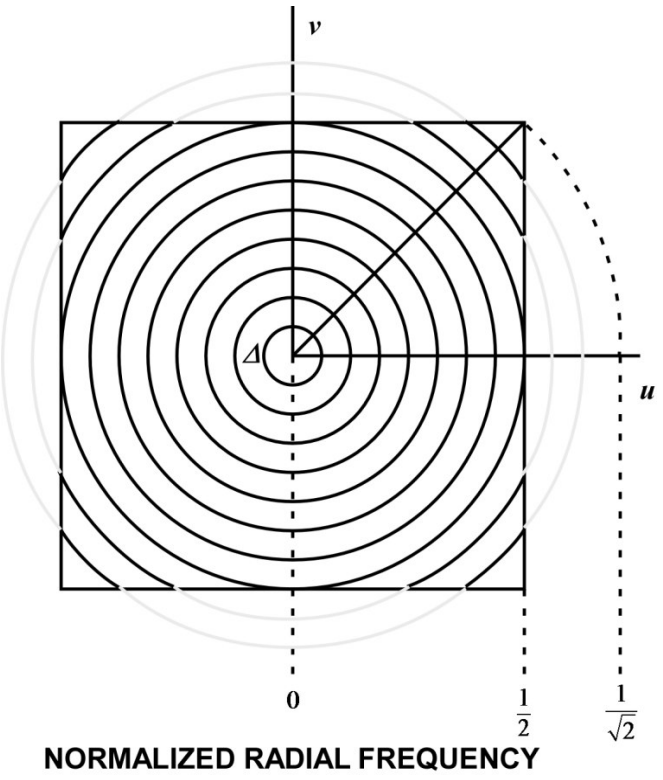

Figure 22. Illustration of the radially averaged power spectrum.

5.3.2 The Critical Success Index

Gerapetritis and Pelissier (2004) presented an analysis to characterize the CSI in terms of FAR and POD. By considering the slope of the CSI function with respect to POD and FAR, they demonstrated that equal changes in FAR and POD produce an equal change in CSI when POD = 1 - FAR. When POD > 1 - FAR, CSI was found to be more sensitive to changes in FAR and when POD < 1 - FAR, CSI was shown to be more sensitive to changes in POD. They showed a more accurate forecast would result in an improvement in both FAR and POD and a corresponding improvement in CSI. Nevertheless, CSI is still considered a valid indicator of nowcasting performance and is considered the primary evaluation score in this study.

5.4 Results

The effect of each filter is illustrated using a reflectivity field from the 31 Mar squall line event depicted in Figure 23. The effects of scale filtering this data are quantified using the RAPSD depicted in Figure 24, which shows that the elliptical filtering process began to suppress power relative to the unfiltered data around the 14 km scale while Fourier filtering began to suppress power around the 4 km scale. Figure 25 compares the line-averaged power spectra along the major and minor axes of an ellipse oriented along the line storm shown in Figure 23 to the corresponding radially averaged power spectrum. Figure 25 shows the reflectivity fields to be fairly isotropic, especially at scales below about 20 km, suggesting and the application of elliptical filtering has a negligible effect on the spectral structure of the data and a fair comparison can be made between the radially averaged power spectra shown in Figure 24.

Figure 26 illustrates the effect of each filter on a 20-min prediction corresponding to the observation depicted in Figure 23. The Fourier and elliptical filtered reflectivity fields were generated by applying each respective filter to the input data sequence used to estimate the motion vector field. In this case, there was no filtering performed on the predicted reflectivity fields. The filtered predicted reflectivity fields were created by applying Fourier and wavelet filters, respectively, to the predicted reflectivity fields. The effects of filtering the predicted images are quantified by the radially averaged power spectra shown in Figure 27, which shows Fourier filtering began to suppress power around the 5 km scale and the wavelet filter suppressed power between the 2 km and 14 km scales relative to the unfiltered predicted reflectivity fields. It is interesting to note the wavelet filter preserves the scales between 1 km and 2 km.

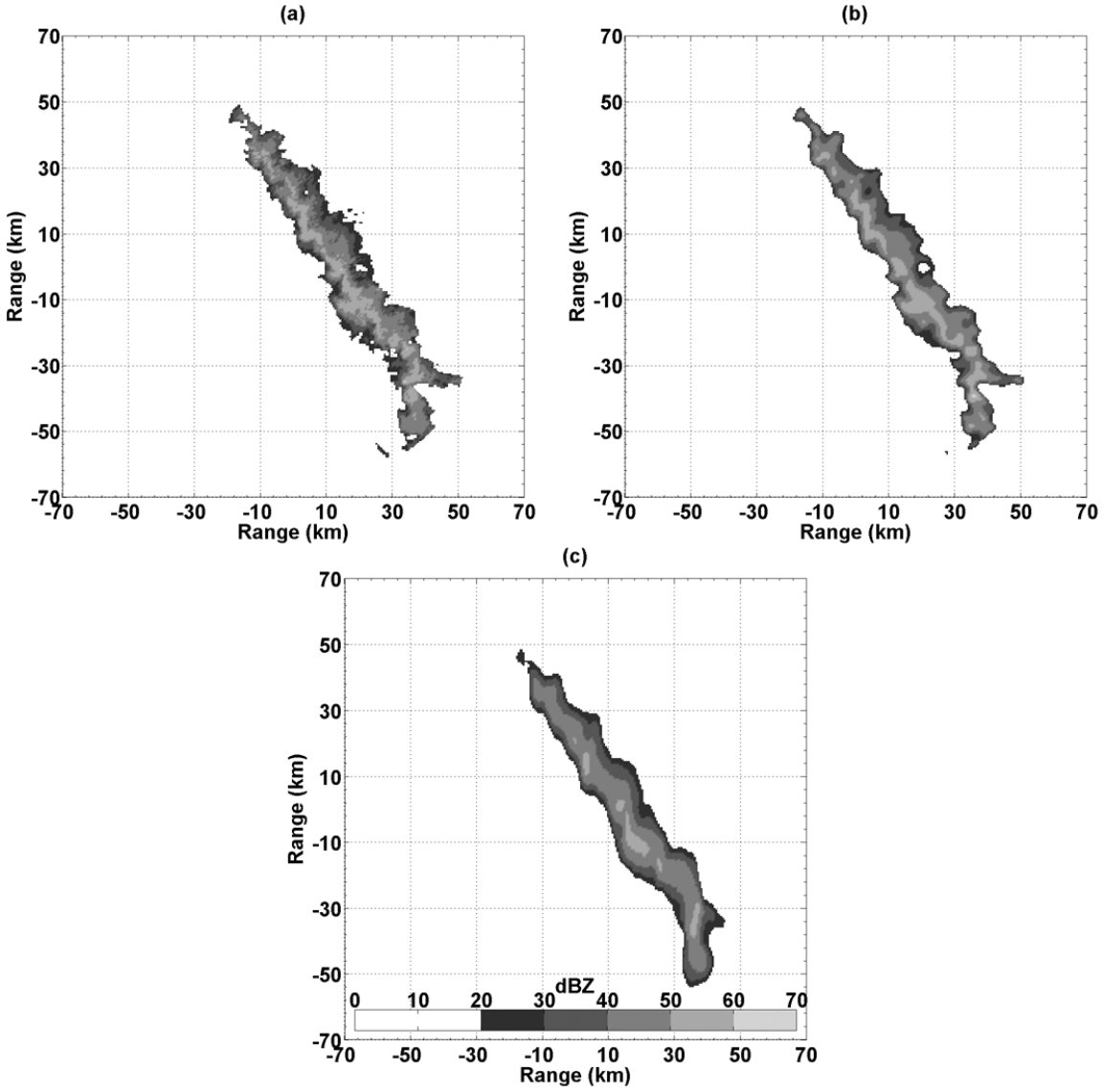

Figure 23. The observation at 0103 UTC 31 Mar 2009: (a) unfiltered, (b) Fourier filtered, and (c) elliptically filtered.

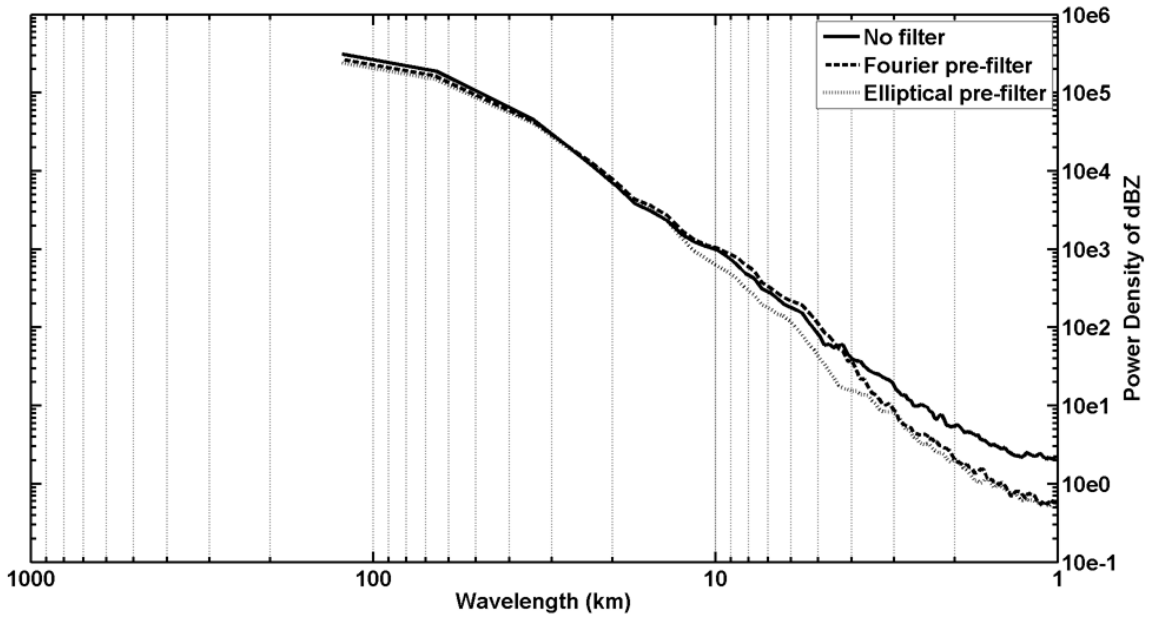

Figure 24. The radially averaged power spectra corresponding to the filtered observations depicted in Figure 23.

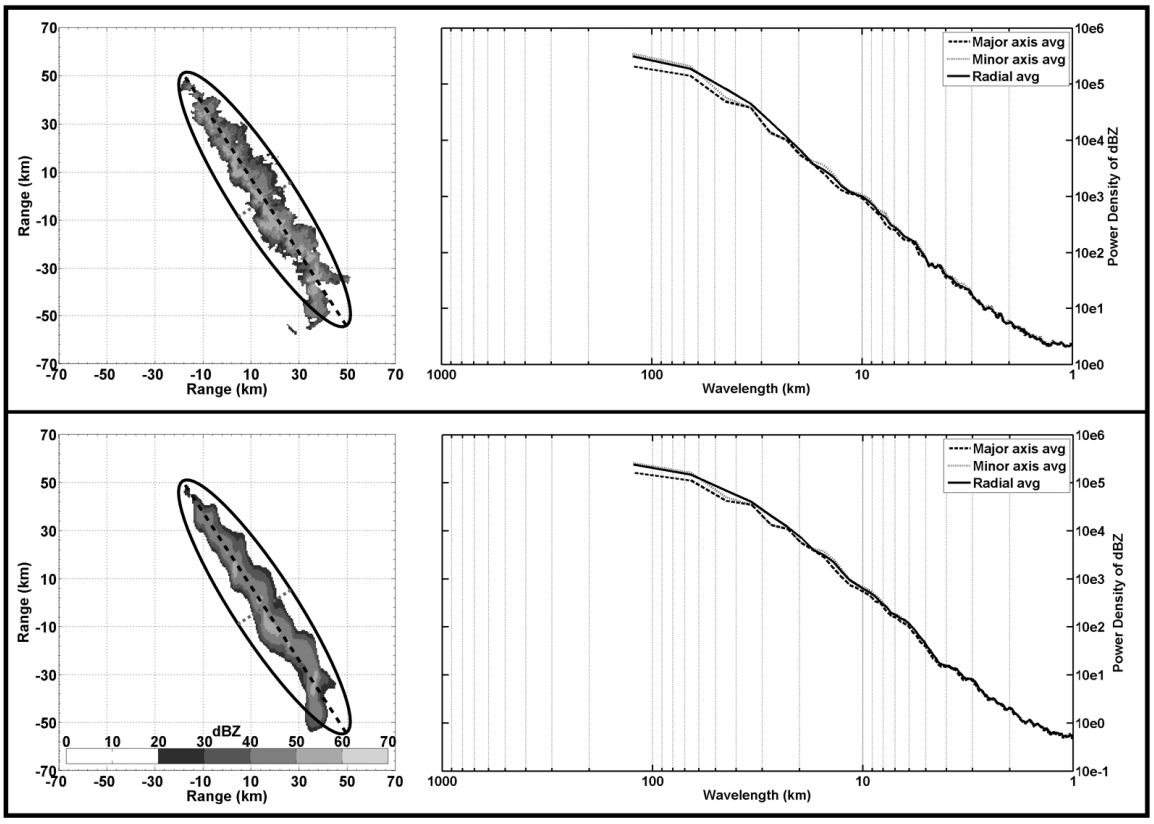

Figure 25. Comparison of the radially averaged power spectrum with the line-averaged power spectra computed along the major and minor axes of an ellipse oriented along the line storm depicted in Fig. 5 for the unfiltered observation (left) and elliptically filtered observation (right).

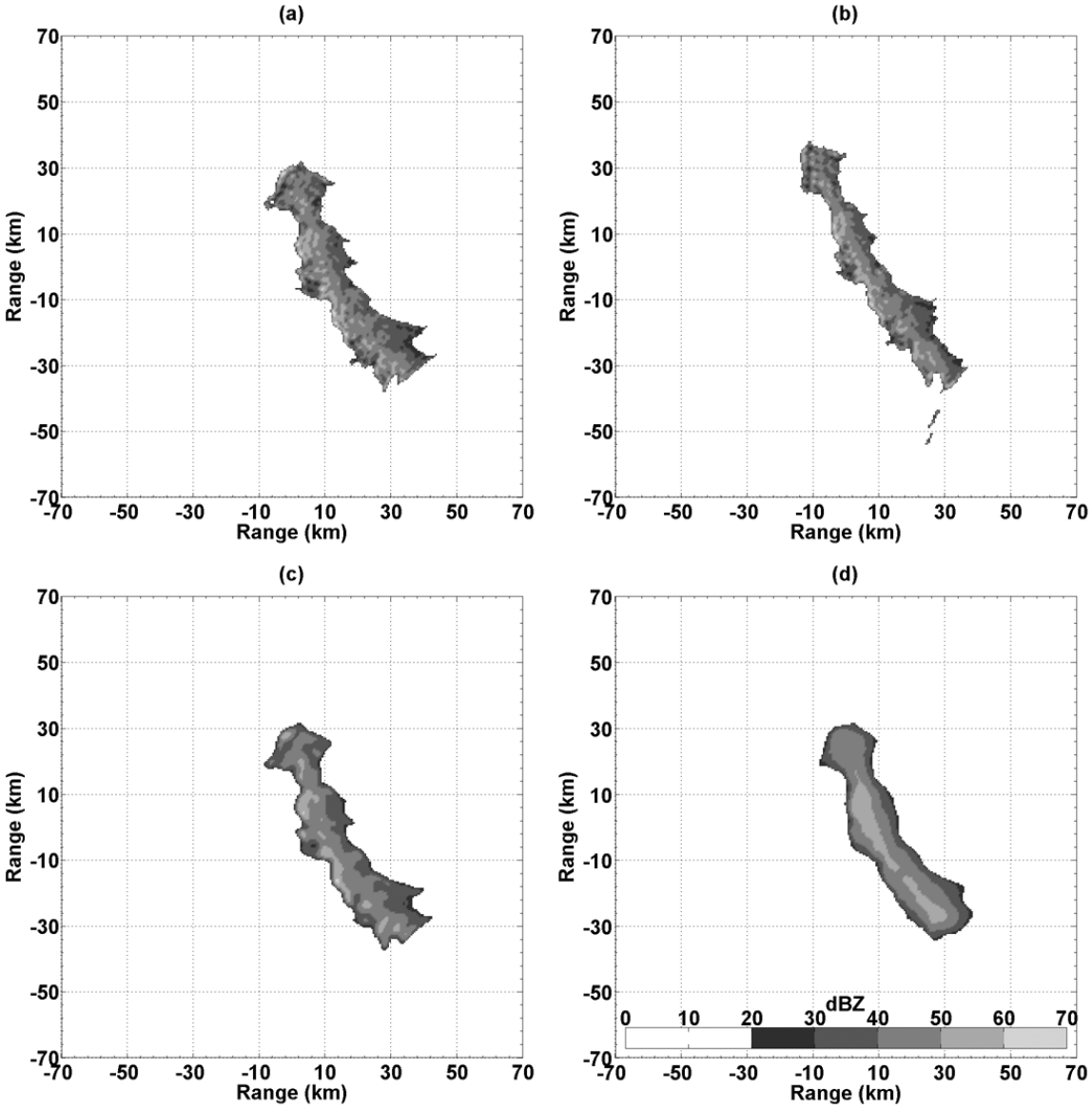

Figure 26. The 20-min prediction corresponding to the 0101 UTC 31 Mar observation: (a) Fourier pre-filtered, (b) elliptical pre-filtered, (c) Fourier pre- + Fourier post-filtered, and (d) Fourier pre- + wavelet post-filtered.

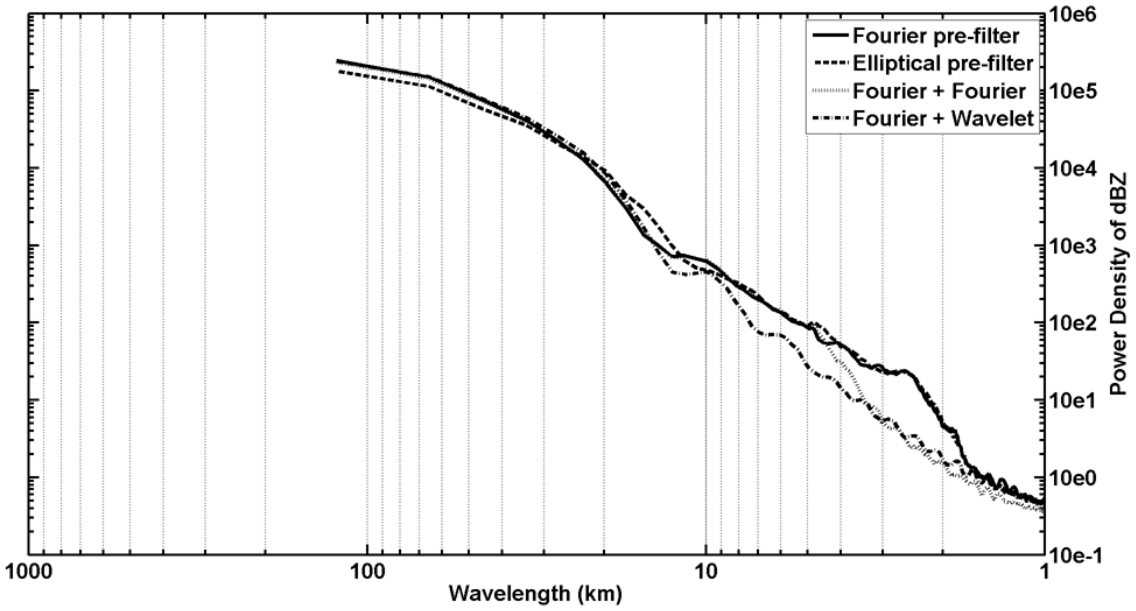

Figure 27. The radially averaged power spectra corresponding to corresponding to the 20-min predictions depicted in Figure 26.

Figure 28 depicts the average CSI (considering a 25 dB*Z* threshold and 1 × 1 km scoring neighborhood) and MAE scores computed over the events in the dataset described in Table 1. The scores were generated by comparing predictions to the appropriate unprocessed reflectivity fields. The 10- and 20-min, mean (averaged over the 20-min lead time period), and mean percent change values corresponding to these results are presented in Table 2. Figure 28 and Table 2 show that applying Fourier filtering in the context of truncating Fourier coefficients in the prediction model provided the best performance in terms of CSI and applying additional Fourier filtering to the predicted reflectivity fields provided the best performance in terms of MAE for lead times up to 20 min. Both the CSI and MAE scores were generated by comparing the resulting predicted reflectivity fields to the corresponding unfiltered observed field.

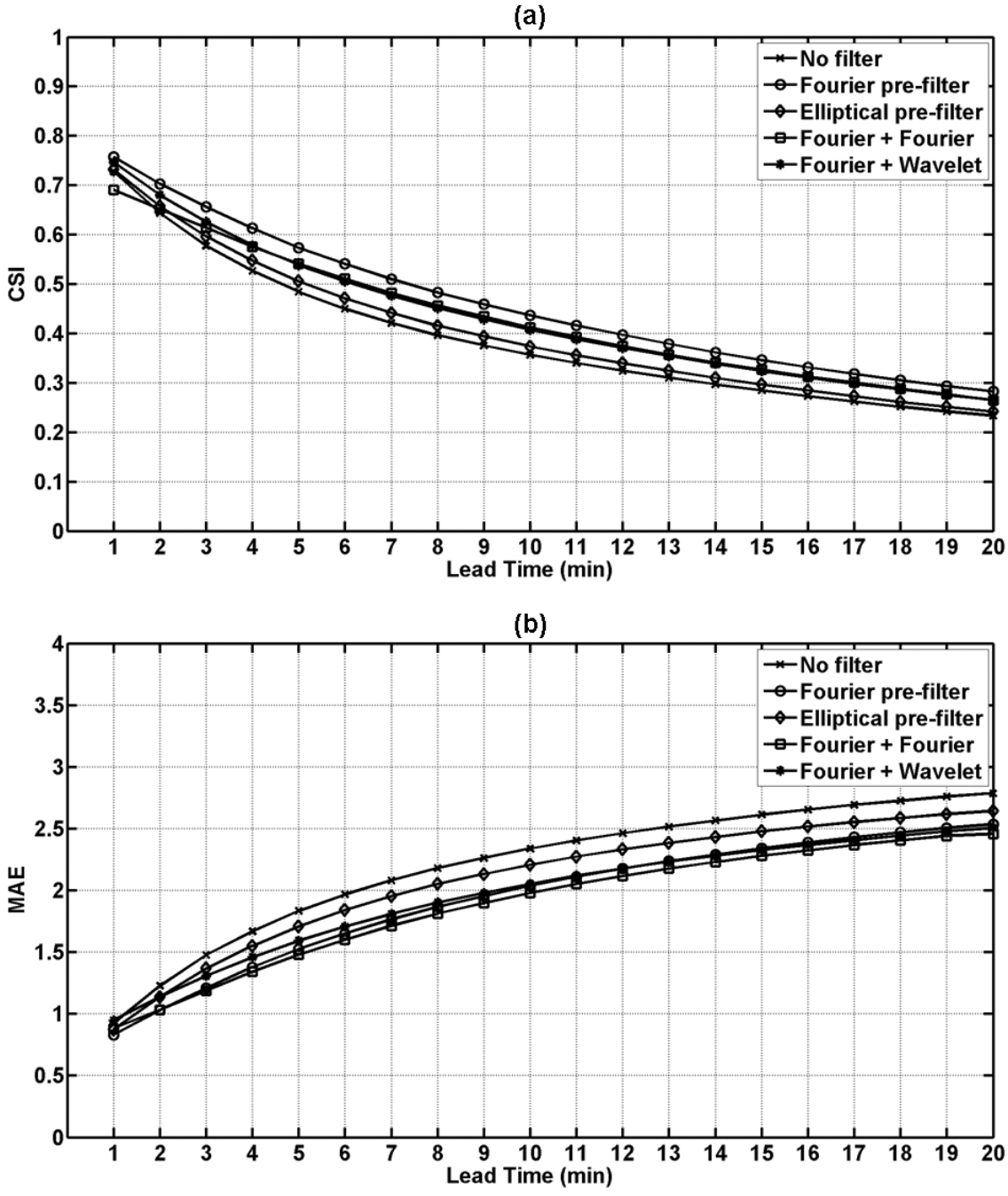

Figure 28. (a) CSI and (b) MAE score comparison for the scale filtering procedures depicted in Figure 19.

Table 2. Summary of nowcasting performance scores for scale filtering analysis (NF = No filtering, FP = Fourier pre-filtering, EP = Elliptical pre-filtering, FF = Fourier pre- + Fourier post-filtering, FW = Fourier pre- + wavelet post-filtering).

Score parameter	Filter				
	NF	FP	EP	FF	FW
10-min CSI	0.3565	0.4362	0.3733	0.4118	0.4070
20-min CSI	0.2334	0.2821	0.2414	0.2647	0.2649
Avg CSI	0.3888	0.4579	0.4033	0.4301	0.4322
%Δ Avg CSI	0.00	17.76	3.72	10.62	11.16
10-min MAE	2.3368	2.0355	2.2061	1.9784	2.0530
20-min MAE	2.7858	2.5348	2.6432	2.4570	2.5044
Avg MAE	2.2061	1.9354	2.0807	1.8877	1.9609
%Δ Avg MAE	0.00	-12.27	-5.68	-14.43	-11.11

5.5 Summary and conclusions

Selectively filtering small-scale features with short lifetimes from precipitation patterns has been shown to improve prediction accuracy in terms of CSI scores when predicting WSR-88D HRVIL and NOWrad composite continental-scale radar data using a cross-correlation-based (Wolfson et al. 1999; Van Horne et al. 2006) and a variational-based nowcasting technique (Turner et al. 2004), respectively.

The effects of Fourier, elliptical, and wavelet filtering techniques on prediction precision using a spectral-based nowcasting algorithm and approximately 66 h (3960 data frames) of high-resolution composite reflectivity data were studied. Each filter was individually tuned for optimal performance based on the results of empirical preliminary studies. The results showed that Fourier filtering in the context of the truncation of spectral coefficients in the prediction model [i.e., reducing the values of N_x and N_y in Eq (3.11) to have normalized cut-off frequencies of 0.2 in each direction] yielded the best performance for lead times up to 20 min in terms of CSI and additionally Fourier filtering the predicted reflectivity fields yielded the best performance in terms of MAE.

Generating predictions based on motion vector fields estimated using Fourier-filtered data without filtering the predicted data showed an approximate 6% and 1% improvements in terms of average CSI and MAE, respectively, over applying the wavelet filtering method to the predicted data. Fourier filtering within the context of truncating Fourier coefficients in the prediction model was also shown to yield an approximate 13% improvement in terms of CSI and 6% in terms of MAE over using the elliptical filtering procedure. Additional filtering of the predicted reflectivity fields using a Fourier low-pass filter showed no increase in CSI but showed an additional approximate 2% improvement in MAE. Any filtering method was shown to improve performance vs no filtering, with the maximum difference being approximately 0.06 (26%) in terms of CSI and 0.3 dBZ (11%) in terms of MAE.

An isotropic Fourier filter as investigated in this study likely more closely matches the spectral structure of the fairly isotropic CASA reflectivity data used in this evaluation (Figure 25) than the elliptical or wavelet filters. These results are consistent with those presented by Zawadzki (1973), who found at scales comparable with a rain cell size (less than 10km), that precipitation is, on average, isotropic. Bellon and Zawadzki (1994) also found that in spite of the marked elongation of a rainfall pattern associated with a frontal passage, the difference between anisotropic and isotropic filtering procedures was barely perceptible and more elaborate and time-consuming anisotropic filtering resulted in a negligible improvement in forecast quality. This provides one explanation why isotropic Fourier filtering yielded the best nowcasting performance in this study. The suppression of scales probably useful for prediction (Figure 24 and Figure 27) dictated by the small-scale nature of the CASA reflectivity data may also provide an explanation of the

difference in nowcasting scores. Bellon and Zawadzki (1994) showed that over-filtering rain rate maps reduced cross-correlation between forecasts and observations. Additionally, the rescaling procedure that is part of the wavelet filtering method can also introduce error. Furthermore, the truncation of Fourier coefficients in the prediction model will affect motion vector field estimation aside from scale suppression afforded by the inherent Fourier filtering. This may further explain the difference in CSI scores between the Fourier-filtered results (via model coefficient truncation) and the elliptical-filtered results (without model coefficient truncation).

CHAPTER VI. IMPROVED SNOW WATER EQUIVALENT NOWCASTING IN THE WEATHER SUPPORT TO DEICING DECISION MAKING SYSTEM

6.1 Introduction

The operation of aircraft during winter precipitation conditions is a significant safety concern. A relatively thin coating of ice on an aircraft wing can cause substantial loss of lift and increase in drag making safe flight impossible. Thus, the formation of ice must be removed or prevented using a deicing fluid prior to take-off.

A key quantity used to assess the type and application frequency of deicing fluid for winter conditions is the snow water equivalent (SWE) value. Accurate short-term forecasts of SWE values are useful to facilitate efficient resource allocation and planning of airport deicing operations. Accurately forecasted SWE values are needed by pilots and ground personnel to assess whether the snow accumulation on an aircraft wing since deicing has exceeded the capability of the deicing fluid to keep the surface ice-free. The Society of Automotive Engineering (SAE) Ground Deicing Committee produces Holdover Tables that indicate the amount of time a deicing fluid can prevent ice formation on an aircraft for a given precipitation type, rate, and temperature. The Holdover Tables are based on testing of deicing fluids at 1 and 2.5 mm h^{-1} liquid equivalent snowfall rates and at various temperatures. Thus, knowledge of the occurrence of rates less than 1 mm h^{-1}, between 1 and 2.5 mm h^{-1}, or greater than 2.5 mm h^{-1} are critical in the proper use of the Holdover Tables. Figure 29 illustrates the SWE categories of interest in this context.

The Weather Support to Deicing Decision Making (WSDDM; Rasmussen et al. 2001, 2003) method was developed to predict SWE values and is currently deployed at several airports in the U. S. WSDDM was also used to provide nowcasting at the Vancouver 2010 Winter Olympic and Paralympic Games (Joe et al. 2010). WSDDM produces nowcasts of SWE values by calibrating the *Z-S* relationship, which relates radar reflectivity to SWE rate, in real-time to account for variability in precipitation density. Extrapolated WSR-88D Level III base reflectivity values are converted to SWE estimates using the *Z-S* relationship calibrated by previous radar observations and surface gauge measurements. Reflectivity values are extrapolated according to motion vectors estimated by a tracking method that maximizes cross-correlation between subgrids in successive data frames.

While WSDDM has shown operational benefit at many U. S. airports, ground clutter mitigation artifacts observed in reflectivity fields generated by the WSR-88D outside of Denver, Colorado, have been shown to severely degrade the accuracy of SWE predictions generated by the WSDDM system deployed at Denver International Airport (DIA). The zero isodop resulting from perpendicular wind direction and scan radial has been shown to produce regions of artificially high correlation between successive base reflectivity fields (Maddox 2010). Because of this, the cross-correlation tracking algorithm was shown to produce erroneous motion vector estimates by fixating on these regions of high correlation. The cross-correlation-based nowcasting algorithm is also well-known to be computationally intensive thus potentially delaying the updates of SWE estimates.

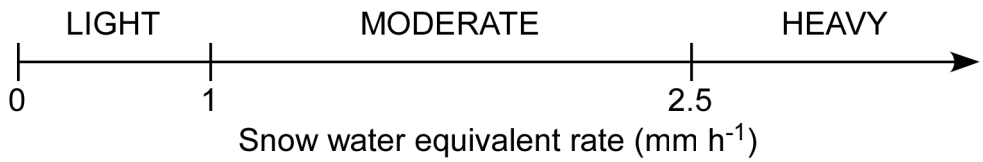

Figure 29. Snow water equivalent categories critical to proper deicing decision-making support.

A method is presented in this section to improve SWE forecasts made by the WSDDM system. The method incorporates DARTS into the WSDDM system by replacing the cross-correlation-based radar nowcasting method currently used. Approximately 69 h of data collected using a WMO standard reference gauge during five winter precipitation events at the NCAR Marshall Field Site and the KFTG WSR-88D near DIA from 2007–2008 was used for evaluation. Results showed an approximate 10% improvement in CSI and a runtime reduction of approximately 2 orders of magnitude for lead times up to 1 h.

6.2 Background

The SWE rate nowcasting algorithm used in WSDDM is based on real-time calibration of the *Z*-*S* relationship, which mathematically relates the radar reflectivity factor (*Z*) to the SWE rate (*S*). A real-time calibration is needed to take into account the natural variations in the *Z*-*S* relationship that occur during a storm because of changes in snow crystal type, degree of riming and aggregation, wetness, and size distribution. By integrating the SWE rate over time, an SWE value is generated.

The *Z*-*S* relationship is shown as

$$Z = aS^b . \tag{6.1}$$

Here, Z is in units of $mm^6\ m^{-3}$ and S is in units of $mm\ h^{-1}$. As a result of this direct relationship, a nowcast of radar reflectivity produces a nowcast of S at a desired location. Likewise, the motion vectors produced by a radar-based nowcasting algorithm used in conjunction with snow gauge, surface temperature, and (optionally) surface wind velocity measurements allow for real-time calibration of parameters a and b in Eq (6.1).

To perform this calibration, S is measured at a desired location at a given time. Then, a search back in time from this location using motion vectors estimated by the Tracking of Radar Echoes by Correlation (TREC; Rinehart and Garvey 1978; Rinehart 1981; Tuttle and Foote 1990; Chornoboy 1994; Li et al. 1995; Li and Lai 2003) algorithm and surface wind speed measurements corresponding to this time and location estimate the location of the precipitation falling into the gauge. The median (linear) reflectivity value corresponding to this location is used to estimate the SWE rate at the gauge. The free parameter a is adjusted such that the estimated liquid equivalent value matches the measured liquid equivalent value by integrating the estimated liquid water equivalent rate, S_e, and the measured liquid water equivalent rate, S_m, respectively, over a given time period. The other free parameter, b, is adjusted based on the measured surface temperature. This calibration procedure is illustrated in Figure 30.

Once calibrated, nowcasts of SWE rate values (S) can be made by applying the calibrated equation to nowcast reflectivity values at the desired location by searching back in time using the combined surface measured and TREC-derived wind vectors. The algorithm runs continuously such that equation parameters and snow water equivalent estimates are updated whenever new radar data becomes available. The WSDDM system diagram is shown in Figure 31.

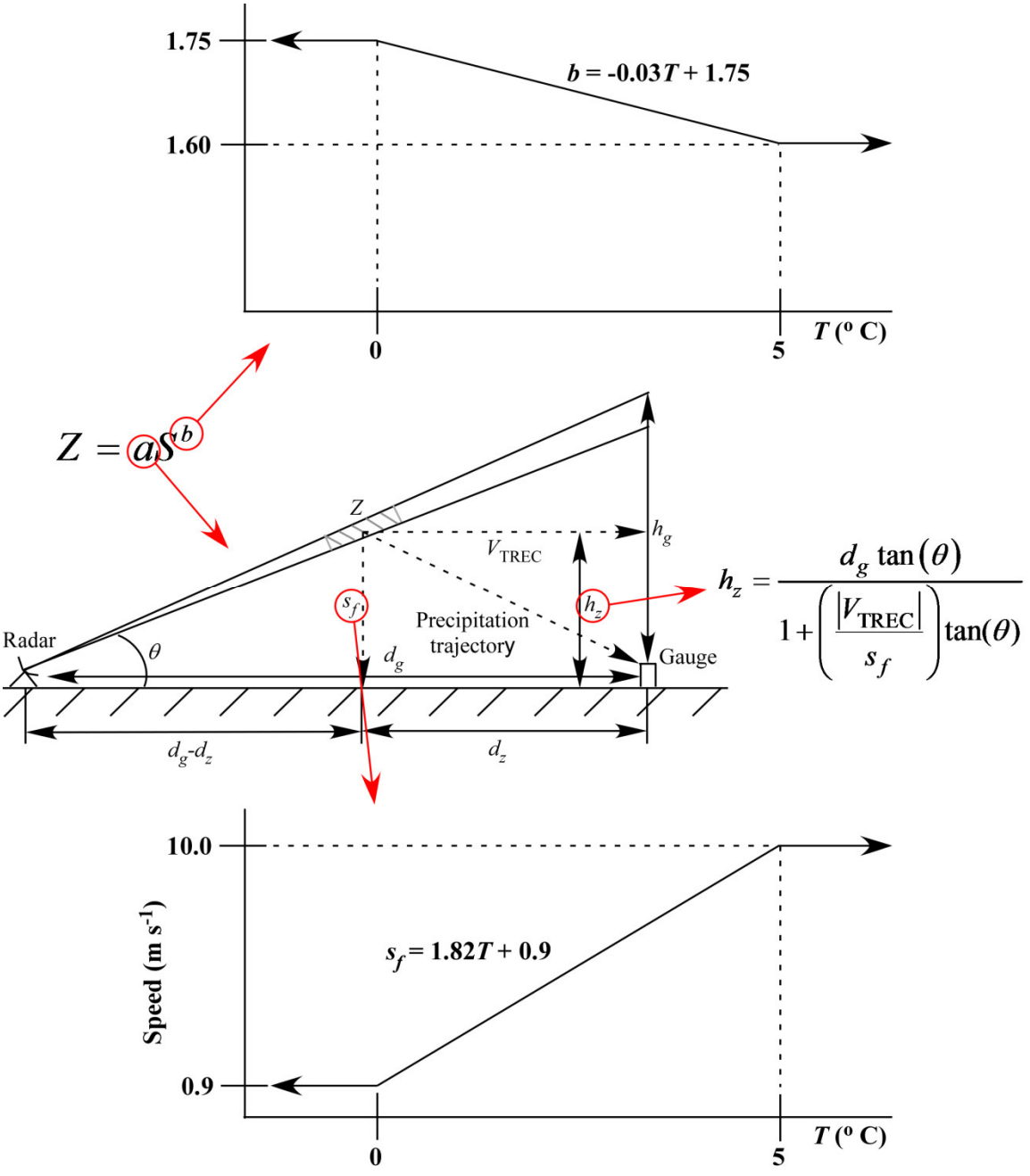

Figure 30. Illustration of the WSDDM *Z-S* calibration procedure.

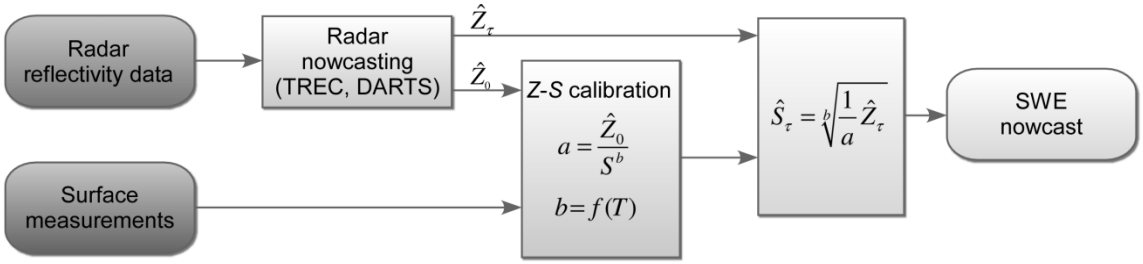

Figure 31. The WSDDM system diagram. The *Z*-*S* equation is calibrated using surface measurements and the initial radar reflectivity estimate, $\hat{Z}_0$. Nowcasts of SWE, $\hat{S}_\tau$, are made using nowcasts of radar reflectivity, $\hat{Z}_\tau$, and the calibrated *Z*-*S* equation.

An integral component of the WSDDM system is the TREC nowcasting algorithm. The TREC algorithm is used to estimate the spatial change between two gridded data fields in time. TREC computes the maximum location(s) of 2D cross-correlation between subsets of two input grids (Cartesian-gridded reflectivity fields are used in the WSDDM system) to generate matrices of motion vectors representing the most probable motion in the horizontal and vertical directions.

The three main steps in the TREC algorithm are summarized as follows:

1) *Determine the global motion vector.* The global motion vector is a single vector that represents the overall (large-scale) motion of the grid in time. The 2D cross-correlation field between two complete grids is computed and the maximum value is found. The distance between the locations of this maximum cross-correlation value and the center of the grid in the horizontal and vertical directions is computed to determine the global motion vector.
2) *Determine the distributed motion vector field.* The motion vector field is a matrix of motion vectors representing small-scale motions within the grid. To compute this field, a subgrid of predetermined size (much smaller than the data grid size) is

centered over each location in the earlier of the 2 input grids. This "feature box" is moved and centered over each location in the older input grid. A feature box in the later grid is centered on the same location as the feature box in the earlier grid. The size of the feature box in the later data field is the size of the first box plus a predetermined maximum data displacement (maximum speed) value. The 2D cross-correlation between these two feature boxes is then computed. The distance between the locations of the maximum cross-correlation value and the subgrid center point is found and a motion vector is computed. This process is repeated for every grid point (or a desired subset of grid points) in the grid and is illustrated in Figure 32.

3) *Check and smooth the motion vector field.* The maximum cross-correlation analysis used by TREC has been found to be sensitive to errors thus requiring error checking and smoothing of the resulting motion vector field. Temporal smoothing is accomplished by linearly weighting previous estimates of the global motion vector and motion vector field with the current respective estimates.

   Gross spatial errors in the motion vector field are corrected by replacing vectors which deviate too much in direction and magnitude from the global motion vector or average of local vectors. An exponential spatial smoothing filter is then applied.

6.3 Data

Data collected during five winter precipitation events (approximately 69 h) were considered in this study which encompassed a range of winter weather characteristics. Details of the events are summarized in Table 3.

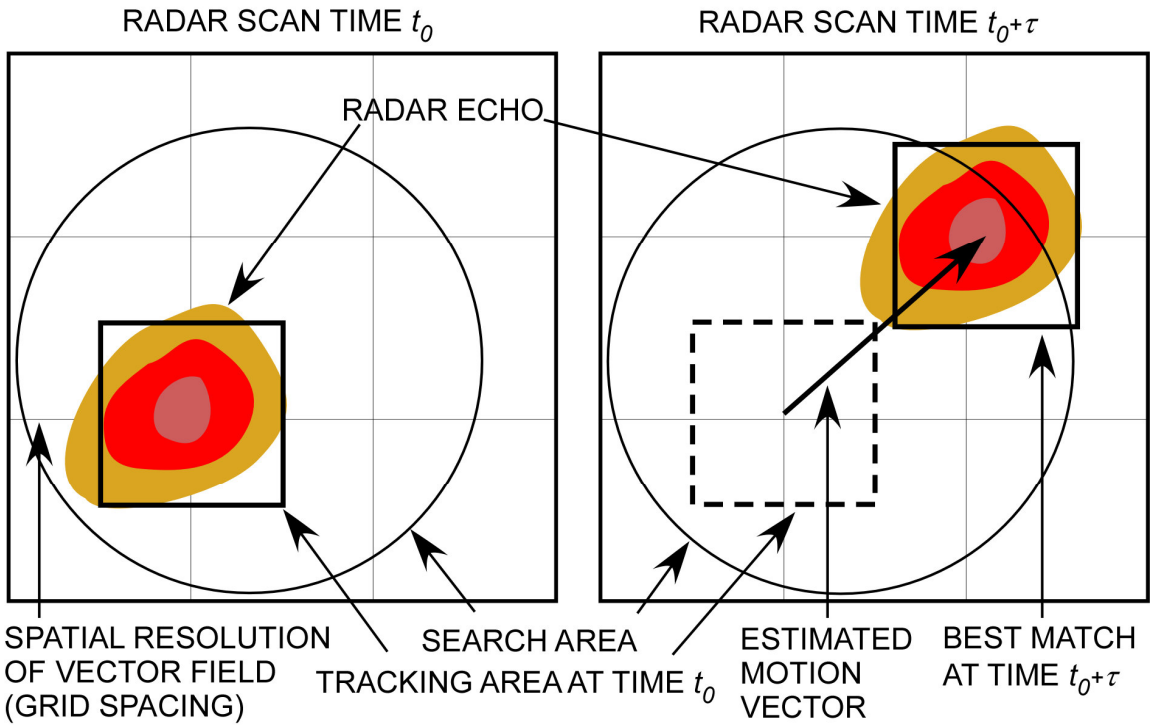

Figure 32. Illustration of the TREC method to estimate a distributed motion vector field. By optimizing a test criterion (correlation coefficient), the best displacement vector is found for each grid point [or a subset of points; from Mecklenburg et al. (2000)].

Table 3. Description of precipitation events used in the evaluation of incorporating DARTS in the WSDDM system.

Start time	Duration (h)	High temp (C)	Low temp (C)	Max wind speed (m s^{-1})	Snow total (mm)	WSR-88D Operating Mode
0404 UTC 21 Oct 2007	14.00	17.8	0.0	14.8	2.5	Precipitation
0008 UTC 11 Dec 2007	14.75	-1.1	-6.7	10.7	170.2	Clear Air
0813 UTC 27 Dec 2007	9.40	-6.1	-11.7	9.4	73.7	Clear Air
0002 UTC 04 Feb 2008	14.60	0.6	-0.56	6.7	58.4	Clear Air
0007 UTC 17 Mar 2008	16.20	2.2	-2.8	9.4	139.7	Clear Air

Surface precipitation data was collected at the NCAR Marshall Test Site (39.9491^{o} lat, -105.1954^{o} lon, 1744 m alt) using a World Meteorological Organization (WMO) standard-reference Geonor Double Fence Intercomparison Reference (DFIR) gauge. A wind shield is a barrier made of wooden or metal strips that prevents wind from blowing the precipitation over the top of the gauge. Previous research has shown that without a wind shield, gauges can under-estimate precipitation by 50% or more during windy events (Landolt et al. 2004). The diameter of a wind shield can also effect the measurement. Wind shields that are sufficiently large cause turbulence in the air flowing over the gauge rather than downward forcing and measurements closer to the accuracy standard set by the WMO (Landolt et al. 2004).The Intercomparison study recommended the double-fence wind shield, which is an octagonal double fence shield, as the accuracy standard (Figure 33). The DFIR shield consists of two concentric rings of fencing at 12 m and 4 m in diameter, with the snow gauge at the center. The snow gauge is surrounded by an additional wind shield at a diameter of about 1.5 m. Thus, the Geonor snow gauge in the DFIR was a triple-shielded gauge reducing wind-induced catchment loss and of the seven wind shields tested by NCAR, the DFIR shield resulted in the greatest catch.

An R.M. Young anemometer was used to collect surface wind velocity data and a Vaisala WXT-510 was used to collect temperature data. Temporal resolution of all surface gauge data was 1 min Gauge measurement errors were ignored in this study.

Radar data consisted of Level III Base Reflectivity products collected by the KFTG WSR-88D radar outside Denver, Colorado (39.7852^{o} lat., -105.5431^{o} lon., 1679 m alt.).

Figure 33. The WMO DFIR Geonor gauge located at the NCAR Marshall Test Site.

Data collected during the lowest elevation angle scan (0.5^{o}) was gridded to Plan Position Indicator (PPI) fields and processed using median filtering and interpolation to remove residual clutter. Data collected during the lowest elevation angle scan is desired in this application for their proximity to the ground. The data were gridded to a spatial resolution of 1 km covering an area of approximately 200 km × 200 km. The data update rate was approximately 5.5 min and 10 min when the radar was operating in Precipitation and Clear Air Mode, respectively. The map of the sensor layout used for this evaluation is shown in Figure 34.

6.4 Results

The performance of WSDDM to nowcast SWE values using TREC as the radar-based nowcasting method was compared to that using persistence blending and DARTS for the data collected from the five winter precipitation events.

Figure 34. Map of the WSDDM evaluation sensor layout.

Table 4 compares the CSI scores and average radar-based nowcasting runtime for this dataset.

Figure 35 shows example reflectivity fields and motion vector fields for both nowcasting methods from the 27 Dec 2007 event. The storm moved in a SE direction and the zero isodop extended from the radar to the SW and NE. The erroneous TREC vectors are apparent and no motion vectors are present over the gauge used for system calibration. The nature of DARTS (i.e., the continuity constraint incorporated in the physical model) allows for accurate motion vector predictions over the gauge site used for system calibration despite the presence of the zero isodop. In each case, WSDDM was run using the latest release of MATLAB on a standard Linux compute server.

Table 4. Results comparing the performance of WSDDM using TREC for radar pattern motion estimation (TREC-WSDDM) and using DARTS for radar pattern estimation (DARTS-WSDDM) for the Marshall dataset. Scores are averaged over the five events.

System/comparison	30-min CSI	60-min CSI	Avg runtime (s)
TREC-WSDDM	0.54	0.55	196.36
DARTS-WSDDM	0.59	0.60	2.58
Δ (%)	+8.75	+9.70	-98.69

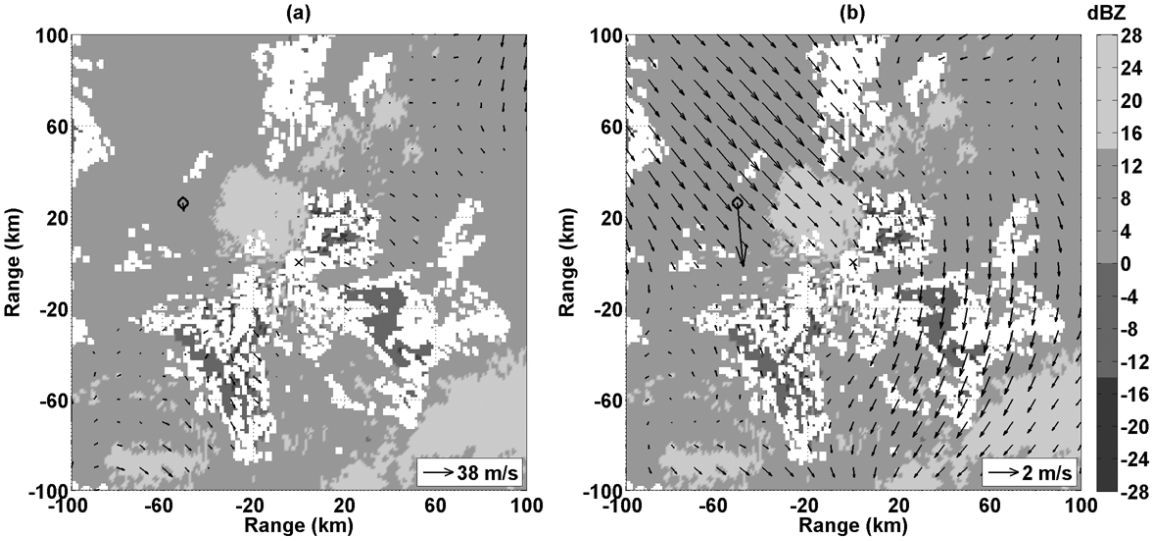

Figure 35. Example reflectivity field and (a) TREC motion vectors and (b) DARTS motion vectors from the 12 Dec 2007 winter storm event. The gauge location is indicated by the 'o' and the radar location by the 'x'. The surface wind vector is shown at the gauge site.

The computational complexities of the DARTS and TREC algorithms can be quantified more formally. Considering an $N \times N$ data field, a forward and inverse Fast Fourier Transform (FFT) operation each with computational complexity $O(N\log_2 N)$ (Cooley and Tukey 1965; Johnson and Frigo 2007), a matrix pseudo-inversion [$O(M^3)$ when considering the modified Golub-Reinsch algorithm (Chan 1982)], and lower-order computations to construct and retrieve the linear system, the overall computational complexity is $O(M^3)$, where $M < N$ is the dimension of the truncated field of FFT

coefficients determined by the choice of parameters N_x and N_y in Eq. (3.11). Considering M is on the order of N and there are on the order of N data fields considered for motion estimation, the computational complexity of DARTS can be given as $O(N^4)$. The computational complexity of TREC is $O(q^2n^2N^2)$ (Tsai and Lin 2003), where q and n ($q < n < N$) are the dimensions of the square sub-template and search area used for pattern matching at each data point, respectively. Both q and n are determined by parameter selection and are on the order of N. The computational complexity of the TREC algorithm can be represented as $O(N^6)$, consistent with the results presented in Table 4.

6.5 Summary and conclusions

The results presented in this section show the utility of replacing the TREC radar-based nowcasting method with DARTS in the WSDDM system to nowcast SWE rates for aviation deicing decision support. The continuity equation upon which DARTS is built allows for more accurate estimation of precipitation pattern motion in the presence of anomalies such as the zero isodop (Figure 35). As a result, SWE estimates using DARTS were shown to be approximately 10% more accurate on average than those made using TREC in terms of CSI scores when considering approximately 69 h of data collected by a WMO DFIR gauge at the NCAR Marshall Test Site and the KFTG WSR-88D. Runtime was also reduced by approximately two orders of magnitude when TREC was replaced by DARTS in the WSDDM system. This savings can be attributed to the efficient linear formulation of the DARTS method. In a more general sense, the results presented in this section show that DARTS performs favorably when nowcasting winter precipitation patterns and relatively low-resolution radar data compared to the data provided by CASA DCAS.

CHAPTER VII. AN INVESTIGATION OF THE PREDICTABILITY OF PRECIPITATION USING HIGH-RESOLUTION COMPOSITE RADAR OBSERVATIONS

7.1 Introduction

The predictability of precipitation patterns observed by meteorological radar is an important concept as it establishes a means to characterize precipitation patterns and provides an upper limit on the extent of useful forecasting. Predictability also varies based on spatial and temporal scales of observed meteorological phenomena. This section describes an investigation of the predictability of precipitation patterns containing microalpha (0.2–2 km) to mesobeta (20–200 km) scales using high-resolution (0.5 km/1 min/1 dB*Z*) composite radar reflectivity data extending the analysis presented by Grecu and Krajewski (2000) and Germann et al. (2006) to smaller scales in space and time. An experimental approach is used where continuous and categorical lifetimes of radar reflectivity fields in Eulerian and Lagrangian space are used to quantify predictability. The results are stratified according to the type of weather event. A practical upper-limit on the extent of nowcasting performance is also estimated. The space-time scale-dependency of predictability is investigated and connections to the predictability of larger-scale features are made. The results show that predictability in terms of lifetime is approximately 14–15 and 20–21 min in Eulerian and Lagrangian space, respectively, and a strong approximation to a linear relationship exists between predictability and space-time structure from microalpha to macrobeta (2 000–10 000 km) scales.

7.2 Background

7.2.1 The predictability of precipitation

The predictability of precipitation is a complex concept. From a purely dynamic point of view, predictability is related to the dependence of the trajectory of the atmospheric state in phase space [i.e., the space in which all possible states of a system are represented, with each possible state of the system corresponding to one unique point in that space (Gibbs 1902)] and small perturbations in the initial conditions. This sensitivity of the trajectory of the atmospheric state to small perturbations in initial conditions is an intrinsic and fundamental property of any nonlinear system referred to as the initial value problem. For a simple, low-dimensional system, the initial value problem can be investigated analytically, but for more complicated systems such as precipitation patterns, the study of predictability becomes more difficult and any approach can only give an estimate of the true predictability (Germann et al. 2006).

A variety of studies have been performed that sought to make inferences about the predictability of the atmosphere with some studies following a purely analytical approach while others were experimental in nature. An example of a purely analytical approach is the evaluation of the Liouville equation, which generalizes Euler's equations of motion to systems that are not rigid (Goldstein 2001), and describes the evolution of the probability density of the atmospheric state in phase space (Gleeson 1966; Epstein 1969) to examine perturbation growth of a dynamic system. Principally, the Liouville equation can be solved analytically for any dynamic system but in

practice such an approach is only applicable to low-dimensional problems [e.g., 1D Riccati equation (Ehrendorfer 1994)].

Several studies of predictability were based purely on observations, such as autocorrelation analysis of the variable of interest (Lorenz 1973; Zawadzki 1973) or studies seeking precursors in the observation space (Bocquet 2002). There also exist a variety of studies employing statistical and numerical weather prediction (NWP) models that combine analytical concepts and observations (Buizza et al. 1999; Ehrendorfer et al. 1999; Massacand et al. 1998; Palmer 2002; Walser et al. 2004). In these methods, predictability was measured by the skill of the model to predict a certain phenomenon as evaluated by statistical comparison with observations or by the growth of initially small perturbations in model phase space using singular vector analysis or ensembles of model runs (Germann et al. 2006).

Several factors contribute to predictability in this sense as used in this study. First, there is persistence of variables, atmospheric phenomena, and processes that are related to precipitation (e.g., cloud water content, instability, and uplift of warm air in a warm front). Second, there is forcing with predictable or partly predictable amplitude (e.g., the diurnal and annual cycle of net radiation, orographic forcing, or Rossby wave dynamics). And, third, there are processes and feedback mechanisms that lead to convergence in phase space (e.g., latent heat release in a convective updraft), which at scales of a few tens of minutes and kilometers leads to stabilization. This is not the case at microscales where latent heat release triggers turbulence, which is non-linear (Germann et al. 2006).

7.2.2 Justification for using an experimental approach

While analytical approaches allow understanding of basic concepts of nonlinearity, perturbation growth, and sensitivity dependence, studies based on idealized systems of dynamic equations or with state-of-the-art NWP models both assume the model to be representative of the true system. Errors in the model structure and/or scale interactions, lack of resolution, inadequate parameterization, parameter uncertainty, problems in boundary conditions if running a regional model, and numerical and computational errors that result hamper such approaches. Wave interactions in the earth's atmosphere produce an energy cascade to both larger and smaller scales. Energy at the smaller scales is removed by molecular dissipation. In a numerical model small-scale energy is erroneously aliased to large scales. These large-scale waves interact with other waves and generate an energy cascade in both directions. The resulting small-scale waves, again, alias energy to the large scales. This accumulation of energy at large scales leads to nonlinear instability and renders a numerical solution meaningless (Grasso 2000). Likewise, no precise definition exists for resolution in regards to numerical modeling (Durran 2000). In practice it is difficult to separate the problem of predictability into a component associated with initial error and a component associated with model error (Palmer 2002). Thus, the validity of the results of predictability studies using NWP models can be very sensitive to model errors.

Experimental approaches also have shortcomings, namely, measurement errors exist and the difficulty connecting the results of such analyses to the nonlinear nature of the underlying system. The formation of precipitation in a numerical weather

prediction model may be closer to the real atmospheric system than the simplistic concept of Lagrangian persistence of radar data, yet Germann and Zawadzki (2004) stated that the precipitation physics of current models are oversimplified. Despite these shortcomings, the concept of taking the skill of a forecasting technique, such as persistence of radar precipitation patterns, as a measure of predictability follows Lorenz (1973) who said, "Regardless of what may be indicated by theory, a conclusive proof that partial predictability exists at a given range would be afforded by any demonstration that at least one forecasting procedure exhibits skill at that range." Thus Lorenz suggested predictability is a concept better taken in a relative sense (i.e., relative to a method of forecasting) and the Lagrangian persistence forecasting model can thus not only be used for nowcasting but also as tool to measure predictability of precipitation patterns.

It is possible to obtain a quantitative estimate of the predictability of precipitation by examining the Eulerian and Lagrangian persistence of radar precipitation patterns, where quantitative measures and the skill of forecasts obtained from Eulerian and Lagrangian persistence nowcasts of radar data are taken as measures of predictability. An Eulerian persistence nowcast is obtained by keeping the latest radar observation frozen and considering this image for all future predictions up to a desired forecast lead time. By advecting the precipitation patterns following the field of estimated storm motion a Lagrangian persistence forecast is obtained. The forecast data are then compared to observations at the given lead times to calculate correlation, lifetime, and skill scores. Since this approach is conceptually simple, an easy-to-interpret measure of predictability of precipitation patterns is obtained that can be applied to a large

sample of data. Calculation of lifetime and scores can be stratified according to spatial and temporal scales, location, time, and precipitation pattern type in order to determine the dependence of predictability on these parameters. A similar stratification of predictability is not straightforward when using a numerical weather prediction model because design and implementation of a model both have a significant influence on the performance at different scales, locations, and in different weather situations (Germann et al. 2006).

7.2.3 Previous experimental approaches using radar data

Zawadzki et al. (1994) presented a detailed study on the predictability of precipitation using rain rate fields and the Lagrangian persistence paradigm as the measure of predictability. They defined predictability of precipitation as the ability to forecast precipitation over an area by Eulerian and Lagrangian persistence and considered the maximum forecast time lags where the skill of Lagrangian persistence exceeded the skill of climatology in terms of mean-square error of rain rate as nowcasting model skill thresholds. They also attempted to relate a range of predictability to larger-scale meteorological parameters [e.g., thermal wind, wind shear energy, helicity, geostropic vorticy, convective available potential energy (CAPE), and the bulk Richardson number]. They considered 11 precipitation patterns depicted by 4 km/10 min 2–3 km CAPPI data fields with each event lasting 2–4 h and encompassing a wide range rain event types collected by a single radar on Montreal Island, Quebec, Canada. They found that all forecast skill was lost between 40–112 min, depending upon the individual case, and that observations first smoothed with a 16-km moving-average filter were predictable up to 120 min. They found significant

storm-to-storm variability in the predictability of precipitation fields but were unable to relate this variability to synoptic-scale meteorological parameters.

Grecu and Krajewski (2000) used a dataset consisting of 145 days of volume scans observed by the WSR-88D at Tulsa, Oklahoma, to evaluate three nowcasting schemes, Eulerian persistence, Lagrangian persistence, and a neural network approach, and calculated the predictability of precipitation patterns as a function of forecast resolution. They defined predictability limits as the forecast lead time when an efficiency coefficient, E, becomes negative and the lead time when the correlation coefficient between prediction and observation falls to a value equal to 0.5. They considered a range of spatial resolutions between 4 km × 4 km and 32 km × 32 km at 6 min temporal resolution. Their results showed that large-scale precipitation features were characterized by longer Lagrangian persistence and consequently precipitation fields were only predictable at scales that exceeded 20 km after 60 min.

The use of a single radar put an upper limit to the scales of observations, and, consequently, also to the timescale over which the forecast was useful (Germann and Zawadzki 2002). To address this issue, Germann and Zawadzki (2002) considered the lifetime of precipitation patterns in Eulerian and Lagrangian space derived from continental-scale composite (i.e., the vertical maximum value measured by any WSR-88D radar in the given space-time frame of one location) reflectivity fields as the definition of predictability. The measures of predictability introduced by Germann and Zawadzki (2002) were the lead time when the cross-correlation function between observed and forecast reflectivity fields decays to $1/e$ and the lead time when the ETS falls to a value of 0.3. Spectral and spatial filters were also used to decompose

precipitation patterns according to scales for two reasons. First, Bellon and Zawadzki (1994) showed that applying a spatial filter to the forecast data improved the RMS error where increasing smoothing windows for increasing lead times were used to prevent structures from being reproduced beyond their lifetimes. Secondly, by calculating the correlation between forecast and observation as a function of scale, scale-dependence of predictability was determined. Their work thus introduced the framework for investigating predictability of precipitation and presented first results. They found the range of predictability increased with increasing scale and concluded that filtering efficiently increased the lifetime of precipitation patterns if the predictability is predominantly limited by the smallest scale present in a radar observation.

This methodology to characterize predictability was adopted by the other papers in the series (Germann and Zawadzki 2004, Turner et al. 2004, Germann et al. 2006). Germann and Zawadzki (2004) extended the method of persistence of radar precipitation patterns to produce probabilistic forecasts. Instead of predicting the precipitation for a given lead time and position, forecasts of the probability that precipitation at a given lead time and position exceeds a given threshold were made. Turner et al. (2004) applied measures of scale-dependent predictability to the forecasting method itself, designing forecast filters that reduced RMS errors and improved CSI scores. They showed nowcasting performance was improved using a wavelet filter. Germann et al. (2006) investigated scale dependence of precipitation by applying this wavelet filter in the following manner. Two scale-dependent variations of the Lagrangian lifetime parameter were applied to the observations and

forecasts of this study: low-pass lifetimes (i.e., lifetimes of observations computed after applying a low-pass filter) of spatially filtered observations and forecasts and bandpass lifetimes (i.e., lifetimes of observations computed after applying a band-pass filter) calculated from wavelet spectra and cospectra. For low-pass lifetimes, features smaller than a cutoff scale were eliminated from forecasts and the verifying observations. Features below the cutoff scale were removed by block-averaged smoothing around each point, with side lengths representing different linear cutoff scales. This removed details at scales considered smaller by the two-dimensional Haar wavelet transform. Low-pass lifetimes were then calculated by integrating under the curve of correlation between the set of low-pass filtered forecasts (from a particular forecast time) and the low-pass filtered versions of the verifying observations. Bandpass lifetimes were calculated using a measure of the coherence between forecasts and observations as a function of scale. Integrating this expression over all forecast lead times provided a measure of lifetime for each spatial scale.

Germann et al. (2006) also investigated two other factors influencing limits of the predictability of precipitation. First, they examined the relative importance of growth and dissipation on forecast error. There are two sources of forecast uncertainty when using Lagrangian persistence of precipitation patterns: growth and dissipation of precipitation and changes in the storm motion vector field. To determine the relative importance of these two limiting factors, they performed the following experiment. They first determined the correlation function between observation and forecast and the corresponding lifetime assuming stationary storm motion. Radar patterns were advected along the trajectories derived from a single motion vector field that had been

calculated at the time when the forecast was issued using the radar data of the past hour (i.e., standard Lagrangian persistence forecasting). They then computed the correlation function between the observations and forecasts and the corresponding lifetime taking into account the evolution of the storm motion vector field. Instead of using a single motion vector field, they used a time series of motion vector fields calculated a posteriori using all data over the entire forecast period. Finally, they took the difference of the correlation function and lifetime between the two as a measure of the importance of changes in the storm motion vector field. Second, they investigated the space and time scales that significantly influenced changes in the motion vector field. They determined the lifetime of Lagrangian persistence with nonstationary motion for a set of motion vector fields with different spatial (2600, 520, 200, and 104) and temporal (8 h, 4 h, 2 h, 1 h, and 15 min) resolutions using data from a single 60-h precipitation event.

Germann and Zawadzki (2002) and Germann et al. (2006) investigated the predictability of precipitation patterns using continental-scale NOWrad [2720 km × 2720 km, macrobeta scale and masoscale defined by Orlanski (1975) and Fujita (1981), respectively] radar reflectivity composites with 4 km/15 min resolution using a threshold of 10 dB*Z*. Germann and Zawadzki (2002) considered four events (78 h total) and Germann et al. (2006) extended this dataset to include five rainfall events and three wet periods for a total of 1424 h of data. They stated there were several sources of errors when using radar measurements to estimate precipitation rates. Apart from convolution and blocking (Pellarin et al. 2002) the transformation from radar reflectivity, *Z*, to precipitation rates, *R*, also introduces uncertainty since the *Z*-*R*

relationship depends on the type of hydrometeors and its size distribution. Thus, variability of the *Z-R* relationship can lead to significant errors, in particular at small scales (Lee and Zawadzki 2005). Germann and Zawadzki (2002, 2004), Turner et al. (2004), and Germann et al. (2006) neglected these inadequacies and assumed that the distribution of radar reflectivity represented the precipitation field.

Germann et al. (2006) stated, "The experimental approach presented in this series of papers provides valuable contribution to the fundamental question of predictability. Its strength lies in its simplicity." The studies by Germann and Zawadzki (2002) and Germann et al. (2006) were practically significant in two ways. First, they provided a baseline against which any forecasting technique can be evaluated. Second, they determined the predictability of precipitation as a function of space-time scales. These points are extended in this study to microscale precipitation phenomena by performing similar analyses using CASA radar data.

Germann and Zawadzki (2002) also stated, "Note that, based on the analyses presented here, nothing can be said about the lifetime of scales with wavelengths smaller than 10 km." Germann et al (2006) also stated, "Given the discretization of our input data of 5 dB*Z*, 15 min, and 4 km, features at or below the lower end of the mesogamma scale are not sampled at a sufficiently high resolution. Examples of such features are individual convective cells, turbulence in the melting layer, or drop sorting. Input data with higher resolution and a different setup would be required if emphasis is on these small-scale phenomena." The 4 km spatial resolution (mesogamma scale) includes thunderstorms (Orlanski 1975) but does not include microalpha scale meteorological phenomenon such as wind circulations, cloud

patterns, tornadoes, and deep convection (NWS 2009; Orlanski 1975), or misoscale meteorological phenomena include microbursts and rotation within thunderstorms (Fujita 1981; NWS 2009). From the perspective of seeking forecast certainty, previous studies of Eulerian and Lagrangian persistence of radar precipitation patterns from the storm to synoptic scales took an important step towards understanding the predictability of precipitation. Another important step is taken here by examining the Eulerian and Lagrangian persistence of microscale precipitation patterns and comparing the results to those attained from previous studies that investigated predictability of larger scales.

7.2.4 Predictability of precipitation using high-resolution radar data

This study investigates the predictability of microalpha scale (0.2–2 km; Orlanski 1975) and misoscale (0.4–4 km; Fujita 1981) precipitation patterns from 66 h of mesobeta scale (20–200 km; Orlanski 1975) and mesoscale (4–400 km; Fujita 1981) CASA composite reflectivity observations with 0.5 km/1 min/1 dBZ resolution spanning an approximate 140 km × 140 km coverage area collected during the 2009 IP1 experiment as described in Table 1. CASA composite radar reflectivity observations include Mesoscale Convective Complex (MCC), Mesoscale Convective Systems (MCS), and squall lines (NWS 2009; Orlanski 1975) and provide suitable spatial extent to observe microalpha scale phenomena given that microalpha scale phenomena typically last a few min to 1 h (Orlanski 1975). The coverage area is thus sufficient as the likelihood of a precipitation pattern will move more than 140 km in the lifetimes of microscale precipitation features is small.

7.3 Methodology

7.3.1 Estimation of Lagrangian persistence

This study used DARTS and the sinc kernel-based advection method to provide the estimates of Lagrangian persistence. DARTS was used with the same settings as those described in Chapter V. The sinc kernel-based advection method preserves small scales in predicted reflectivity fields during advection necessary to assess the predictability of small-scale features. This is illustrated by comparing the RAPSD of an observation and corresponding prediction from the 31 Mar event (Figure 36).

7.3.2 Assessment of predictability

This study considers "continuous" and "categorical" lifetimes of radar observations to quantitatively assess the predictability of precipitation. While several other scores can be considered for this purpose (Grecu and Krajewski 2000), these two quantities were chosen for simplicity and to compare the results presented here to those found in literature for larger-scales.

The continuous lifetime is considered to be the lead time, τ, when the correlation function, $c(\tau)$, between observed, $\Psi(t_0+\tau,\mathbf{x})$, and forecasted, $\hat{\Psi}(t_0+\tau,\mathbf{x})$, reflectivity fields in the domain, Ω, shown as (Zawadzki 1973),

$$c(\tau)=\frac{\iint_{\Omega}\hat{\Psi}(t_0+\tau,\mathbf{x})\Psi(t_0+\tau,\mathbf{x})d\mathbf{x}}{\left[\iint_{\Omega}\hat{\Psi}(t_0+\tau,\mathbf{x})^2 d\mathbf{x}\iint_{\Omega}\Psi(t_0+\tau,\mathbf{x})^2 d\mathbf{x}\right]^{0.5}}, \tag{7.1}$$

decays to a value of $1/e$. The correlation function quantifies the linear association and phase (displacement) error between variables (Wilks 2006).

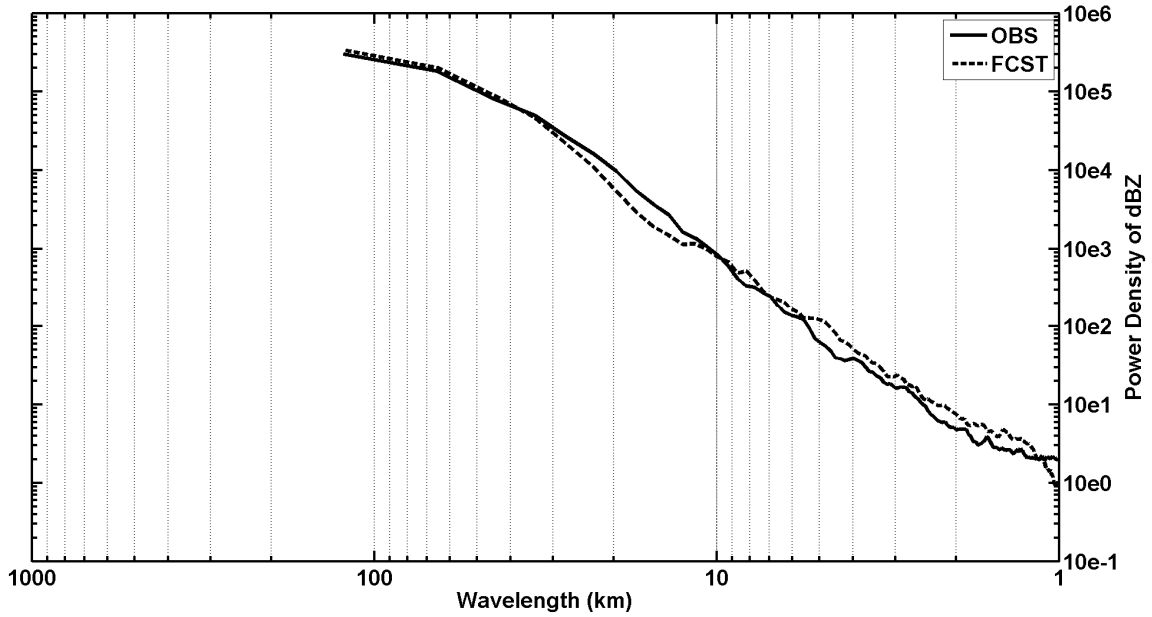

Figure 36. Radially-averaged power spectra of a 20-min forecast (FCST) and the corresponding observation (OBS) from the 31 Mar 2009 event depicting the numerical diffusion characteristics of the sinc-based advection scheme.

The categorical lifetime is considered to be lead time when the Equitable Threat Score (ETS), also known as the Gilbert skill score (Gilbert 1884; Mason 2003),

$$\mathrm{ETS} = \frac{A - A_{\mathrm{RANDOM}}}{A + B + C - A_{\mathrm{RANDOM}}} \quad \text{and} \tag{7.2}$$

$$A_{\mathrm{RANDOM}} = \frac{(A + B)(A + C)}{A + B + C + D}, \tag{7.3}$$

where A represents the intersection of the areas over which the event was forecast and subsequently occurred, B represents the area over which the event was forecasted and subsequently did not occur, and C is the area over which the event occurred but was not forecast to occur, and D represents the intersection of the areas over which the event was not forecast to occur and did not occur, falls to a value of 0.3. This value corresponds approximately to POD and FAR values both being equal to 0.5. The ETS was chosen to quantify predictability because of its straightforward interpretation and

wide-spread use for verification of rainfall predicted by NWP models (Mesinger 2008; Weygandt et al. 2004), where the (asymptotic) "equitability" allows scores to be compared more fairly across different regimes and across different events (Hogan et al. 2010). Values of the ETS range from -1/3 to 1, with a zero-score indicating no skill, a negative score indicating more skill is attained by chance, and a score of unity indicating a perfect forecast.

Like the CSI, the ETS depends on threshold and scoring neighborhood parameters and, in general, will behave similarly to but exhibit lower values than the CSI as forecast "hits" due to random chance are removed (Schaefer 1990). A threshold of 25 dBZ and scoring neighborhood of 1 km × 1 km were used in this study. The ETS has been shown to be sensitive to hits (Accadia 2003), directly proportional to bias (Mason 1989; Hamill 1999), and inversely proportional to phase errors (Baldwin et al. 2006) and rare events (Stephenson et al. 2008).

The shortcomings of the ETS (e.g., Hogan et al. 2010) can be mitigated and a more complete analysis of the predictability of precipitation can be made by considering the results of continuous and categorical predictability collectively. A relationship exists between the scores of a categorical (or dichotomous) forecast and the errors of a continuous precipitation forecast, but Tartaglione (2010) showed that a strict one-to-one relationship does not exist between them. He asserted the precipitation intensity or amount, the chosen threshold, and the manner in which precipitation is distributed can alter the score values and consequently such relationships. Categorizing precipitation causes a loss of information about the numerical values of precipitation and a direct link between the dichotomous score and

the continuous forecast errors might not be possible. This suggests multiple quantitative assessment methods should be used to assess the predictability of precipitation in the manner presented here. Thus, the correlation function and ETS were chosen to assess predictability based on the numerical accuracy and skill of the forecasts, respectively.

7.4 Data

The complete dataset described in Table 1 was used in this study. Spatial scale-dependency was investigated by degrading the resolution of the predicted fields to 1, 2, and 4 km via moving-averaging linear reflectivity values at each grid point using square filter kernels of appropriate side lengths. Example observations at 0.5, 1, 2, and 4 km resolutions are shown in Figure 37. Dependence on temporal resolution was investigated by downsampling the temporal sequence of radar observations and then resampling the sequence back to the original length by inserting the last observed data frame between downsampled frames (i.e., data frames were reinserted according to Eulerian persistence). This process is illustrated in Figure 38. Example motion vector field estimates generated by DARTS corresponding to the observations at spatial resolutions shown in Figure 37 are shown in Figure 39. Example motion vector field estimates corresponding to the data sequence at 0.5 km resolution for 1, 2, 4, and 8 min temporal resolutions are shown in Figure 40. Figure 39 shows relatively low sensitivity of the motion vector field estimates to changes in spatial resolution while Figure 40 shows that degrading temporal resolution has a marked effect on the motion vector field estimated by the DARTS model. A history length of 10 data frames (10 min) for assimilation into the DARTS model was considered in this study.

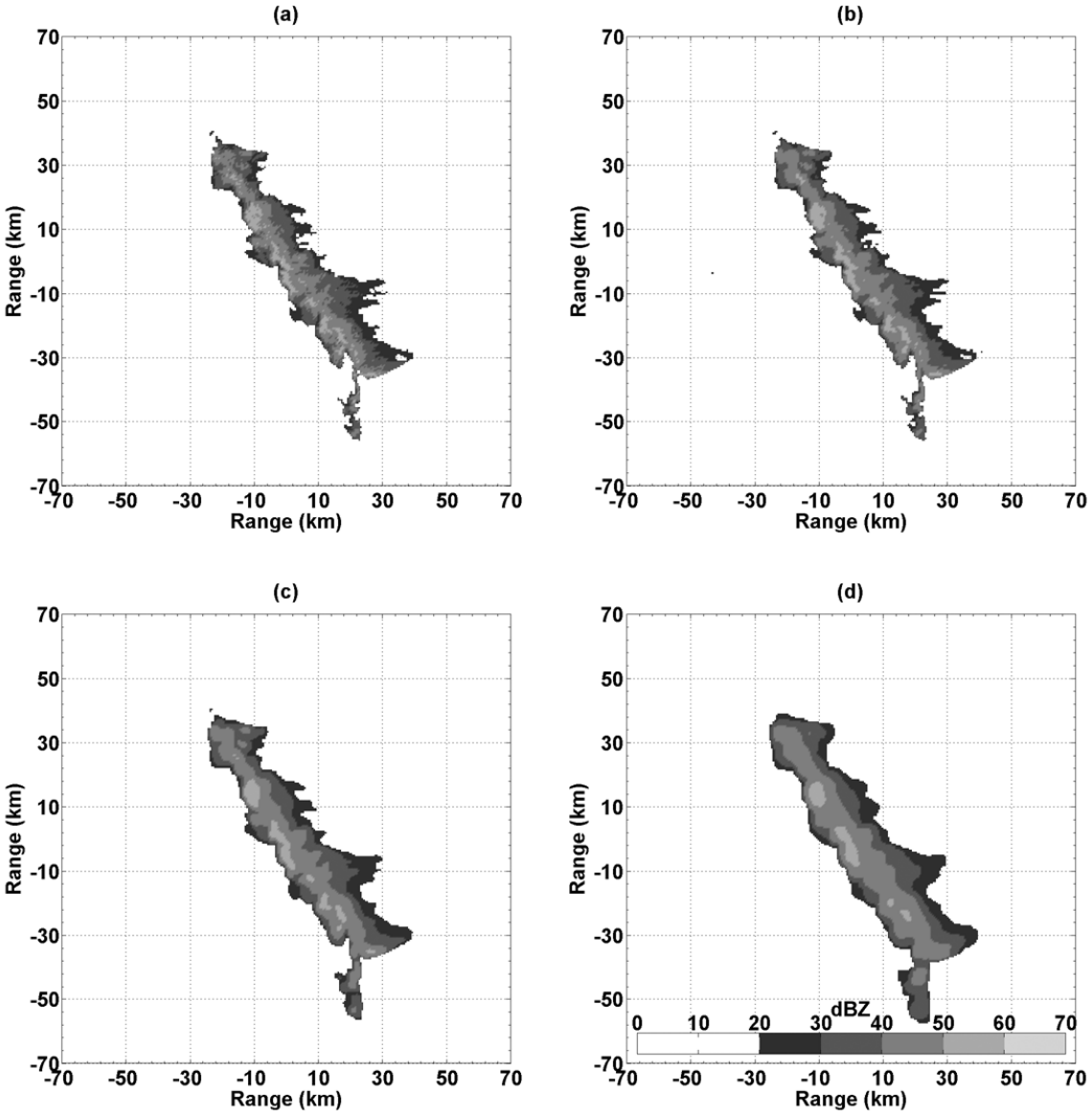

Figure 37. Reflectivity observations at 0103 UTC 31 Mar 2009 at spatial resolutions of (a) 0.5 km, (b) 1 km, (c) 2 km, and (d) 4 km.

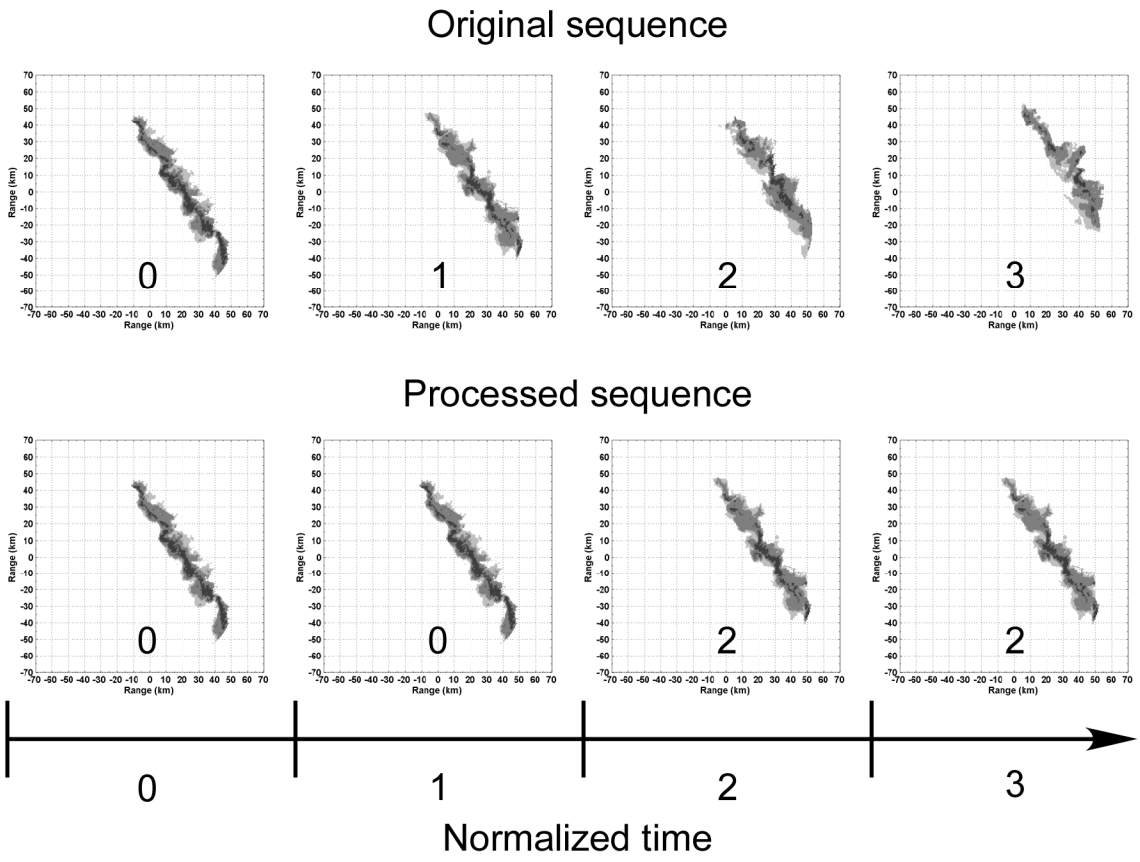

Figure 38. Example reflectivity observation sequence from the 31 Mar 2009 event processed for one-half the original resolution to analyze the effect of temporal resolution on predictability.

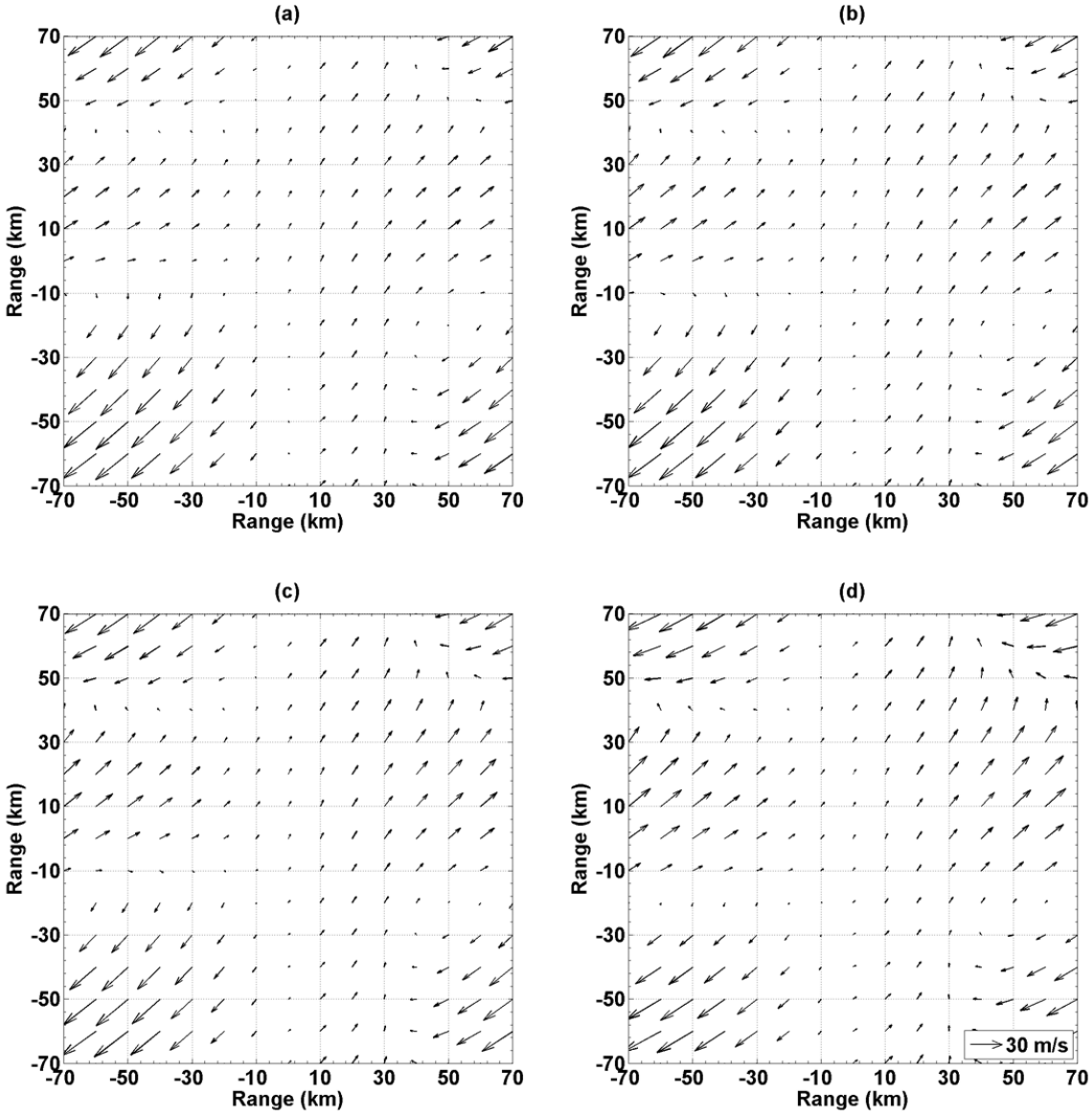

Figure 39. Example motion vector field estimates for the reflectivity fields depicted in Figure 37, for spatial resolutions of (a) 0.5 km, (b) 1 km, (c) 2 km, and (d) 4 km.

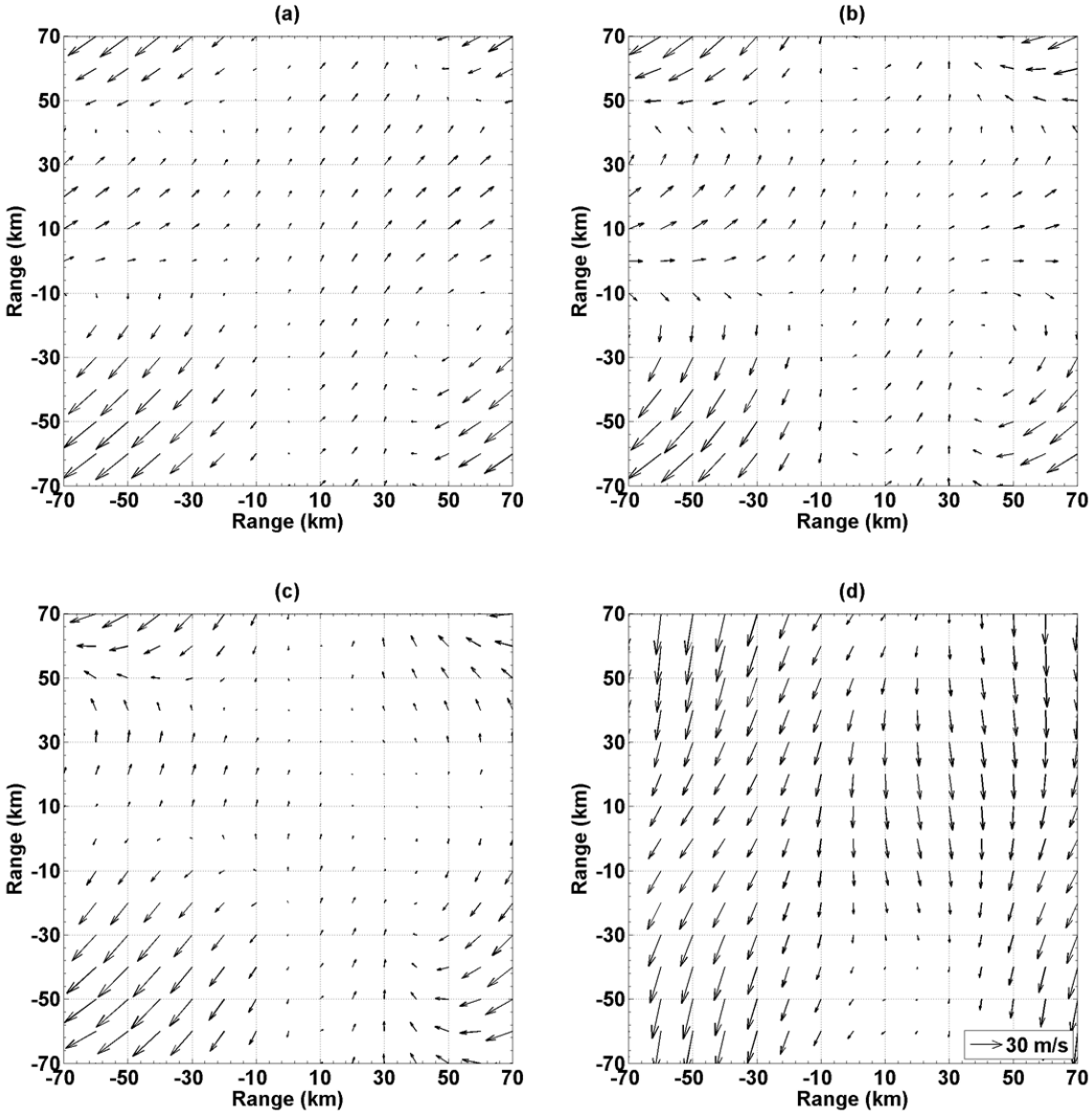

Figure 40. Example motion vector field estimates for the reflectivity fields depicted in Figure 37, for temporal resolutions of (a) 1 min, (b) 2 min, (c) 3 min, and (d) 8 min.

7.5 Results

The average CC and ETS scores corresponding to Eulerian and Lagrangian persistence nowcasting methods calculated over the 17-event 2009 CASA IP1 dataset are depicted in Figure 41. The results show that Lagrangian lifetimes are longer than Eulerian lifetimes, as expected. Continuous and categorical lifetimes are shown to be approximately 14 min and 15 min, respectively, in Eulerian space and approximately 21 min and 20 min, respectively, in Lagrangian space.

Results for each of the 17 events collected during the 2009 CASA IP1 experiment and associated continuous (L_{CC}) and categorical (L_{ETS}) lifetimes for Eulerian (EP) and Lagrangian (LP) persistence are given in Table 5. Here, average lifetime values correspond to the average of the lifetime values computed for each event (i.e., the average of the lifetime values vs the lifetime computed from the average CC and ETS scores). Lifetime values beyond 30 min were estimated by linear extrapolation of the score array to the longer lead times. The results show the average continuous and categorical lifetimes to be approximately 21.3 and 21.5 min, respectively, in Eulerian space and approximately 24.2 min and 24.0 min, respectively, in Lagrangian space. Again, average Lagrangian lifetime values were higher than those corresponding to Eulerian persistence.

The following subsections present results of studies that further investigated characteristics of the predictability of precipitation patterns depicted by CASA IP1 radar data.

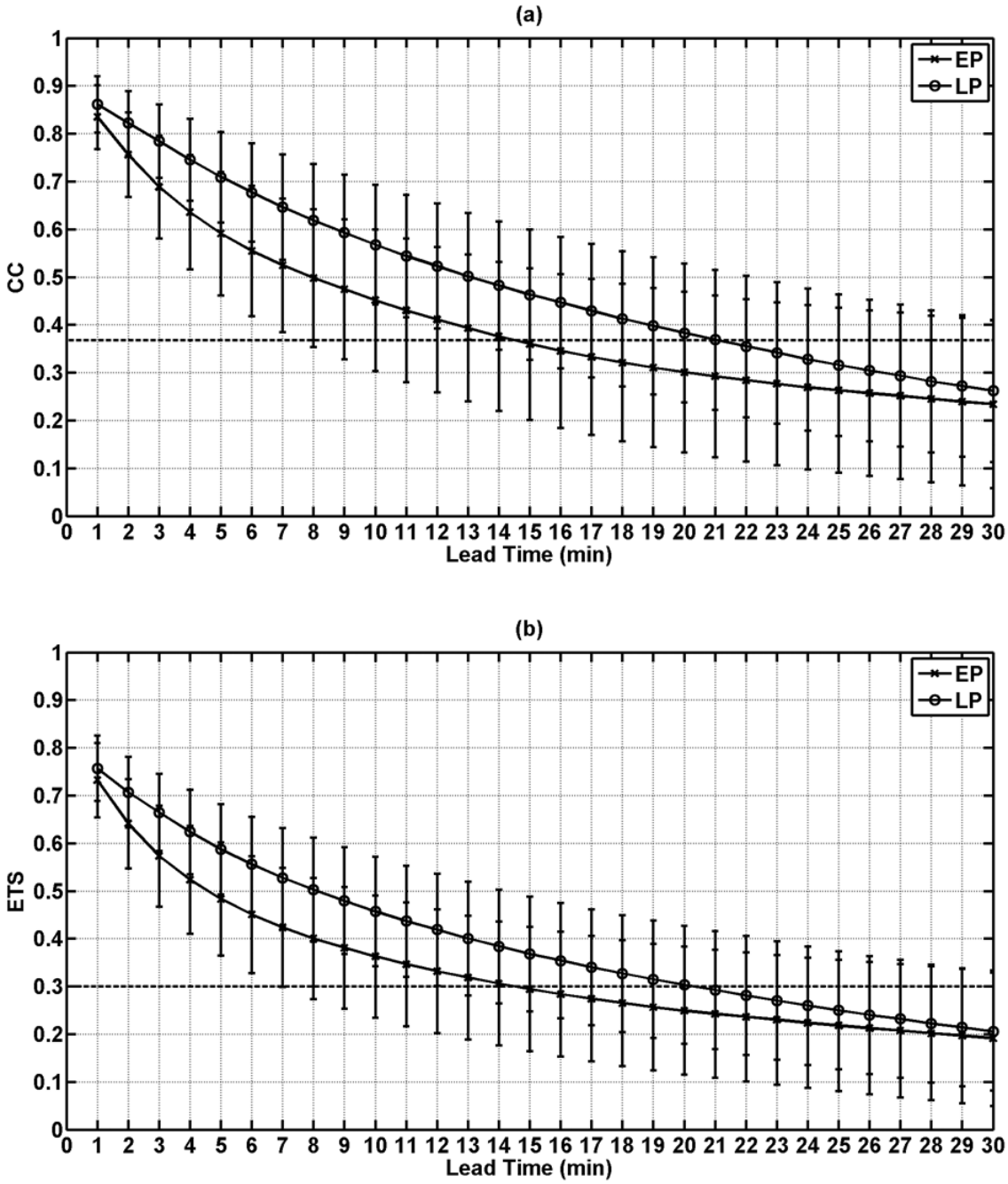

Figure 41. (a) Cross-correlation coefficient and (b) ETS vs prediction lead time estimated by Eulerian persistence (EP) and Lagrangian persistence (LP) nowcasting methods. Markers represent the mean value taken over the 17 events in the 2009 IP1 dataset and horizontal bars represent one standard deviation above and below the mean value. The dashed horizontal line in (a) represents the 1/*e* value where the corresponding lead time is taken to indicate the concept of "continuous lifetime". The dashed horizontal line in (b) represents the 0.3 value where the corresponding lead time is taken to indicate the concept of "categorical lifetime".

Table 5. Summary of precipitation event data collected during the CASA IP1 experiment used for nowcasting evaluation and lifetime estimates (L) based on cross-correlation (CC) and Equitable Threat Score (ETS) values in Eulerian (EP) and Lagrangian (LP) space.

Event No.	Start time (UTC)	Approximate duration (h)	Type	$L_{CC,EP}$ (min)	$L_{ETS,EP}$ (min)	$L_{CC,LP}$ (min)	$L_{ETS,LP}$ (min)
1	2111 10 Feb	5.8	Supercell	40.5	35.9	35.2	32.4
2	0014 10 Mar	4.8	Line	10.4	9.6	20.7	19.1
3	2307 23 Mar	6.0	Multicell	14.2	12.7	25.5	23.4
4	0025 31 Mar	2.0	Line	13.4	13.8	23.6	23.4
5	2236 16 Apr	3.0	Multicell	4.3	3.6	7.7	6.5
6	2347 18 Apr	1.0	Single-cell	10.4	10.4	15.4	15.7
7	2337 26 Apr	5.0	Line	14.6	14.5	21.2	20.7
8	0721 29 Apr	8.0	Multicell	15.0	34.7	20.4	21.8
9	0251 30 Apr	6.0	Multicell	40.3	36.5	29.0	29.0
10	0858 02 May	6.8	Multicell	14.3	12.4	17.0	15.3
11	1422 05 May	3.0	Multicell	12.3	13.4	17.4	17.6
12	0334 09 May	1.5	Single-cell	7.9	6.7	9.8	8.7
13	0907 11 May	1.8	Multicell	6.3	6.7	12.9	12.4
14	0930 12 May	2.5	Multicell	11.1	7.9	19.2	16.8
15	0319 13 May	3.3	Supercell	17.5	18.1	24.0	27.2
16	0430 14 May	2.5	Supercell	79.1	56.2	61.6	60.5
17	0234 16 May	3.0	Line	51.1	71.6	51.1	57.3
Avg	—	3.9	—	21.3	21.5	24.2	24.0

7.5.1 Dependence of predictability on precipitation pattern type

Results stratifying lifetimes according to event type are shown in Table 6. Due to the relatively small dataset, lifetime values for each event type were compared to lifetime values averaged over the set of remaining event types. Such stratification allows for preliminary conclusions about the dependence of predictability on precipitation event type to be drawn.

The results show line events to be more predictable in terms of continuous and categorical lifetime than the set of remaining types. This result can be attributed to the organized structure of line events yielding more predictability. Regarding nowcasting line events, using Lagrangian persistence was shown to provide relative improvements of about 30% and 10% in terms of continuous and categorical lifetimes, respectively, to facilitate predictability to about 30 min. This relative improvement relates directly to the high degree of advection contributing to the overall evolution of the event. The results presented in Table 6 also show multicell storms to be less predictable than the set of remaining types. This is expected as multicell events exhibited less structure and were thus less predictable. Regarding nowcasting multicell events, using Lagrangian persistence was shown to provide relative improvements of about 27% and 13%, respectively, to facilitate predictability of about 18 min. Despite the relatively unstructured nature of multicell events, Lagrangian persistence still provided considerable improvement over Eulerian persistence even though absolute predictability was shown to be only about 60% that of the line events.

Table 6. Comparison of average lifetime values, $\overline{L}$, vs precipitation event type (LN = line, MC = multicell, SC = single-cell, PC = supercell).

Event type set	Number of events	$\overline{L}_{CC,EP}$ (min)	$\overline{L}_{ETS,EP}$ (min)	$\overline{L}_{CC,LP}$ (min)	$\overline{L}_{ETS,LP}$ (min)
LN	4	22.38	27.38	29.15	30.13
MC ∪ SC ∪ PC	13	21.02	19.63	22.70	22.10
MC	8	14.73	15.99	18.64	17.85
LN ∪ SC ∪ PC	9	27.21	26.31	29.18	29.44
SC	2	9.15	8.55	12.60	12.20
LN ∪ MC ∪ PC	15	20.95	19.71	23.96	23.29
PC	3	45.70	36.73	40.27	40.03
LN ∪ MC ∪ SC	14	16.11	18.18	20.78	20.55

Single-cell events were shown to be the least predictable, with Lagrangian persistence providing 38% and 43% relative improvement over Eulerian persistence in terms of continuous and categorical lifetimes, respectively, but facilitated predictability of only about 12 min. This is expected in the absence of complex interaction among smaller scales within larger-scale precipitation volumes. Such interaction has been shown to be responsible for the mass organization in large-scale precipitation volumes, where small scale changes are strongly coupled at larger scales where the predictability extends over longer time scales (Grecu and Krajewski 2000). Supercell events were shown to be the most predictable, with Eulerian persistence lifetimes greater than Lagrangian persistence lifetimes in terms of continuous categorical predictability and Lagrangian persistence only providing a relative improvement over Eulerian persistence of about 9% in terms of categorical predictability. These results are consistent with those presented by Grecu and Krajewski (2000) and Zawadzki et al (1994) who found longer decorrelation times for stronger events. The supercell events observed were also exceptionally wide-spread and persistent.

7.5.2 Dependence of predictability on data resolution

The results presented in Figure 41 are extended to analyze the dependence of predictability on spatial and temporal scales. The dependence on spatial scale was investigated by comparing predicted data fields filtered to each resolution to the corresponding unfiltered observations. The results are illustrated in Figure 42, which shows Lagrangian lifetimes in both continuous and categorical senses increase with decreasing spatial resolution. Eulerian lifetimes show less increase with decreasing spatial resolution in continuous and categorical senses, respectively. These results are consistent with those of similar studies that considered larger scales that showed smaller spatial scale features are shorter-lived than larger-scale features (Bellon and Zawadzki 1994; Grecu and Krajewski 2000; Germann et al. 2006).

The dependence on temporal resolution is illustrated in Figure 43, which shows Lagrangian persistence lifetimes decrease to the approximate values corresponding to Eulerian persistence around a temporal resolution of 8 min and Eulerian lifetimes increase slightly with decreasing temporal resolution. This behavior can be attributed to the nature of the DARTS nowcasting method, requiring a sequence of past data to estimate motion, and the increased number of perfect forecasts made by the Eulerian persistence paradigm afforded by the temporal processing methodology.

7.5.3 Limits to nowcasting using the Lagrangian persistence paradigm

Aside from the accuracy of the estimated motion vector field, two sources of forecast uncertainty exist when considering Lagrangian persistence of precipitation patterns: growth and dissipation of precipitation and changes in the storm motion vector field during the lead time period.

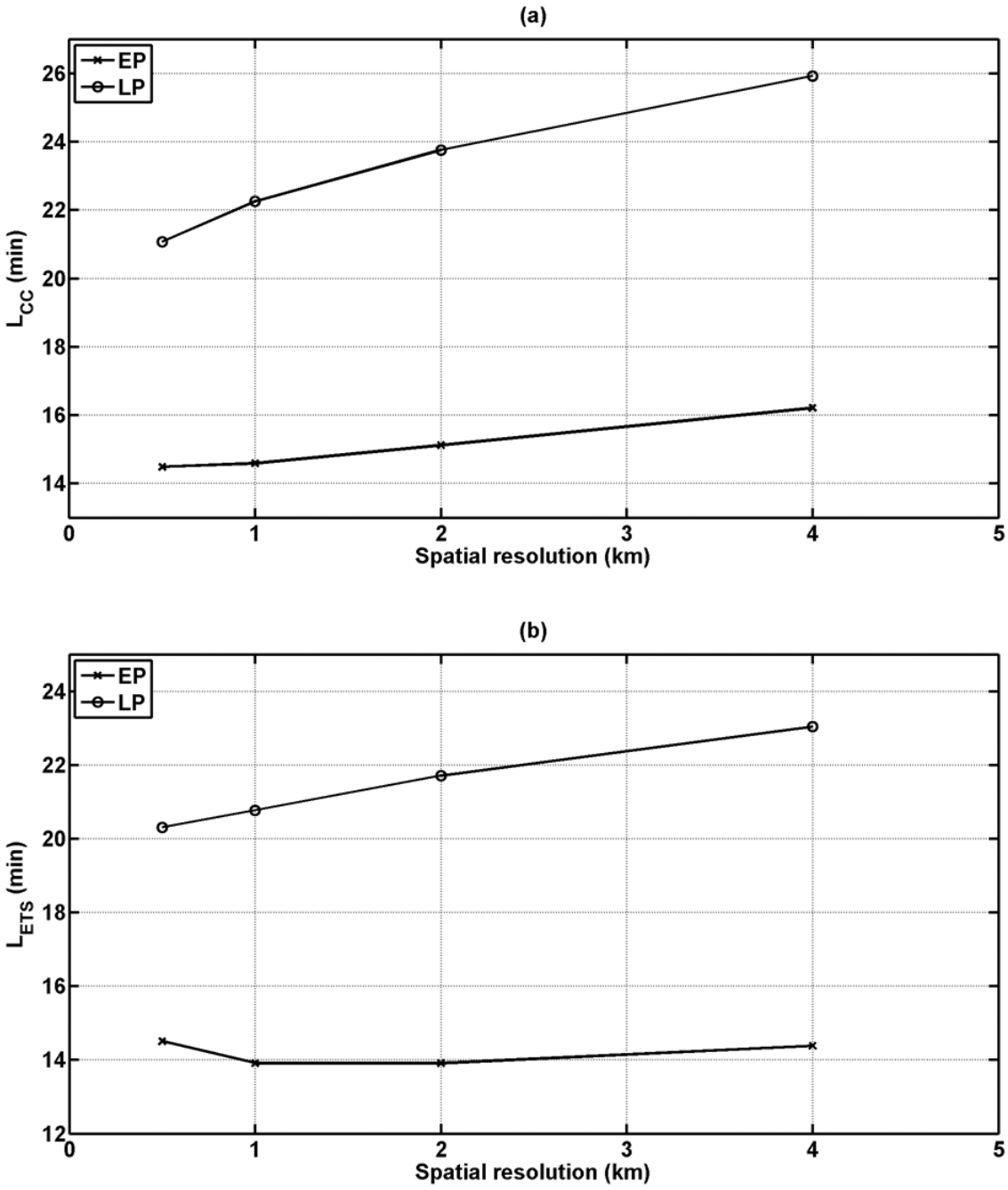

Figure 42. (a) Continuous and (b) categorical lifetime values vs spatial resolution. Markers represent the mean value taken over the 17 events in the 2009 IP1 dataset.

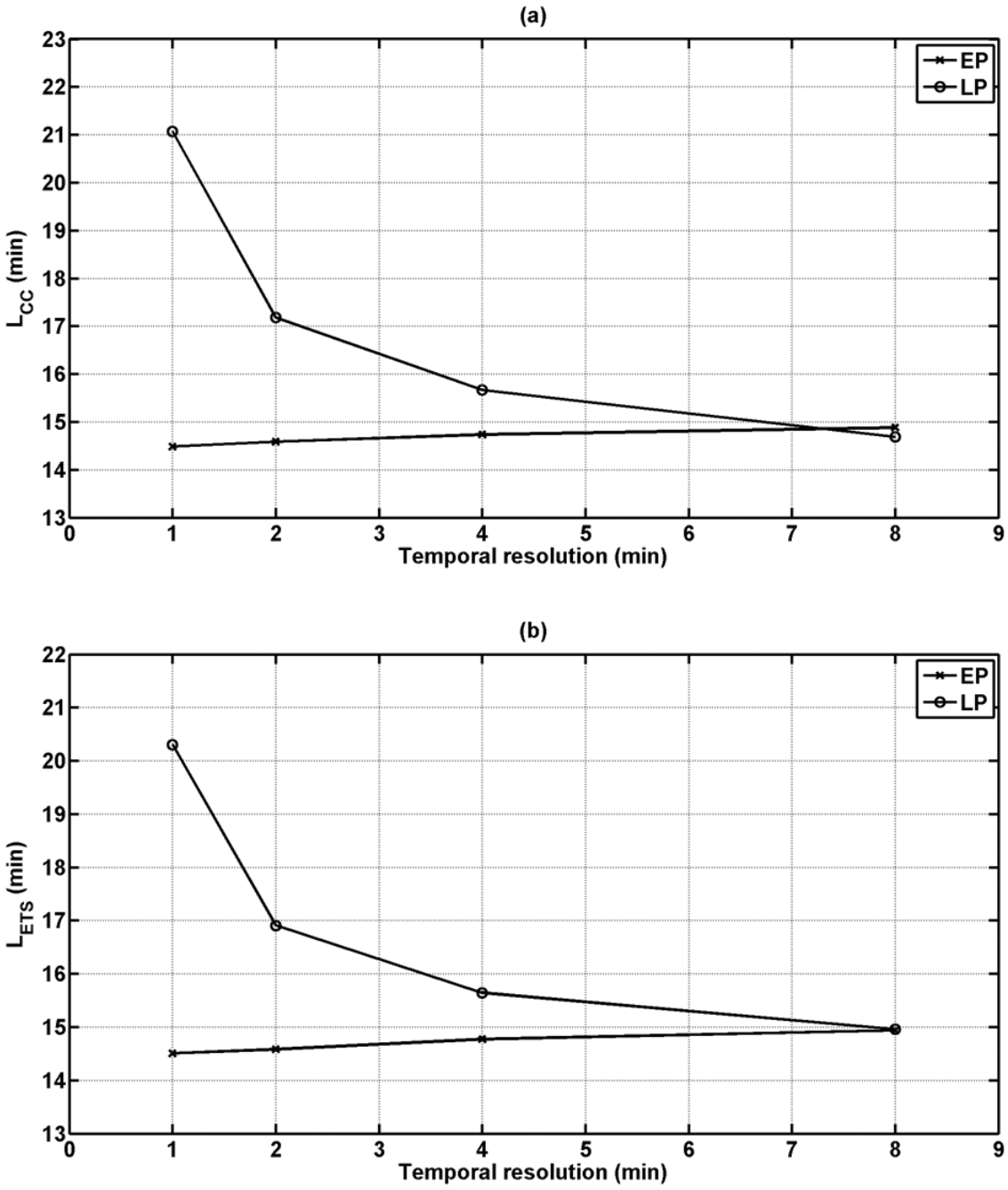

Figure 43. (a) Continuous and (b) categorical lifetime values vs temporal resolution. Markers represent the mean value taken over the 17 events in the 2009 IP1 dataset.

The relative importance of the changes in the storm motion vector field during the lead time period can be examined by advecting the observed and subsequently predicted reflectivity fields according to a time series of estimated motion vector fields computed from observations at each lead time instead of using a single, persistent motion vector field throughout the lead time. This process is illustrated in Figure 44.

The continuous and categorical lifetime values computed in this manner are presented in Figure 45. The results presented by Germann et al (2006) show an increase in continuous lifetime from 5.1 to 6.2 h (~22 % increase) when considering the paradigm used here. The results of this study show an increase in lifetime from about 21 to about 23.5 min (~12% increase) when considering a non-persistent (i.e., "Lagrangian updated" or "LU") motion vector field sequence vs a single motion vector field persistent up to the maximum lead time (Lagrangian persistence). Such behavior is expected as the assumption of Lagrangian persistence weakens with increasing lead time. While this methodology is practically unrealizable, such analysis provides an estimate of an upper-bound on nowcasting performance. These results suggest that most of the error in nowcasting using the DARTS and sinc kernel-based advection methodology and CASA IP1 radar data likely comes from evolution (i.e., growth and decay of intensity) of precipitation patterns occurring during the prediction period.

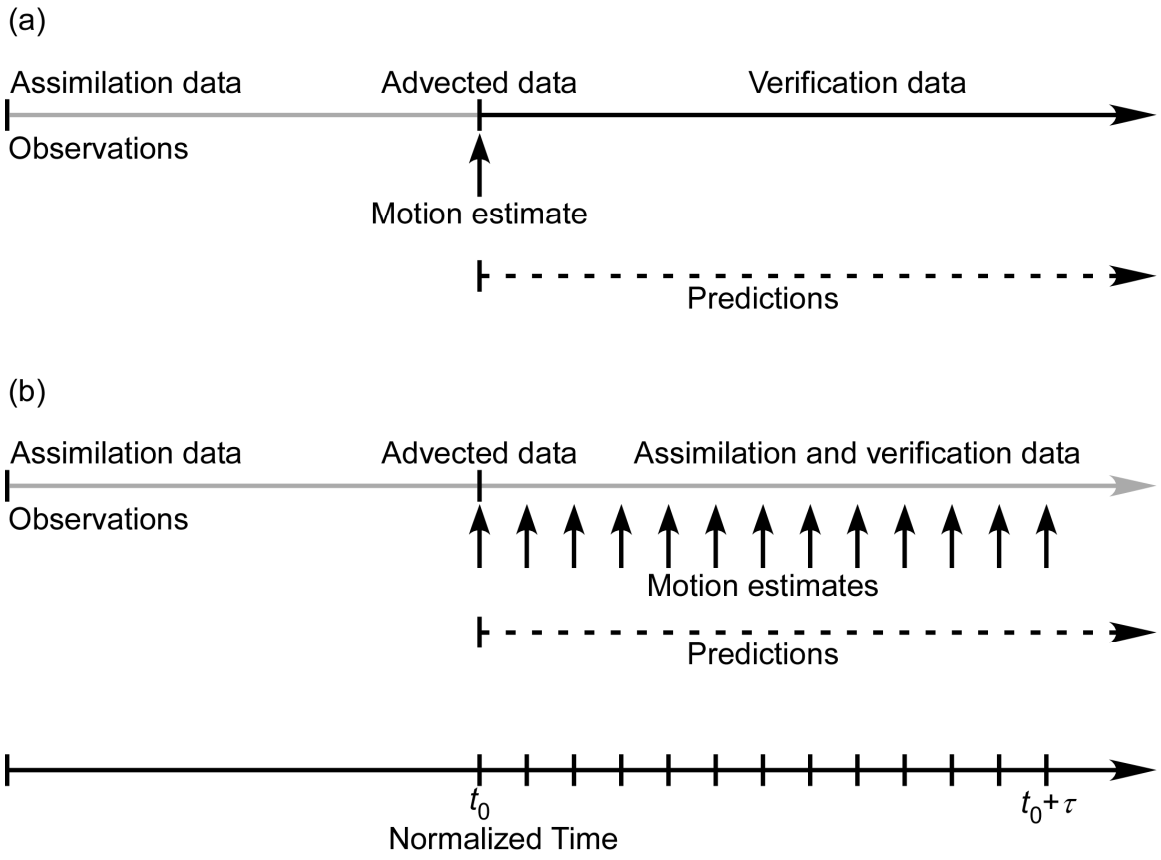

Figure 44. Illustration of the nowcasting procedure to estimate the useful extent of the Lagrangian persistence paradigm. While this procedure is practically unrealizable (i.e., future observations are used for motion estimation), it provides a practical upper-bound on nowcasting performance using the Lagrangian persistence model and CASA IP1 reflectivity data.

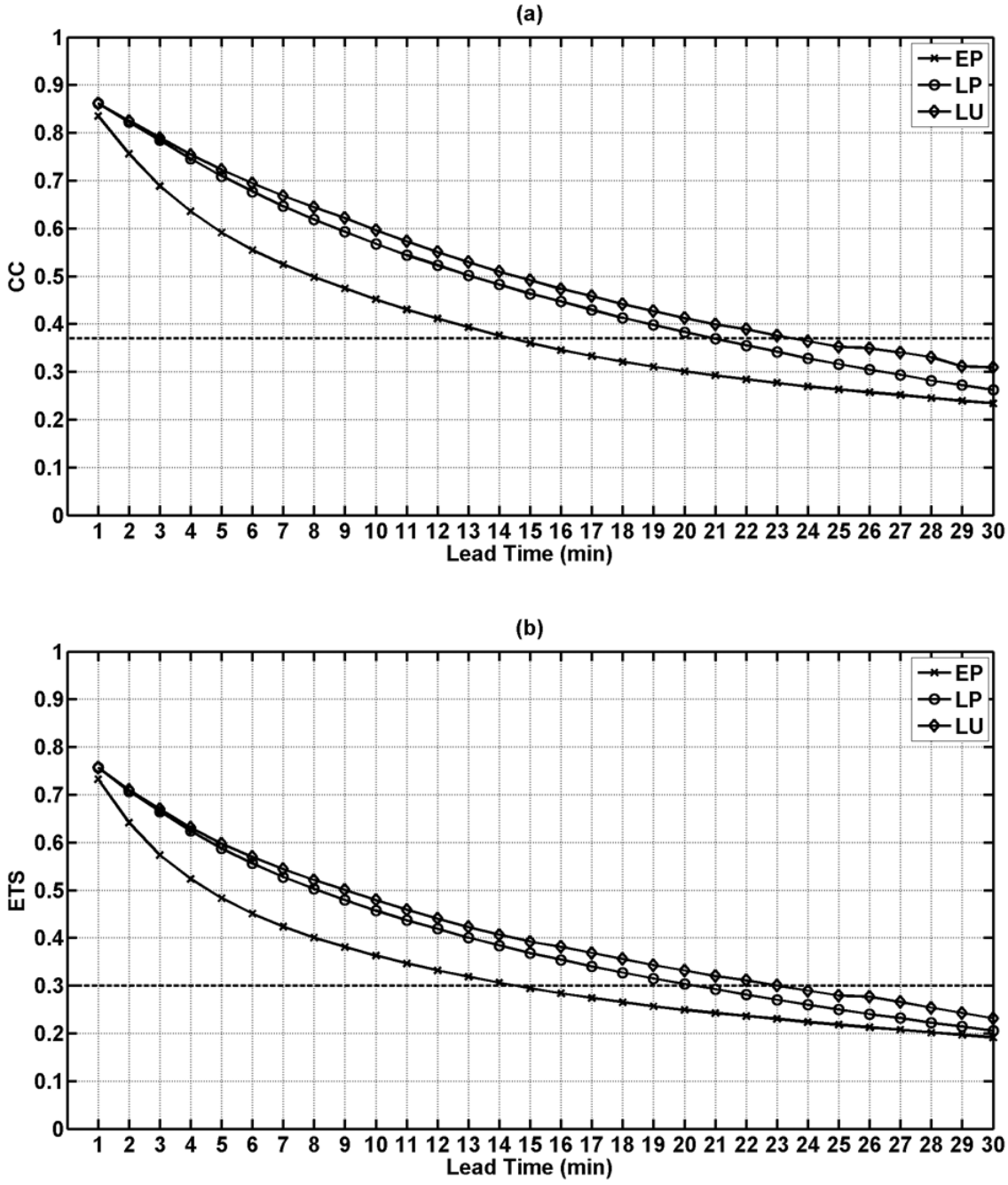

Figure 45. (a) Cross-correlation coefficient and (b) ETS vs lead time for Eulerian persistence (EP), Lagrangian persistence (LP), and nowcasting using a time series of motion vector fields throughout the lead time period (LU).

7.5.4 Connection to predictability at larger scales

The results of predictability presented in this study for microalpha (0.2–2 km) to mesobeta (20–200 km) scales using CASA IP1 radar observations, denoted "R10", is compared to results presented by Grecu and Krajewski (2000), denoted "GK00", that considered data at mesogamma (2–20 km) to meso (200–2000 km) scales, and Germann et al. (2006), denoted "GZT06", that considered data at mesogamma to macrobeta (2000–10 000 km) scales. Figure 46 illustrates the relationship between continuous lifetimes found in this study in Eulerian and Lagrangian space to those presented in GK00 and GZT06. These results suggest a linear relationship between predictability at microalpha to macrobeta scales and are consistent with those presented by the National Research Council (2009), which showed an approximate linear relationship between spatial and temporal scales of several types of meteorological phenomena across these scales.

7.6 Summary and conclusions

The predictability of precipitation patterns observed by weather radar is an important concept as it establishes a means to characterize precipitation patterns and provides an upper limit on the extent of useful forecasting. Predictability varies based on spatial and temporal scales of observed meteorological phenomena. This section presented a study that extended previous work by Grecu and Krajewski (2000) and Germann et al. (2006) by investigating the predictability of precipitation from microalpha (0.2–2 km) to mesobeta (20–200 km) scales using CASA IP1 composite radar reflectivity data and an experimental approach to quantify predictability.

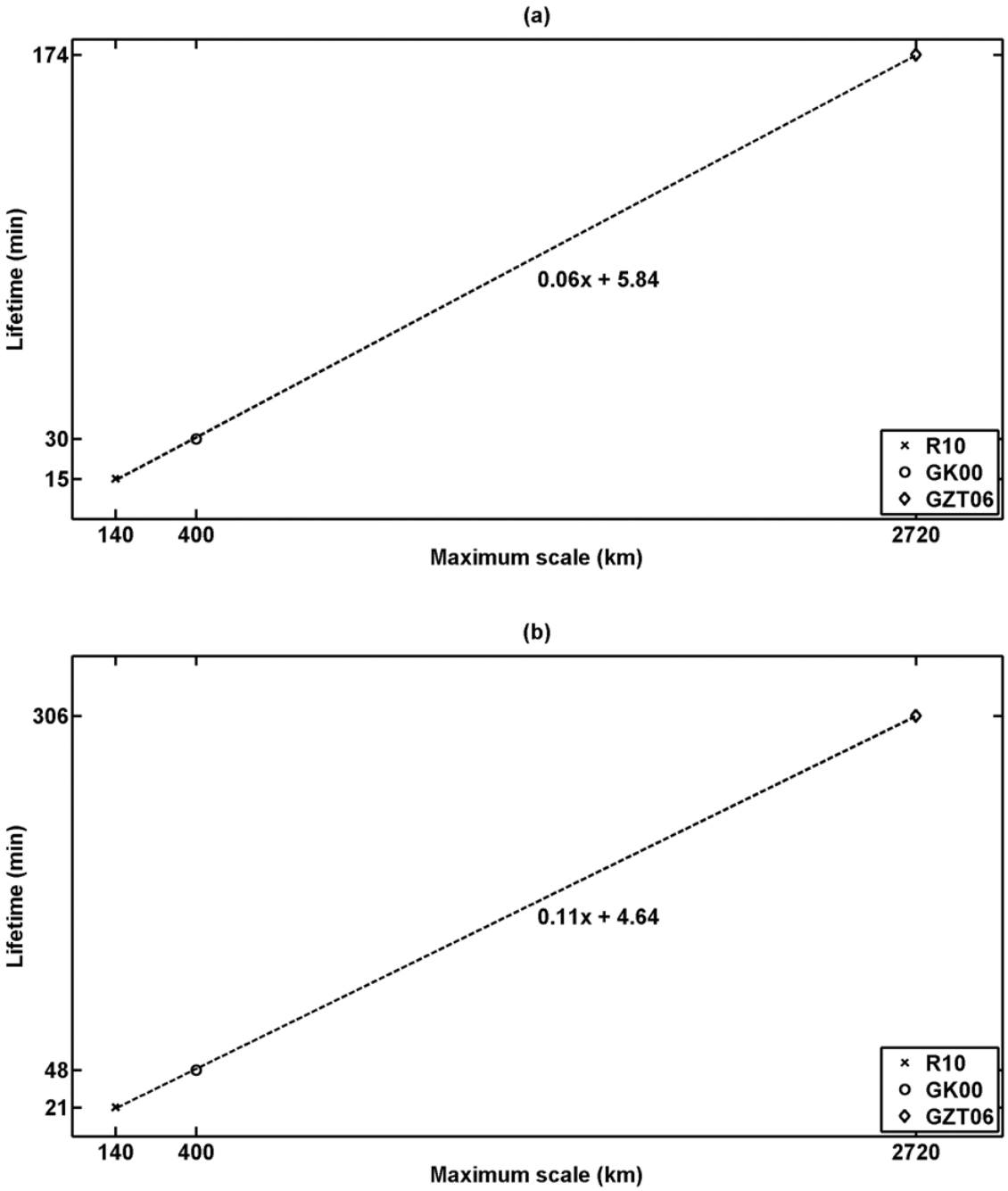

Figure 46. Relationship between continuous lifetime values in (a) Eulerian and (b) Lagrangian space vs maximum spatial scale estimated using the results of this research (R10) and those presented by Grecu and Krajewski (2000; GK00) and Germann et al. (2006; GZT06). The root mean square error of the linear regression fits are 0.44 and 0.74 min, respectively.

Lifetimes estimated from predictions based on Eulerian and Lagrangian persistence were computed and compared. Continuous lifetime values corresponding to the lead time when the cross-correlation coefficient between observations and predictions drops to 1/*e* were computed. Since nowcasting performance is typically assessed in a categorical (i.e., "hit" or "miss") sense, categorical lifetime values corresponding to the lead time when the ETS drops to 0.3 (corresponding approximately to FAR and POD scores both being equal to 0.5) were also computed. The DARTS and sinc kernel-based advection methodology was used to represent Lagrangian persistence. DARTS estimates motion at the same resolution as the data and the sinc kernel-based advection method was shown to adequately preserve the small-scale spatial features in the predicted reflectivity fields (Figure 36). Such an approach provides a relatively simple and practical means to assess predictability.

The results showed Lagrangian persistence lifetime values computed from CC and ETS scores averaged over approximately 66 h of data collected by the CASA IP1 radar network during the winter and spring of 2009 were about 20 min in both continuous and categorical senses, representing improvements of about 30% and 40% (~6 min) over Eulerian persistence, respectively. These results suggest that operational nowcasting using the DARTS and sinc kernel-based nowcasting methodology should be considered to be generally useful up to about 20 min.

A preliminary study was performed to give insight into the dependence of predictability on precipitation event type. The results showed that supercell events (exhibiting a high degree of persistence, rotation, and low advection velocities) were most predictable in terms of lifetime values, followed by line events (exhibiting

organized and persistent structure) and multicell events (where complex interaction between individual cells likely enhances predictability). Single-cell events were shown to be the least predictable using data from this limited dataset.

The analysis of predictability was extended to investigate the spatial and temporal dependence on space-time scales represented by data resolution on nowcasting performance. Results showed that continuous and categorical lifetime values corresponding to Lagrangian persistence increased with decreasing spatial resolution and were higher than those corresponding to Eulerian persistence. These results support the notion that lifetimes of larger-scale features are longer than those for smaller-scale features and that selective filtering should be used to improve nowcasting performance. The results of the study investigating the dependence on temporal resolution showed that Lagrangian lifetime values decreased to values approximately corresponding to Eulerian persistence as temporal resolution was reduced to about 8 min by substituting previous observations into the sequence of reflectivity observations accordingly. This can be attributed to the nature of the DARTS motion estimation method and the increased number of perfect forecasts made by Eulerian persistence afforded by the data processing methodology.

Results of a study to assess the contribution of changes in the estimated motion vector field during the nowcast lead time to the nowcast error showed that nowcasting using a motion vector field updated at each lead time provided an increase in lifetimes of about 10–12% (~2–3 min). Although such a nowcasting paradigm is not realizable in practice, these results establish an approximate upper-bound on nowcasting performance using the

DARTS and sinc kernel-based advection nowcasting methodology and CASA IP1 radar data.

Finally, estimates of predictability in this study were compared to those presented in literature for larger [mesogamma (2–20 km) to macrobeta (2000–10 000 km)] scales. The results suggest a linear relationship between predictability across these scales, with RMSE error for a linear regression being less than 1 min. The fact that the regression analysis of results from three separate studies conducted by three different researchers using different prediction methodologies and radar data collected over different regions yielded such a small error makes a strong statement regarding a fundamental linear space-time relationship between the atmospheric scales considered in this study.

CHAPTER VIII. NOWCASTING RAINFALL FIELDS DERIVED FROM SPECIFIC DIFFERENTIAL PHASE ESTMATES

8.1 Introduction

While nowcasting of precipitation has traditionally been done using radar reflectivity data, research over the last decade indicates that using the specific differential phase (K_{dp}), defined as one-half the range derivative of the two-way differential phase (Φ_{dp}), has several advantages over using reflectivity for estimating rainfall accumulation. Since Φ_{dp} is a dual-polarized radar product and not a power measurement, rainfall estimates derived from K_{dp} are not susceptible to radar calibration error, attenuation, or beam blockage and are less affected by anomalous propagation. Rainfall rate estimates derived from K_{dp} are also less sensitive to variations in drop size distributions and to the presence of dry, tumbling hail than those derived from reflectivity. The specific differential phase can also be used to correct for attenuation losses and to verify radar hardware calibration (Brandes et al. 2001).

Additionally, X-band (λ ~ 3 cm) polarimetry used in the CASA network offers important practical advantages over longer wavelength radar polarimetry at shorter ranges. One advantage is a significantly stronger differential phase shift on propagation, which is proportional to the radar frequency [for Rayleigh scattering (Bringi and Chandrasekar 2001)]. This allows the use of K_{dp} -based rainfall estimators for lighter rainfall rates when measured with X-band radars vs measurements made by longer wavelength radars. X-band radars are also smaller, less expensive, require less energy for

the same sensitivity, and are more easily transported compared to their longer-wavelength counterparts. These traits make X-band radars a convenient tool for quantitative precipitation estimation (QPE) where high-resolution rainfall measurements are needed in a limited area such as a relatively small watershed or for specialized studies like those in urban hydrology (Maki et al. 2008).

A new algorithm for estimating K_{dp} has been developed that has been shown to yield more accurate and robust estimates than previous methods (Wang and Chandrasekar 2009). Studies investigating the feasibility of nowcasting rainfall fields derived from K_{dp} fields estimated using this new algorithm have yet to be performed. This section presents a preliminary investigation of the characteristics and extent of nowcasting rainfall derived from K_{dp} fields estimated using the method presented by Wang and Chandrasekar (2009). Nowcasting performance was assessed by scoring predicted rain rate fields relative to original rain rate field estimates and rain gauge measurements. Approximately 9 h of data from two events in the 2009 CASA IP1 dataset was considered for evaluation.

8.2 K_{dp} background and estimation

In dual-linear-polarization bases, the specific differential phase K_{dp}, defined as the slope of range profiles of the differential propagation phase shift Φ_{dp} between horizontal (H) and vertical (V) polarization states (Seliga and Bringi 1978; Jameson 1985; Bringi and Chandrasekar 2001), is fundamentally represented as

$$K_{dp}(r) = \frac{1}{2}\frac{d\Phi_{dp}(r)}{dr}. \tag{8.1}$$

Since falling raindrops are oblate, the electric field will encounter more water content in the horizontal direction than in the vertical. The H-pulse will therefore be affected by

more water than the V-pulse. Since electromagnetic waves travel more slowly through water than through air, the horizontally polarized wave will travel more slowly through the field of raindrops than will the vertically polarized pulse. Likewise, the horizontally polarized backscattered radiation will also travel more slowly back to the radar than the vertically-polarized backscatter (Bringi and Chandrasekar 2001).

Radar does not measure the forward propagation parameter Φ_{dp} directly. Instead, the total differential phase Ψ_{dp} is estimated from copolar covariance that consists of both the phase shifts resulting from forward propagation and backscattering, shown as

$$\Psi_{dp} = \Phi_{dp}(r) + \delta_{hv}(r). \tag{8.2}$$

If the differential backscattering phase δ_{hv} is relatively constant or negligible, the profile of Ψ_{dp} can be used to estimate K_{dp}. This is not always the case, however, and significant gate-to-gate variation of δ_{hv} must be suppressed by filtering and the presence of significant δ_{hv} over a short range must be detected and removed (Chandrasekar et al. 1990).

The estimation of K_{dp} involves approximating the slope of Φ_{dp} profiles, which is known to be a noisy and unstable computation. Evaluation of the derivative is essentially a high-pass filtering process expecting a smooth and continuous input function (Mitra 2005). The range profile of total differential phase Ψ_{dp} contains Φ_{dp} and differential backscatter phase shift δ_{hv}, as well as measurement fluctuations. The fluctuation in the estimates of Ψ_{dp} will be magnified during the differentiation resulting in large variance in the estimates of K_{dp}. Furthermore, phase wrapping may exist in Φ_{dp} requiring proper unfolding of the wrapped phase profiles. For a long propagation path in rain or at higher-

frequency bands such as X-band, Φ_{dp} values can easily exceed the maximum unambiguous range.

Previous methods for estimating K_{dp} involved piecewise fitting to predict the local trend, where any phase sample deviating too far from this trend was attributed to phase wrapping. This solution is neither elegant nor stable because of the statistical fluctuations present in the Φ_{dp} field. Previous approaches have also been sought to reduce the variance of K_{dp} estimates, which included range filtering, linear fitting, or both (Golestani et al. 1989; Hubbert and Bringi 1995). These techniques reduce the peak K_{dp} values in the estimation that could introduce biases. In addition, only limited adaptive capability can be achieved with filtering or fitting to follow the steep slopes within intense rain cells and reduce the estimation variance in the rest of the segments simultaneously.

In CSU–CHILL (Brunkow et al. 2000), logic is adopted to detect the wrapped phase and accordingly unfold the range profile of Φ_{dp}. Low-pass range filtering is used to reduce the estimation variance, where variance reduction is approximately proportional to the normalized cutoff frequency of the filter. Hubbert et al. (1993) presented a range filter that suppresses gate-to-gate fluctuations but preserves the underlying trend of Φ_{dp}. In the CSU–CHILL algorithm, the cutoff scale is chosen to be 3 km and iterative filtering is used to adaptively compensate for the persistence of large δ_{hv}. This adaptive adjustment is meant to follow the steep phase changes in intensive precipitation regions while keeping the variation of estimated K_{dp} low in light precipitation regions. The regression length is tailored for the CSU–CHILL radar, which has a range resolution of 150 m. Therefore, the estimation can keep up with a small-scale variability up to 1.5 km in heavy rain and a large-scale variability up to 4.5 km in light rain.

In general, the conventional approach used to estimate K_{dp} is somewhat complicated in the sense that a slope is first approximated for unfolding the phase profiles and then a more accurate slope is estimated for K_{dp}. Its performance also relies on the choice of several hard thresholds.

Wang and Chandrasekar (2009) presented an adaptive scheme to estimate K_{dp} that avoids the need to unfold phases, which they showed to have better range resolution in intense rain cells to capture the small-scale variability vs previous approaches. The new estimator is based on the complex-valued range profiles of the differential phase shift. When the profile crosses a full period, even though the principal phase wraps back with an abrupt jump, locally the profile is still continuous in the complex domain. In general form, the K_{dp} estimate is given by

$$\hat{K}_{dp} = -j\left\{\frac{\vartheta'(r)}{\vartheta(r)}\right\} + e(r), \tag{8.3}$$

where,

$$\vartheta(r) = e^{j\hat{\Psi}_{dp}(r)} \text{ and} \tag{8.4}$$

$$\vartheta'(r) = je^{j\hat{\Psi}_{dp}(r)}\frac{d\hat{\Psi}_{dp}(r)}{dr}. \tag{8.5}$$

K_{dp} estimates are made by filtering angular Φ_{dp} profiles based on angular Ψ_{dp} statistics and estimating K_{dp} using cubic spline interpolation (Gerald and Wheatley 2003). Thus, phase unfolding is avoided, and the accuracy is also ensured.

A regularization technique was introduced to control the balance between estimation bias and variance and incorporates adaptive capability to keep up with steep change of Φ_{dp}. The conventional filtering process is avoided by employing a regularization

framework, and stable numerical derivatives can be computed with an appropriate choice of Lagrangian parameter, λ, in the following manner

$$\min_{s(r)}\left\{\int\left|s'(r)\right|^2 dr+\lambda\sum_{k=1}^{M}\left|f(r_k)-\int_{-\infty}^{r_k}s(r)dr\right|^2\right\}, \tag{8.6}$$

where $f(r_k)$ is the range profile of Φ_{dp} and $s(r)$ is the function to be found to minimize both the smoothness of the underlying regression function and the regression errors. Using cubic splines as the regression function, the polynomial function for the kth interval between nodes r_k and r_{k+1} can be written as

$$g_k(r)=a_k(r-r_k)^3+b_k(r-r_k)^2+c_k(r-r_k)+d_k,\quad r\in\left[r_k,r_{k+1}\right] \tag{8.7}$$

and the resulting K_{dp} estimate is given as

$$\hat{K}_{dp}=\frac{1}{2}\mathrm{Im}\left(\frac{c_k}{d_k}\right). \tag{8.8}$$

Adaptivity to avoid oversmoothing segments of low variations and peak K_{dp} values is achieved by introducing varying weights, q and w, in (8.6) in the following manner

$$\min_{s(r)}\left\{\int q^2(r)\left|s'(r)\right|^2 dr+\lambda\sum_{k=1}^{M}w^2(r_k)\left|f(r_k)-\int_{-\infty}^{r_k}s(r)dr\right|^2\right\} \tag{8.9}$$

that allows for the control of the balance between bias (to compensate for the variation in slope) and variance (to compensate for the statistical fluctuation of the input profiles) for different segments. Wang and Chandrasekar (2009) presented a method by which these parameters can be updated adaptively and provide robust operational estimation of K_{dp} relative to previous methods.

Wang and Chandrasekar (2009) showed the new technique matched the structure of a single storm event observed by the CASA network much better than previous approaches

and that negative K_{dp} values were largely eliminated. This method for K_{dp} estimation will be used in this research.

8.3 Estimating rainfall from K_{dp}

Bringi and Chandrasekar (2001) showed that K_{dp} in rain is proportional to the product of rainwater content and the mass-weighted mean diameter. This also indicates that K_{dp} is related to the fourth moment of the drop size distribution (DSD). Subsequently it was shown that a power-law expression relating any moment of the DSD and rainfall rate can be derived after normalizing by the intercept parameter of a normalized gamma drop size distribution. Therefore, a general K_{dp}-based estimate of rainfall rate can be expressed as (Sachidananda and Zrnić 1986; Chandrasekar et al. 1988)

$$R = aK_{dp}^{b}, \tag{8.10}$$

where R is the rainfall rate in mm h^{-1} and K_{dp} is in units of ^{o} km^{-1}. Even though the R-K_{dp} relationship is relatively insensitive to variation of DSD, subtle difference exists for different DSDs and especially for different raindrop shapes. The mean rain drop shape vs size has been studied extensively in the literature (Chandrasekar et al. 1988, Bringi et al.1998, Brandes et al. 2002, Thurai and Bringi 2005). A range of coefficients has been reported for the R-K_{dp} power law relation at both S-band and X-band (Gorgucci et al. 2001; Matrosov et al. 2002; Park et al. 2005; Ryzhkov et al. 2005). The R-K_{dp} relationship used in this study is similar to that used in the KOUN dual-polarized radar by Ryzhkov (2005) and scaled to X-band operation at 9.4 GHz, shown as

$$R = 18.15K_{dp}^{0.791}. \tag{8.11}$$

8.4 Data

Approximately 9 h of data collected during the 05 May (multicell) and 14 May (supercell) CASA IP1 events were used for evaluation. Estimates of K_{dp} fields using the method described by Wang and Chandrasekar (2009) were generated from full 2^{o} surveillance sweep scans and converted to gridded and merged Plan Position Indicator (PPI) fields using the technique described by Liu et al. (2007). A threshold of 5 mm h^{-1} was applied.

Rain gauge cross-validation was performed using data collected by gauges located within the Little Washita River Experimental Watershed (LWREW), which is managed by the U. S. Department of Agriculture (USDA) Agricultural Research Service (ARS) as part of the Little Washita Micronetwork (Allen and Naney 1991). The LWREW covers an area of 611 km^2 and is situated in the center of the CASA IP1 test bed allowing for overlapping coverage from almost all the CASA IP1 radars (Figure 47). Data from 20 unheated tipping-bucket rain gauges deployed within the watershed were considered, which measure rainfall in discrete bucket tips of 0.254 mm per tip. The gauge data were archived as running rainfall accumulation in 5-min intervals over a 24-h period. Piecewise Cubic Hermite Interpolating Polynomial derivation was used to temporally align the radar and gauge data and estimate rainfall rate from measured accumulation (Fritsch and Carlson 1980).

8.5 Assessment methodology

The cross-correlation coefficient [CC; Eq (7.1)], ETS [Eq (7.2)], and MAE [Eq (4.4)] were used to assess nowcasting performance relative to the initial rainfall intensity estimate from which future predictions were generated.

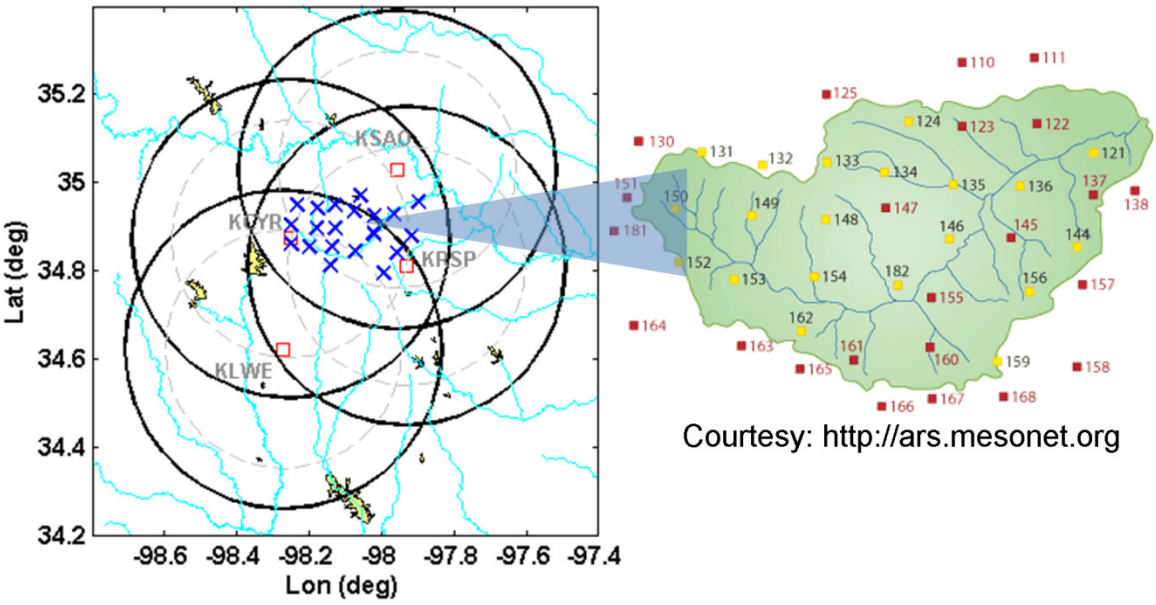

Figure 47. The distribution of ARS Micronet gauge network within the IP1 network coverage area. A current operational gauge station is denoted by an 'x' on the left and labeled with station IDs on the right [from Wang and Chandrasekar (2010)].

A scoring box size of 1 km × 1 km and a threshold of 5 mm h^{-1} were used for the calculation of the ETS scores in this study.

Additionally, Normalized Bias (NB), Normalized Standard Error (NSE), and the CC were used to assess nowcasting performance relative to rain gauge measurements. The NB and NSE are defined respectively as follows

$$\mathrm{NB} \equiv \frac{\langle R_\mathrm{R} - R_\mathrm{G} \rangle}{\langle R_\mathrm{G} \rangle} \text{ and} \tag{8.12}$$

$$\mathrm{NSE} \equiv \frac{\langle |R_\mathrm{R} - R_\mathrm{G}| \rangle}{\langle R_\mathrm{G} \rangle}, \tag{8.13}$$

where the brackets indicate the sample (spatial) average, R_R is the radar estimate and R_G is the gauge measurement of instantaneous rainfall rate. The CC is defined in Eq (7.1), but in this case is computed between radar measurements chosen at the location of rain

gauges and the rain gauge measurements temporally interpolated to the time of the estimated or predicted rain rate fields.

8.6 Results

Example rain rate fields estimated using Eq (8.11) and corresponding 5-min predicted rain rate fields from the 05 May and 14 May data are shown in Figure 48. The average CC, ETS, and MAE scores computed relative to the initial rain rate field estimates are shown in Figure 49. The results show continuous lifetimes to be about 20 and 11 min and categorical lifetimes to be about 18 and 14 min for Lagrangian and Eulerian persistence, respectively. MAE values are shown to be about 0.50 mm h^{-1} lower for Lagrangian persistence vs Eulerian persistence for a 20-min lead time. These results are consistent with those shown in Figure 41.

The average NB, NSE, and CC scores computed relative to rain gauge observations are shown in Figure 50 to Figure 52. To compensate for the potential time delay between K_{dp} estimates aloft and rain gauge measurements at the surface, nowcasts were verified using 0-, 1-, and 2-min time lags of rain gauge data relative to radar estimates. The prediction lead times are referenced to the times of the radar estimates (i.e., an n-min nowcast corresponding to a 0-min lag aligns with an $n - m$ nowcast corresponding to an m-min lag).

The 0-min lag results show NB corresponding to nowcasts made by the DARTS and the sinc kernel-based methodology begins to increase relative to NB values corresponding to Eulerian persistence after a lead time of about 5 min.

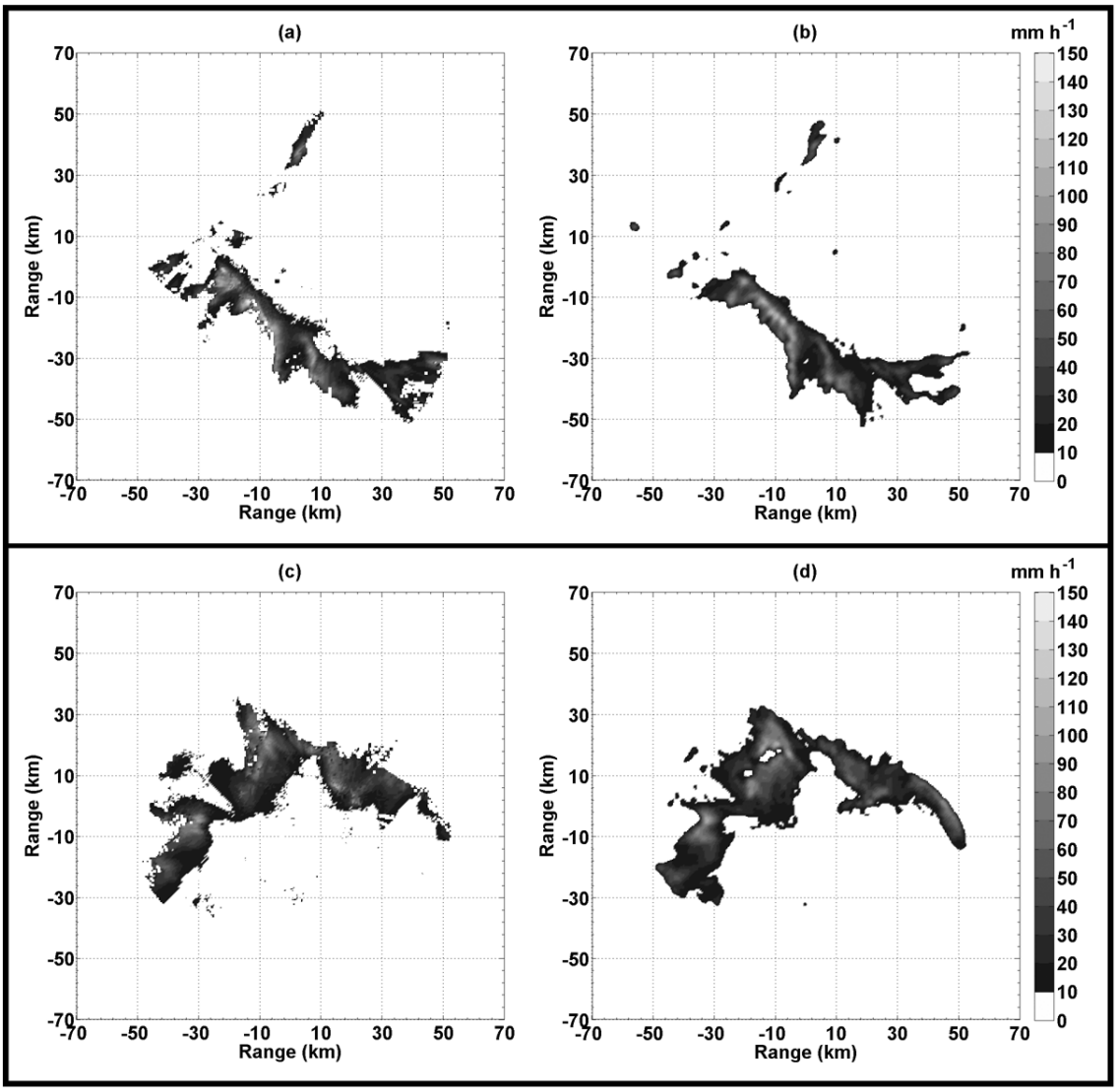

Figure 48. Example (a) estimated rain rate field and (b) 5-min predicted rain rate field corresponding to time 1517 UTC 05 May 2009 and (c) estimated rain rate field and (d) 5-min predicted rain rate field corresponding to time 0414 UTC 14 May 2009.

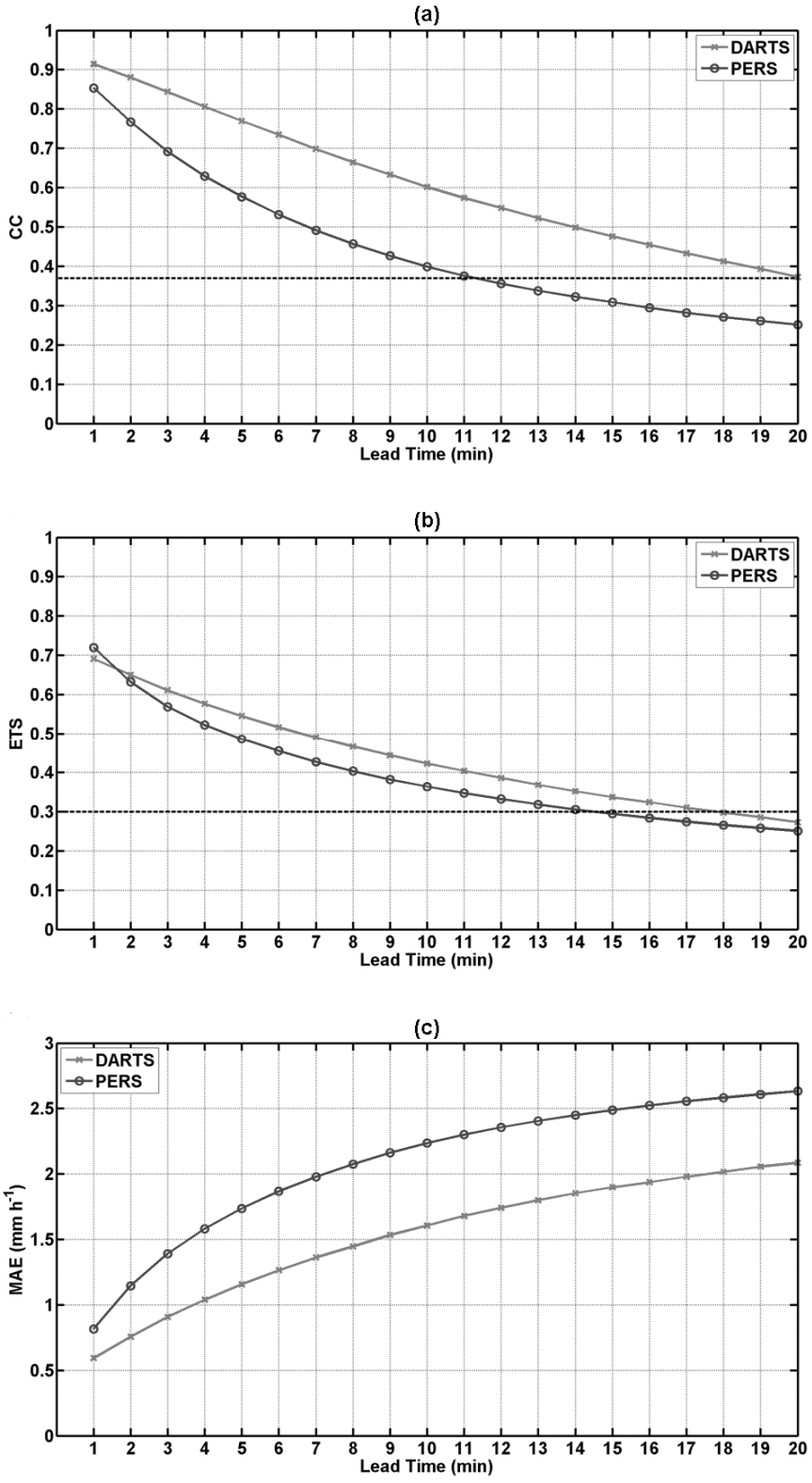

Figure 49. (a) CC, (b) ETS, and (c) MAE scores averaged over the 05 May and 14 May 2009 CASA IP1 events illustrating the performance of nowcasting rain rate fields estimated from K_{dp} relative to initial field estimates.

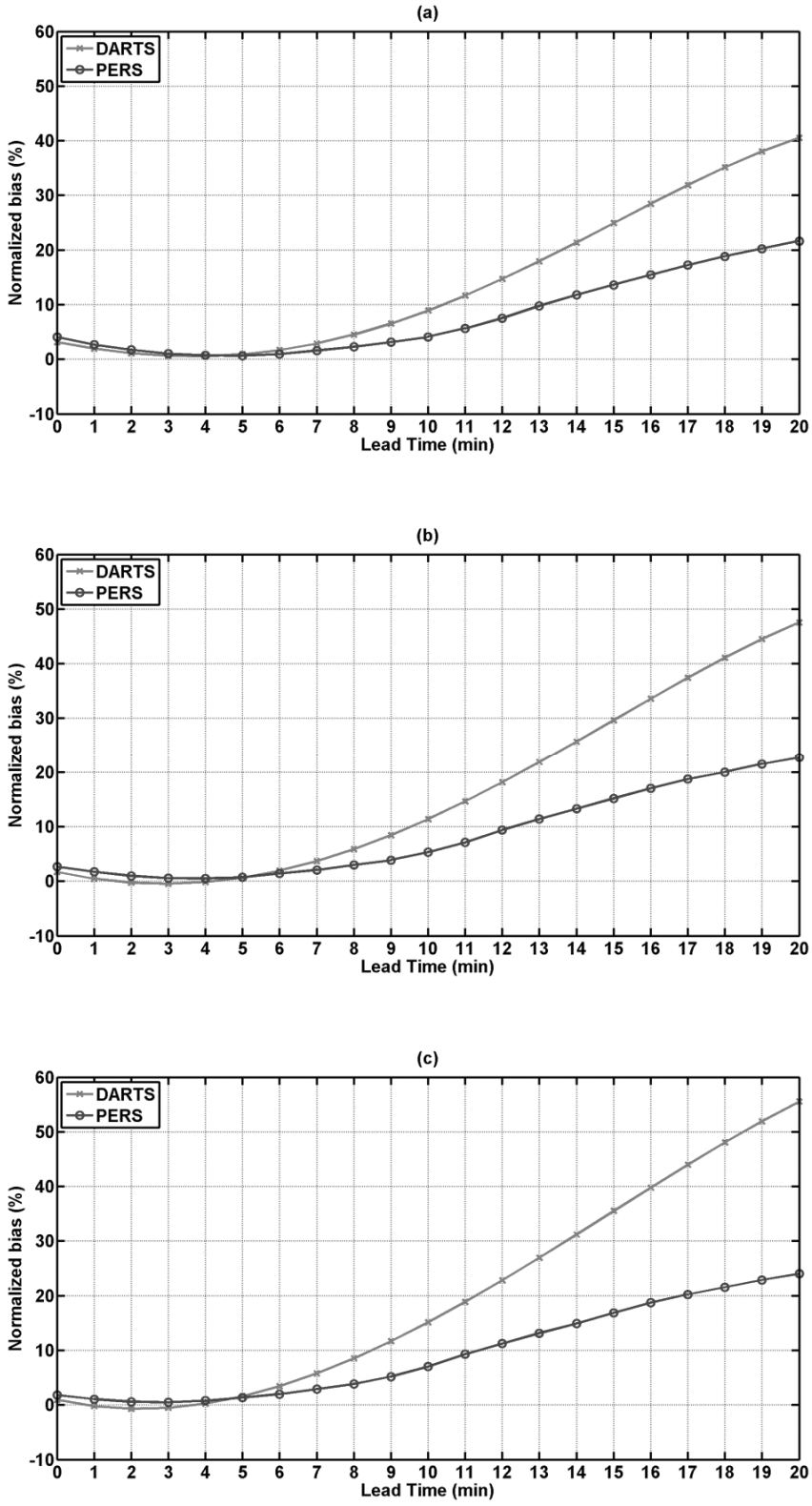

Figure 50. Normalized bias scores averaged over the 05 May and 14 May 2009 CASA IP1 events illustrating the performance of nowcasting rain rate fields estimated from K_{dp} relative to rain gauge measurements for time lags of (a) 0, (b) 1, and (c) 2 min.

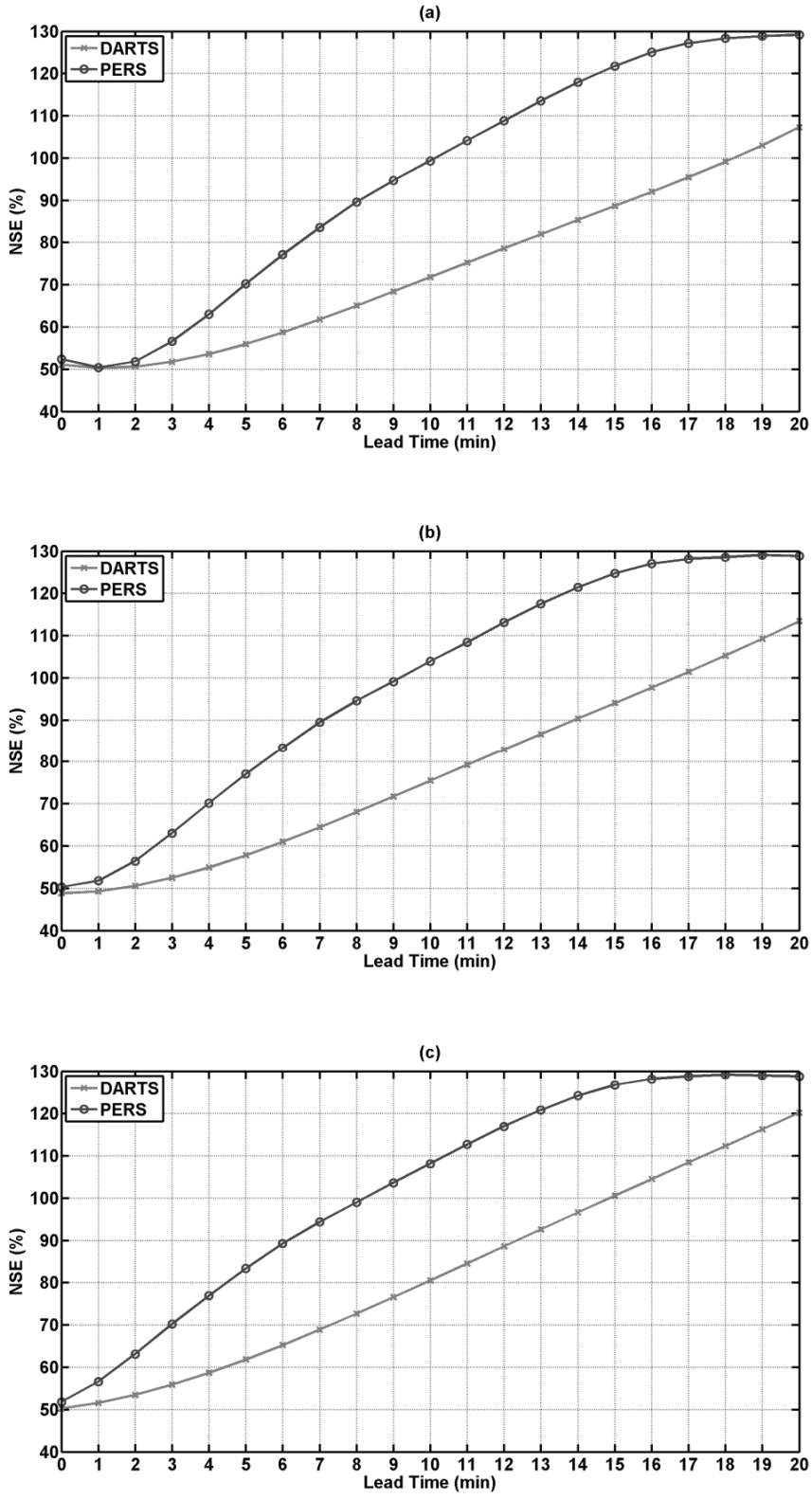

Figure 51. Normalized standard error scores averaged over the 05 May and 14 May 2009 CASA IP1 events illustrating the performance of nowcasting rain rate fields estimated from K_{dp} relative to rain gauge measurements for time lags of (a) 0, (b) 1, and (c) 2 min.

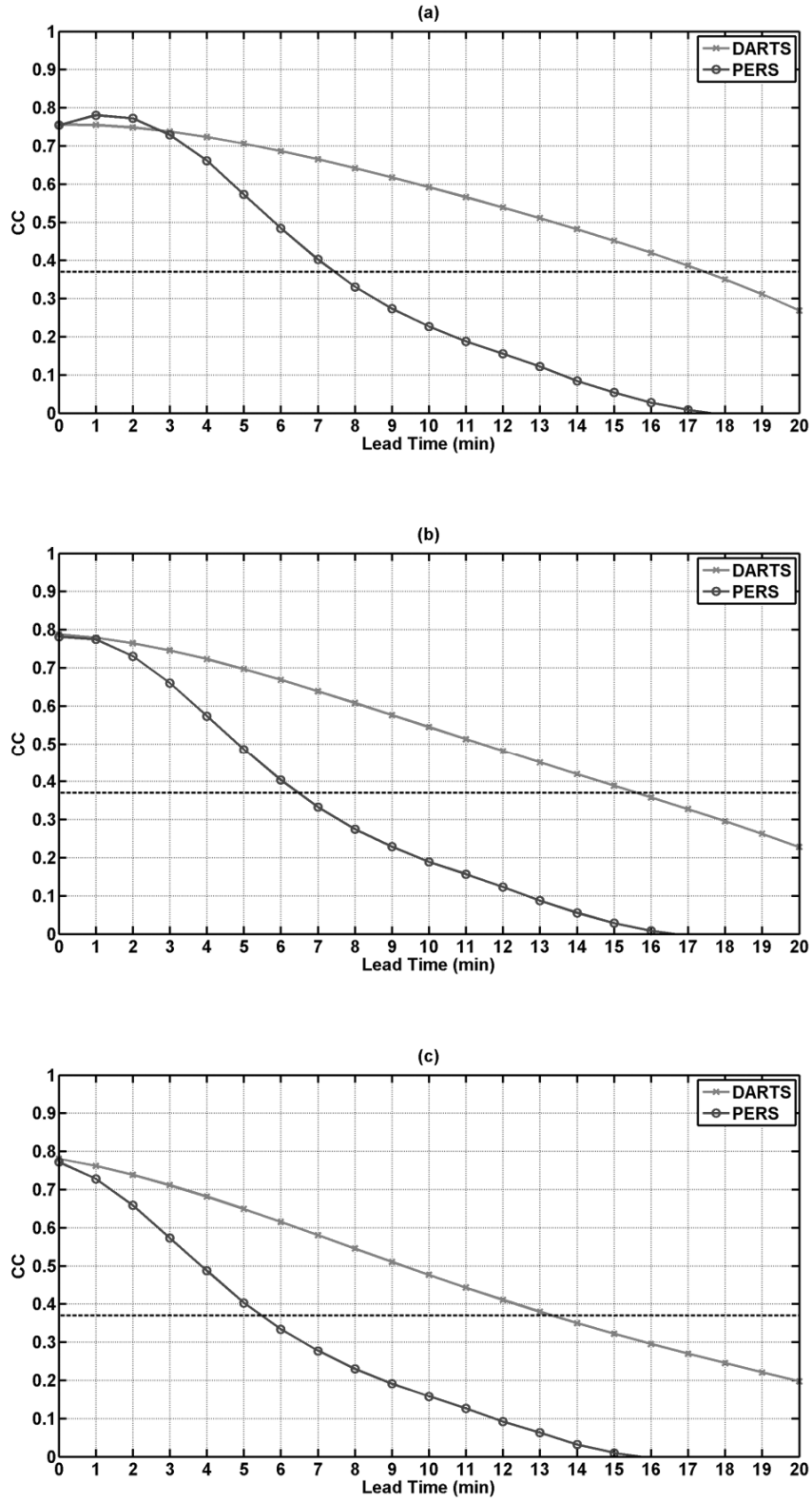

Figure 52. Cross-correlation coefficients averaged over the 05 May and 14 May 2009 CASA IP1 events illustrating the performance of nowcasting rain rate fields estimated from K_{dp} relative to rain gauge measurements for time lags of (a) 0, (b) 1, and (c) 2 min.

The values of NSE for Lagrangian persistence are seen to be consistently lower than those corresponding to Eulerian persistence from about a lead time of 3 min with a maximum difference of about 30% between lead times of 10–14 min. The values CC are shown to be higher for Lagrangian persistence relative to Eulerian persistence after a lead time of about 3 min, equating to lifetimes of approximately 17.5 and 7.5 min, respectively. These results are consistent with those shown in Figure 41 (which shows Lagrangian and Eulerian continuous lifetimes about 21 min and 14 min, respectively) and Figure 49 (which shows Lagrangian and Eulerian continuous lifetimes about 20 min and 11 min, respectively).

The results corresponding to Lagrangian persistence nowcasts for 1- and 2-min time lags show improvement in NB for the 0–5-min lead time frame at the expense of higher values at lead times greater than about 15 min. The NSE values are shown to be approximately equal for lead times up to 20 min. Cross-correlation values corresponding to 1- and 2-min time lags are slightly higher for the 0–6-min lead time frame after which they steadily decrease to values below those corresponding to the 0-min time lag. Estimates of lifetime decrease from about 17.5 min for the 0-min time lag to about 15.5 and 13.5 min for time lags of 1- and 2-min, respectively.

The NSE can be considered to be the strictest of the three metrics considered in this analysis. Since sample mean errors between radar estimates corresponding to each of the 20 gauge observations are calculated at each time, the NSE also includes potential bias errors, as the errors at different gauge locations cannot possibly cancel out leading to lower NB values. The cross-correlation does not take forecast bias into account, as it is possible for a forecast with large errors to still have a good correlation with the

corresponding observations (Wilks 2006). Krajewski et al. (2010) showed that average normalized differences between observations from 44–56 rain gauges located in the Oklahoma Mesonet (Brock et al. 1995) and the Little Washita Micronetwork and radar rainfall estimates made using the NEXRAD *Z-R* relationship applied to data collected during 20 Oklahoma storms selected from a 6-yr period from January 1998 to December 2003 by the Oklahoma City WSR-88D radar (KTLX) were between about 15% and 91%. Using 91% as a reference, the results shown in Figure 51 suggest nowcasting using rain fall fields derived from K_{dp} estimated using the method proposed by Wang and Chandrasekar (2009) and the DARTS and sinc kernel-based nowcasting methodology can be done to about out to about 15–16 min.

8.6.1 Nowcasting rainfall fields derived from K_{dp} estimates using CAPPI fields

The results in the preceding section were generated using estimated rainfall represented by PPI gridded data fields. Several studies comparing radar-based estimates of rainfall with rain gauge measurements considered the use of CAPPI data fields (Chumchean et al. 2004; Hossain et al. 2004; Wesson and Pegram 2006). A study was performed to compare the performance of nowcasting rainfall fields derived from K_{dp} estimates using data fields gridded from the 2^{o} surveillance scans (PPI) and gridded CAPPI data fields (Mohr and Vaughan 1979; Mohr et al. 1986).

Example CAPPI rain rate fields estimated using Eq (8.11) and corresponding 5-min predicted rain rate fields from the 05 May and 14 May data are shown in Figure 53. The average CC, ETS, and MAE scores computed relative to the initial CAPPI rain rate field estimates are shown in Figure 54.

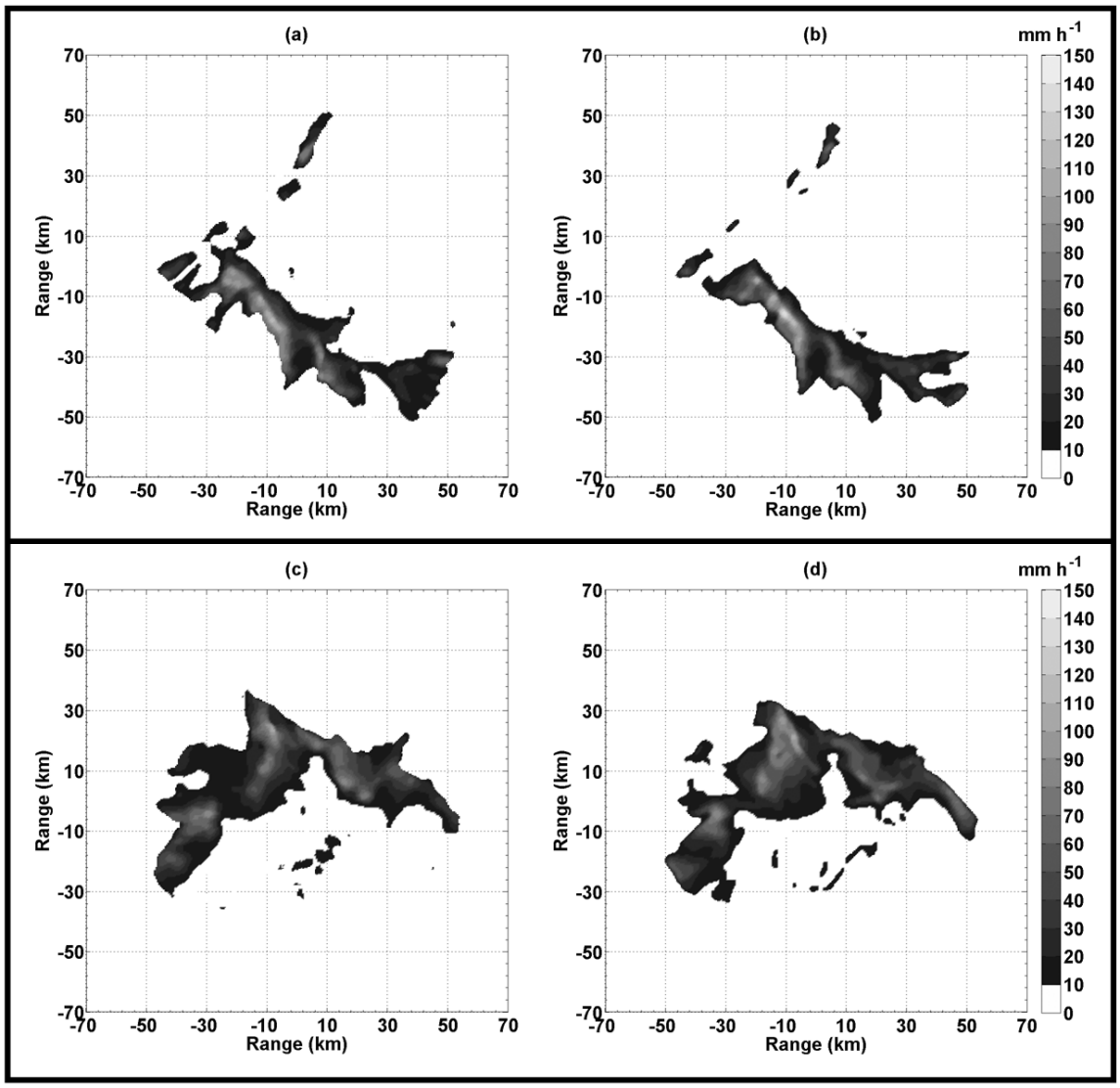

Figure 53. Example (a) estimated rain rate CAPPI field and (b) 5-min predicted rain rate CAPPI field corresponding to time 1517 UTC 05 May 2009 and (c) estimated rain rate field and (d) 5-min predicted rain rate field corresponding to time 0414 UTC 14 May 2009.

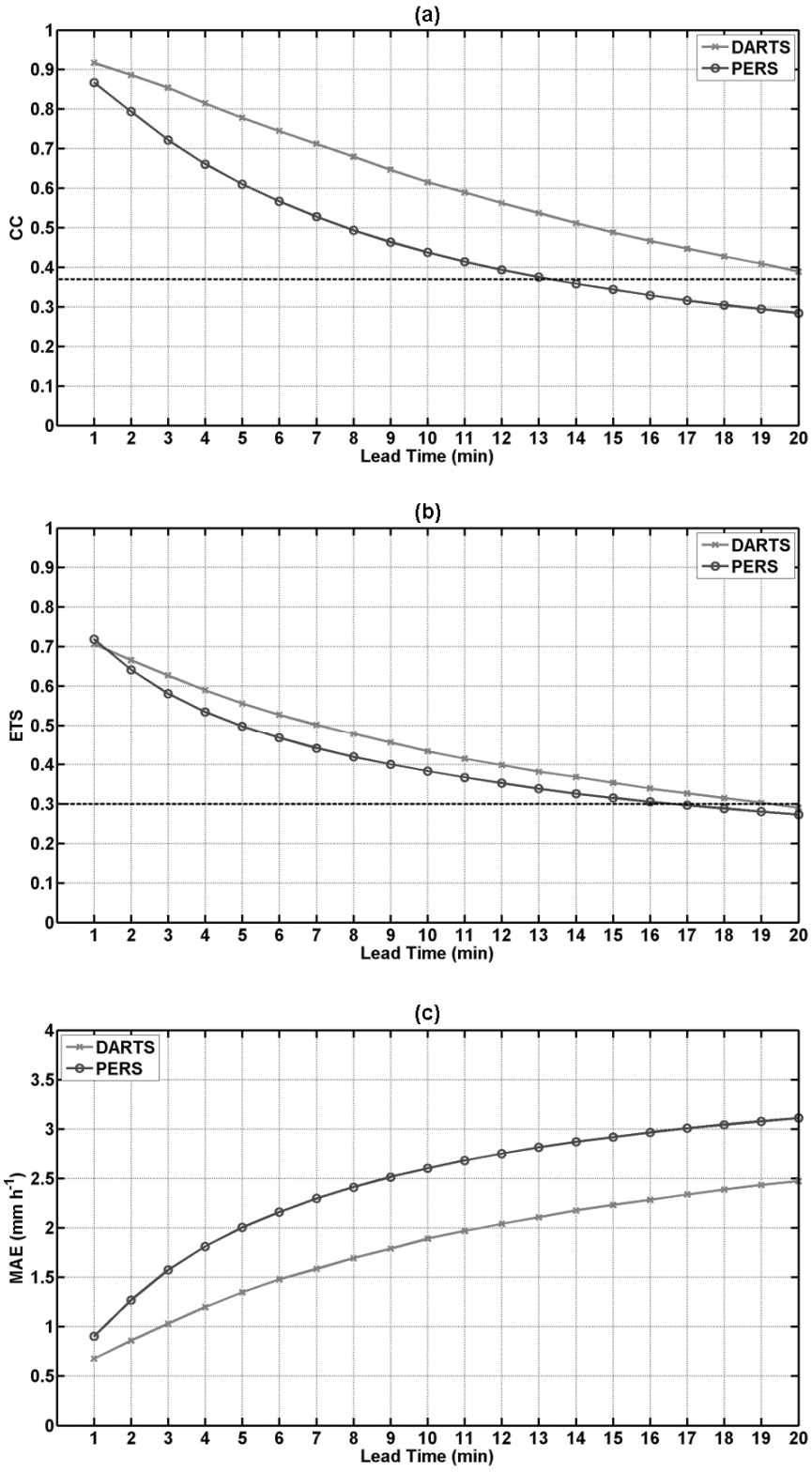

Figure 54. (a) CC, (b) ETS, and (c) MAE scores averaged over the 05 May and 14 May 2009 CASA IP1 events illustrating the performance of nowcasting CAPPI rain rate fields estimated from K_{dp} relative to initial CAPPI field estimates.

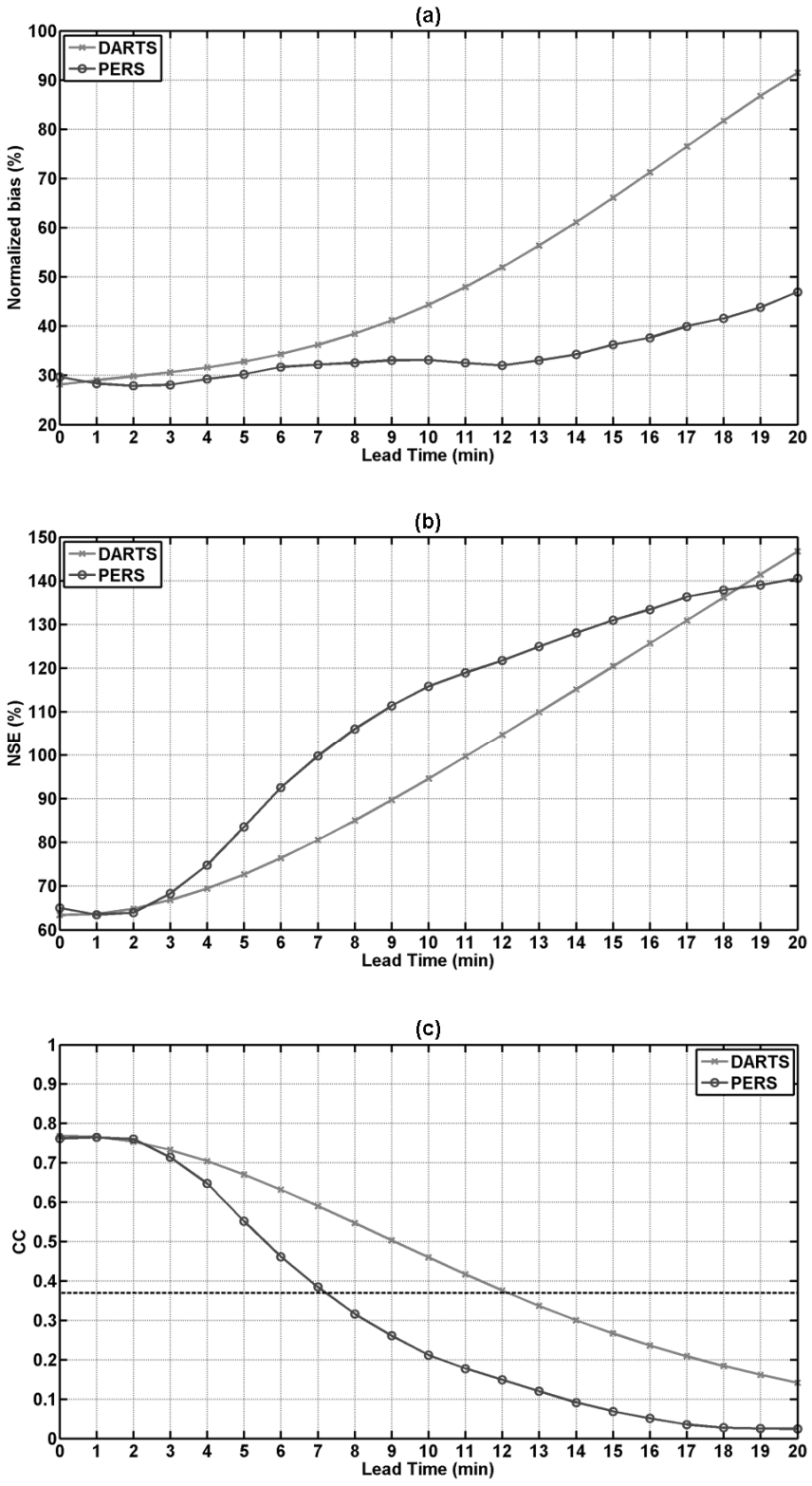

Figure 55. (a) NB, (b) NSE, and (c) CC scores averaged over the 05 May and 14 May 2009 CASA IP1 events illustrating the performance of nowcasting CAPPI rain rate fields estimated from K_{dp} relative to rain gauge measurements.

The results show continuous lifetimes to be about 21 and 13 min and categorical lifetimes to be about 19 and 16 min for Lagrangian and Eulerian persistence, respectively. MAE values are shown to be about 0.6 mm h^{-1} lower for Lagrangian persistence vs Eulerian persistence for a 20-min lead time. These results are consistent with or slightly better than those shown in Figure 49 which considered PPI data fields.

The average NB, NSE, and CC scores computed relative to rain gauge observations (considering a 0-min time lag of rain gauge measurements relative to radar estimates) are shown in Figure 55. Compared to the results shown in Figure 50 that considered using PPI fields for nowcasting, the results using CAPPI fields show consistent CC values but considerably higher initial average NB and NSE values. These results suggest future research considering nowcasting rainfall fields based on K_{dp} estimates using CASA radar data and the method for K_{dp} estimation presented by Wang and Chandrasekar (2009) should be done using PPI fields gridded using the method introduced by Liu et al. (2007).

8.7 Summary and conclusions

Rainfall field estimates using K_{dp} have been shown to be superior to those using reflectivity. K_{dp} is not susceptible to radar calibration error, attenuation, or beam blockage and are less affected by anomalous propagation. Rainfall rate estimates derived from K_{dp} are also less sensitive to variations in drop size distributions and to the presence of dry, tumbling hail than those derived from reflectivity. Additionally, X-band polarimetry offers important practical advantages over longer wavelength radar polarimetry,

including the provision for using K_{dp}-based rainfall estimators for lighter rainfall rates and smaller size and lower cost vs longer wavelength radars.

A new method to estimate K_{dp} has recently been developed. This method uses an adaptive scheme to estimate K_{dp} that avoids the need to unfold phases, which has been shown to have better range resolution in intense rain cells to capture the small-scale variability vs previous approaches.

This section presented preliminary results illustrating the feasibility of nowcasting rainfall fields estimated from K_{dp} derived from CASA X-band radar data and the method proposed by Wang and Chandrasekar (2009). The DARTS and sinc kernel-based nowcasting methodology was used to represent Lagrangian persistence. Approximately 9 h of data collected during the 05 May (multicell) and 14 May (supercell) CASA IP1 events were used for evaluation. Predicted K_{dp}-derived rainfall fields were generated up to a lead time of 20 min and were compared against an Eulerian persistence forecast. The results showed that the extent of useful nowcasts was approximately 20 and 18 min in a continuous (cross-correlation coefficient) and categorical (ETS) sense, respectively, when using DARTS, constituting approximate 82% and 29% relative improvements over Eulerian persistence, respectively.

In terms of nowcasting relative to rain gauge cross-validation, the continuous lifetime for Lagrangian persistence represented by nowcasts made by the DARTS and sinc kernel-based advection methodology was shown to be about 17.5 min, constituting an approximate 133% improvement over Eulerian persistence. Recent literature (Krajewski et al. 2010) shows initial normalized error between radar estimates of rainfall based on reflectivity and gauge observations to be as high as 91%. Using this value as a reference,

the results presented in this section suggest nowcasting rain fall fields derived from K_{dp} estimated using the method by Wang and Chandrasekar (2009) can be done out to about 15–16 min. The results also showed that introducing a delay between radar estimates and gauge measurements improved performance in the first few minutes of the lead time period. More data should be analyzed to form stronger conclusions and make further statements about the characteristics and nature of nowcasting rainfall fields derived from K_{dp}. Future research considering nowcasting rainfall fields based on K_{dp} estimates using CASA radar data and the method for K_{dp} estimation presented by Wang and Chandrasekar (2009) should be done using PPI fields gridded using data from the 2^{o} sweep and the method introduced by Liu et al. (2007).

CHAPTER IX. SUMMARY AND CONCLUSIONS

9.1 Summary

The salient contributions and results of this dissertation are summarized as follows:

1. The most important practical aspect of this work was the successful operational implementation of nowcasting in CASA DCAS via the DARTS motion estimation and sinc kernel-based advection methods. Development of the DARTS and sinc kernel-based nowcasting methodology was necessitated by the high-resolution nature of the CASA IP1 radar data (relative to current NEXRAD data) used for nowcasting. Nowcasting was used in this context to provide 1–10 min nowcasts for emergency manager decision support and 1–5 min nowcasts to control radar scan strategies to better observe the atmosphere. The nowcasting implementation was shown to be efficient by successfully processing high-resolution CASA radar data while running on a standard computer in a distributed environment, robust to data drops and mistiming due to network latency or long periods of inactivity, and portable by running on different machines at different locations. Results from the performance analysis using data from 17 precipitation events observed by the CASA radar network during the 2009 IP1 experiment showed DARTS outperformed a persistence forecast by approximately one standard deviation in terms of CSI and MAE scores and provided unanimous value to operational forecasters as measured by end-user surveys.

2. Currently state-of-the-art scale filtering methods were adapted and evaluated for use in the CASA DCAS nowcasting system to optimize performance. Results from the analysis of nowcasting performance using data from the 17 2009 IP1 events showed that Fourier filtering in the context of truncation of DARTS model coefficients was superior in terms of CSI and additional Fourier filtering of predicted reflectivity fields provided the best performance in terms of MAE.
3. DARTS was incorporated in the WSDDM system to provide more efficient and accurate estimates of SWE in support of aircraft deicing decision-making. DARTS was shown to provide an approximate 9% increase in performance in terms of CSI scores at a lead time of 60 min and provided a runtime reduction of approximately two orders of magnitude vs the cross-correlation-based nowcasting method currently used in WSDDM. The dataset used for evaluation consisted of approximately 69 h of data collected by a WMO DFIR standard reference gauge located at the NCAR Marshall Field Site and the KFTG WSR-88D during five winter precipitation events from 2007–2008. This study also showed that DARTS can be used successfully for nowcasting winter precipitation patterns observed by weather radar providing data with resolution lower than that provided by the CASA IP1 network.
4. The predictability of precipitation patterns represented by meteorological radar data is an important concept in the development of effective nowcasting systems by establishing a means to characterize precipitation patterns and features to provide an upper limit on the extent of the utility of nowcasting. Previous studies were extended to characterize the predictability of precipitation patterns depicted by radar observations to microalpha scale using DARTS and CASA IP1 radar data. The results

showed that nowcasting in CASA DCAS was generally useful to a lead time of about 20 min and that high spatial and temporal resolution data is necessary to make the best nowcasts. Preliminary results stratifying predictability results based on the type of the observed weather event were presented that showed relatively persistent, wide-spread supercell events to be the most predictable and single cell events to be the least predictable. Results of an investigation of the dependence of predictability on spatial and temporal scales supported the notion that lifetimes of larger-scale features are longer than those for smaller-scale features and that selective filtering should be used to improve nowcasting performance. A practical upper-bound on nowcasting was also established that was found to be about 10–12% higher in terms of lifetime than Lagrangian persistence. Comparison of predictability results presented here with those from studies conducted at larger scales suggested a linear relationship exists between the lifetimes of microalpha (0.2–2 km) to macrobeta (2000–10 000 km) scales in Eulerian and Lagrangian spaces.

5. Specific differential phase (K_{dp}) has been shown to provide more accurate and robust rainfall estimates relative to reflectivity and a new method to estimates K_{dp} has been developed. The challenge of estimating precipitation using weather radar and assessing accuracy using rain gauge data was extended to nowcasting rainfall fields estimated from radar data. The characteristics and extent of nowcasting rainfall fields estimated from K_{dp} were investigated using the currently latest method for K_{dp} estimation with CASA IP1 radar data and the DARTS and sinc kernel-based nowcasting methodology. The results corresponding to nowcasting performance assessed relative to initial rain rate field estimates were consistent with those

presented in Chapter VII. The results considering rain gauge cross-validation showed the extent of the utility of nowcasting was about 15–16 min.

9.2 Suggestions for future work

Suggestions for future work to extend this research include:

1. Extending the DARTS model to estimate motion in 3D to facilitate nowcasting the vertical profile of storms to provide better warning of impending severe weather and/or flooding.
2. Adapting the DARTS model to nowcast multi-Doppler wind fields for wind power/energy prediction..
3. Developing the DARTS model to estimate motion based on a weighted least-squares approach where more recent observations receive more weight to potentially improve accuracy of motion estimates.
4. Further developing the DARTS model based on turbulence studies (Schertzer et al. 1997; Venugopal et al. 1999; Seed 2003; Schleiss et al. 2009), which consider spatio-temporal scale dependence of atmospheric features at scales currently depicted by CASA radar observations and smaller scales potentially observed by next-generation high-resolution radars.
5. Incorporating real-time scoring capability in the operational CASA DCAS nowcasting system to develop a real-time estimate of forecast confidence.
6. Assimilating high-resolution CASA radar observations and nowcasts into an NWP model to potentially provide longer-term predictions of winds, rainfall, and atmospheric state.

7. Developing a multi-modal nowcasting system for use in CASA DCAS using surface measurements, NWP model output, and convective initiation capability in the model to predict boundary layer convergence (Stull 1997) and better predict the onset of severe weather.
8. Incorporating real-time, scale-based adaptive filtering in the DARTS nowcasting model by truncating model coefficients to match the geometry of small-scale precipitation features depicted by CASA radar observations and filter appropriate scales according to lead time. Such capability could improve nowcasting performance and the adaptivity of the filtering could be based on the physical characteristics of the weather event.
9. Investigating the use of different wavelet bases in a wavelet-based filtering method in the CASA nowcasting system to potentially improve nowcasting accuracy.
10. Applying scale filtering methods to the motion vector field estimated by DARTS to possibly improve nowcasting accuracy and to study the effects of motion vector field resolution on predictability.
11. Using DARTS and WSDDM to investigate winter storm characteristics by analyzing time series of calibrated a and b values in Eq (6.1).
12. Extending the analysis of the predictability of precipitation patterns observed by the CASA radar network using a larger dataset and more quantitative assessment methods [e.g., bias (Wilks 2006), Heidke Skill Score (Heidke 1926; Barnston 1992), Hanssen-Kuipers discriminant (Hanssen and Kuipers 1965), fractions skill score (Roberts and Lean 2008)] to more thoroughly analyze the dependence of

predictability on event type, intensity, and area, and extending such analysis to smaller atmospheric scales when enabling technology becomes available.

13. Extending the analysis of the characteristics and extent of nowcasting rainfall fields estimated from K_{dp} to include data from more events and investigate the spatio-temporal characteristics and predictability of such rainfall fields compared to rainfall fields estimated from reflectivity.
14. Exploring the relationship between K_{dp}-based rain fall estimates aloft and rain gauge measurements at the surface to make more accurate rain fall predictions and verification of such predictions.

REFERENCES

Accadia, C., S. Mariani, M. Casaioli, A. Lavagnini, and A. Speranza, 2003: Sensitivity of precipitation forecast skill scores to bilinear interpolation and a simple nearest-neighbor average method on high-resolution verification grids. *Wea. Forecasting*, **18**, 918–932.

Acheson, D. J., 1990: *Elementary Fluid Dynamics*. Oxford University Press, 408 pp.

Allen, P. B., and J. W. Naney, 1991: Hydrology of the Little Washita River Watershed, Oklahoma: Data and analyses. U.S. Department of Agriculture, Agricultural Research Service Publication ARS-90, 73 pp.

Baldwin, M. E., and J. S. Kain, 2006: Sensitivity of several performance measures to displacement error, bias, and event frequency. *Wea. Forecasting*, **21**, 636–648.

Barnston, A. G., 1992: Correspondence among the correlation, RMSE, and Heidke forecast verification measures; Refinement of the Heidke score. *Wea. Forecasting*, **7**, 699–709.

Bellon, A., and I. Zawadzki, 1994: Forecasting of hourly accumulations of precipitation by optimal extrapolation of radar maps. *J. Hydrol.*, **157**, 211–233.

Bocquet, F., 2002: Synoptic-scale signatures of warm-season mesoscale vortices in the Montreal region. Master's thesis, Dept. of Atmospheric and Oceanic Sciences, McGill University, 68 pp.

Boudevillain, B., and H. Andrieu, 2003: Assessment of Vertically Integrated Liquid (VIL) water content radar measurement. *J. Atmos. Oceanic Technol.*, **20**, 807–819.

Bowler, N. E., C. E. Pierce, and A. Seed, 2004: Development of a precipitation nowcasting algorithm based on optical flow techniques. *J. Hydrol.*, **288**, 74–91.

Bowler, N. E., C. E. Pierce, and, A. Seed, 2007: STEPS: A probabilistic precipitation forecasting scheme which merges an extrapolation nowcast with downscaled NWP. *Quart. J. Roy. Meteor. Soc.*, **132**, 2127–2155.

Brandes, E. A., A. V. Ryzhkov, and D. S. Zrnić, 2001: An evaluation of radar rainfall estimates from specific differential phase. *J. Atmos. Oceanic Technol.*, **18**, 363–375.

Brandes, E. A., G. Zhang, and J. Vivekanandan, 2002: Experiments in rainfall estimation with a polarimetric radar in a subtropical environment. *J. Appl. Meteor.*, **41**, 674–685.

Bringi V. N., V. Chandrasekar, and R. Xiao, 1998: Raindrop axis ratios and size distributions in Florida rainshafts: An assessment of multiparameter radar algorithms. *IEEE Trans. Geosci. Remote Sens.*, **36**, 703–715.

Bringi, V. N., and V. Chandrasekar, 2001: *Polarimetric Doppler Weather Radar: Principles and Applications*. Cambridge University Press, 662 pp.

Brock, F. V., K. C. Crawford, R. L. Elliott, G. W. Cuperus, S. J. Stadler, H. L. Johnson, and M. D. Eilts, 1995: The Oklahoma Mesonet: A technical overview. *J. Atmos. Oceanic Technol.*, **12**, 5–19.

Browning, K. A. 1979: The FRONTIERS plan: A strategy for using radar and satellite imagery for very short-range precipitation forecasting. *Meteor. Mag.*, **108**, 161–184.

Browning, K. A., 1980: Local weather forecasting. *Proc. Roy. Soc. London A*, **371**, 179–211.

Browning, K. A., 1982: *Nowcasting*. Academic Press, 256 pp.

Brunkow, D. A., V. N. Bringi, P. C. Kennedy, S. A. Rutledge, V. Chandrasekar, E. A. Mueller, and R. K. Bowie, 2000: A description of the CSU–CHILL national radar facility. *J. Atmos. Oceanic Technol.,* **17,** 1596–1608.

Buizza, R., A. Hollingsworth, A. Lalaurette, and A. Ghelli, 1999: Probabilistic predictions of precipitation using the ECMWF ensemble prediction system. *Wea. Forecasting,* **14,** 168–189.

Byers, H. R., and R. R. Braham, 1949: *The Thunderstorm*. U.S. Government Printing Office, 287 pp.

Cartwright, T. J., M. M. Wolfson, B. E. Forman, R. G. Hallowell, M. P. Moore, and K. E. Theriault, 1999: The FAA Terminal Convective Weather Forecast product: Scale separation filter optimization. Preprints, *29th Int. Conf. on Radar Meteorology*, Montreal, Quebec, Amer. Meteor. Soc., 852–855.

Chan, T. F., 1982: An improved algorithm for computing the singular value decomposition. *ACM Trans. Math. Software*, **8**, 72–83.

Chandrasekar, V., W. A. Cooper, and V. N. Bringi, 1988: Axis ratios and oscillations of raindrops. *J. Atmos. Sci.*, **45**, 1323–1333.

Chandrasekar, V., V. N. Bringi, N. Balakrishnan, and D. S. Zrnić, 1990: Error structure of multiparameter radar and surface measurements of rainfall. Part III: Specific differential phase. *J. Atmos. Oceanic Technol.*, **7**, 621-629.

Chandrasekar, V., and Coauthors, 2010: The CASA IP1 test-bed after 5 years of operation: Accomplishments, breakthroughs, challenges and lessons learned. *Proc. Sixth European Conf. on Radar in Meteorology and Hydrology,* Sibiu, Romania, National Meteorological Administration of Romania, 2.1. [Available online at http://www.erad2010.org/pdf/oral/monday/1_ERAD2010_0361.pdf.]

Chornoboy, E. S., A. M. Matlin, and J. P. Morgan, 1994: Automatic storm tracking for air traffic control. *Lincoln Labs. J.*, **7**, 427–448.

Chumchean, S., A. Seed, and A. Sharma, 2004: Application of scaling in radar reflectivity for correcting range-dependent bias in climatological radar rainfall estimates. *J. Atmos. Oceanic Technol.*, **21**, 1545–1556.

Cooley, J. W., and J. W. Tukey, 1965: An algorithm for the machine calculation of complex Fourier series. *Math Comput.*, **19**, 297–301.

Cornford, D., 2004: A Bayesian state space modeling approach to probabilistic quantitative precipitation forecasting. *J. Hydrol.*, **288**, 92–104.

Dance, S., E. Ebert, and D. Scurrah, 2010: Thunderstorm strike probability nowcasting. *J. Atmos. Oceanic Technol.*, **27**, 79–93.

Dixon, M., and G. Wiener, 1993: TITAN: Thunderstorm identification, tracking, analysis, and nowcasting—a radar-based methodology. *J. Atmos. Oceanic Technol.*, **10**, 785–797.

Donaldson, R., R. Dyer, and M. Krauss, 1975: An objective evaluator of techniques for predicting severe weather events. Preprints, *Ninth Conf. on Severe Local Storms*, Norman, OK, Amer. Meteor. Soc., 321–326.

Doswell, C. A., R. Davies-Jones, and D. L. Keller, 1990: On summary measures of skill in rare event forecasting based on contingency tables. *Wea. Forecasting*, **5**, 576–585.

DuFran, Z. M., R. L. Carpenter, and B. L. Shaw, 2009: Improved precipitation nowcasting algorithm using a high-resolution NWP model and national radar mosaic. Preprints, *34th Int. Conf. on Radar Meteorology*, Williamsburg, VA, Amer. Meteor. Soc., 3B.6. [Available online at http://ams.confex.com/ams/pdfpapers/156040.pdf.]

Dupree, W., and Coauthors, 2009: The 2008 CoSPA forecast demonstration. Preprints, *14th Conf. on Aviation, Range, and Aerospace Meteor.,* Phoenix, AZ, Amer. Meteor. Soc., P1.1. [Available online at http://ams.confex.com/ams/pdfpapers/151488.pdf.]

Durran, D. R., 2000: Comments on "The differentiation between grid spacing and resolution and their application to numerical modeling". *Bull Amer. Meteor. Soc.*, **81**, 2478–2479.

Dutta, D., D. K. Sarma, M. Konwar, S. Sharma, G. Viswanathan, R. M. Gairola, J. Das, B. A. M. Kannan, and S. Venkateswaralu, 2010: Nowcasting of yes/no rain situations at a station using soft computing technique to the radar imagery. *Indian J. Radio Space Phys.*, **39**, 92–102.

Ebert, E. E., and J. L. McBride, 2000: Verification of precipitation in weather systems: determination of systematic errors. *J. Hydrol.*, **239**, 179–202.

Ebert, E. E., L. J. Wilson, B. G. Brown, P. Nurmi, H. E. Brooks, J. Bally, and M. Jaeneke, 2004: Verification of nowcasts from the WWRP Sydney 2000 Forecast Demonstration Project. *Wea. Forecasting*, **19**, 73–96.

Ehrendorfer, M., 1994: The Liouville equation and its potential usefulness for the prediction of forecast skill. Part I: Theory. *Mon. Wea. Rev.*, **122**, 703–713.

Ehrendorfer, M., R. M. Errico, and K. D. Raeder, 1999: Singular-vector perturbation growth in a primitive equation model with moist physics. *J. Atmos. Sci.,* **56,** 1627–1648.

Epstein, E. S., 1969: Stochastic dynamic prediction. *Tellus*, **21**, 739–759.

Fox, N. I., and C. K. Wikle, 2005: A Bayesian quantitative precipitation nowcast scheme. *Wea. Forecasting*, **20**, 264–275.

Fritsch, F. N., and R. E. Carlson, 1980: Monotone piecewise cubic interpolation. *SIAM J. Numer. Anal.*, **17**, 238–246.

Fujita, T. T., 1981: Tornadoes and downbursts in the context of generalized planetary scales. *J. Atmos. Sci.*, **38**, 1511–1534.

Fulker, D., R. K. Rew, and A. Wilson, 2000: A TCP/IP-based system for reliably disseminating near-real-time meteorological data. *CBS Technical Conference on WMO Information Systems and Services*, Geneva, Switzerland, 27–28

Gerald, C., and P. Wheatley, 2003: *Applied Numerical Analysis,* 7th ed. Addison-Wesley, 624 pp.

Gerapetritis, H., and J. M. Pelissier, 2004: The critical success index and warning strategy. *Proc. 17th Conf. on Probability and Statistics in the Atmospheric Sciences*, Seattle, WA, Amer. Meteor. Soc., 2.10. [Available online at http:// ams.confex.com/ams/pdfpapers/70691.pdf.]

Germann, U., and I. Zawadzki, 2002: Scale-dependence of the predictability of precipitation from continental radar images. Part I: Description of the methodology. *Mon. Wea. Rev.*, **130**, 2859–2873.

Germann, U., and I. Zawadzki, 2004: Scale dependence of the predictability of precipitation from continental radar images. Part II: Probability forecasts. *J. Appl. Meteor.*, **43**, 74–89.

Germann, U., I. Zawadzki, and B. Turner, 2006: Predictability of precipitation from continental radar images. Part IV: Limits to prediction. *J. Atmos. Sci.*, **63**, 2092–2108.

Gibbs, J. W., 1902: *Elementary principles in statistical mechanics*. C. Scribner, 207 pp.

Gilbert, G. K., 1884: Finley's tornado predictions. *Amer. Meteor. J.*, **1**, 166–172.

Gleeson, T. A., 1966: A causal relation for probabilities in synoptic meteorology. *J. Appl. Meteor.*, **5**, 365–368.

Golding, B., 1998: Nimrod: A system for generating automatic very-short-range forecasts. *Meteor. Appl.* **5**, 1–16.

Goldstein, H., 2001: *Classical Mechanics,* 3rd ed. Addison-Wesley, 680 pp.

Golestani, Y., V. Chandrasekar, and V. N. Bringi, 1989: Intercomparison of multiparameter radar measurements. Preprints, *24th Int. Conf. on Radar Meteorology*, Tallahassee, FL, Amer. Meteor. Soc., 309–314.

Gonzalez, R. C., and R. E. Woods, 2002: *Digital Image Processing,* 2nd ed. Prentice Hall, 793 pp.

Gorgucci, E., G. Scarchilli, V. Chandrasekar, and V.N. Bringi, 2001: Rainfall estimation from polarimetric radar measurements: Composite algorithms immune to variability in raindrop shape-size relation. *J. Atmos. Oceanic Technol.*, **18**, 1773–1786.

Grasso, L. D., 2000: The differentiation between grid spacing and resolution and their application to numerical modeling. *Bull. Amer. Meteor. Soc.,* **81,** 579–580.

Grassotti, C., R. N. Hoffman, E. R. Vivoni, D. Entekhabi, 2003: Multiple-timescale intercomparison of two radar products and rain gauge observations over the Arkansas–Red River Basin. *Wea. Forecasting*, **18**, 1207–1229.

Grecu, M., and W. F. Krajewski, 2000: A large-sample investigation of statistical procedures for radar-based short-term quantitative precipitation forecasting. *J. Hydrol.*, **239**, 69–84.

Greene D. R., and R. A. Clark, 1972: Vertically integrated liquid water—a new analysis tool. *Mon. Wea. Rev.*, **100**, 548–552.

Hamill, T. M., 1999: Hypothesis tests for evaluating numerical precipitation forecasts. *Wea. Forecasting*, **14**, 155–167.

Han, L. Y., S. Fu, L. Zhao, Y. Zheng, H. Wang, and Y. Lin, 2009: 3D convective storm identification, tracking and forecasting—an enhanced TITAN algorithm. *J. Atmos. Oceanic Technol.,* **26**, 719–732.

Handwerker, J., 2002: Cell tracking with TRACE3D—a new algorithm. *Atmos. Res.*, **61**, 15–34.

Hanssen, A. W., and W. J. A. Kuipers, 1965: On the relationship between the frequency of rain and various meteorological parameters. *Mededeelingen en Verhandelingen*, **81**, 2–15.

Heidke, P., 1926: Berechnung des erfolges und der güte der windstärkevorhersagen im sturmwarnungsdienst. *Geografika Annaler*, **8**, 301–349.

Hering, A. M., C. Morel, G. Galli, S. Sénési, P. Ambrosetti, and M. Boscacci, 2004: Nowcasting thunderstorms in the Alpine region using a radar based adaptive thresholding scheme. *Proc. Third European Conf. on Radar in Meteorology and Hydrology,* Visby, Sweden, Copernicus Gmbh, 206–211.

Higgins, J. R., 1996: *Sampling Theory in Fourier and Signal Analysis: Foundations*. Oxford University Press, 236 pp.

Hilgendorf, E. R., and R. H. Johnson, 1998: A study of the evolution of mesoscale convective systems using WSR-88D data. *Wea. Forecasting*, **13**, 437–452.

Hogan, R. J., C. A. T. Ferro, I. T. Jolliffe, and D. B. Stephenson, 2010: Equitability revisited: Why the "Equitable Threat Score" is not equitable. *Wea. Forecasting*, **25**, 710–726.

Hohti, H., J. Koistinen, P. Nurmi, E. Saltikoff, and K. Holmlund, 2000: Precipitation nowcasting using radar-derived atmospheric motion vectors. *Phys. Chem. Earth*, **25B**, 1323–1327.

Hossain, F., E. N. Anagnostou, T. Dinku, and M. Borga, 2004: Hydrological model sensitivity to parameter and radar rainfall estimation uncertainty. *Hydrol. Proc.*, **18**, 3277–3291.

Hubbert, J., V. Chandrasekar, V. N. Bringi, and P. Meischner, 1993: Processing and interpretation of coherent dual-polarized radar measurements. *J. Atmos. Oceanic Technol.*, **10**, 155–164.

Hubbert, J., and V. N. Bringi, 1995: An iterative filtering technique for the analysis of copolar differential phase and dual-frequency radar measurements. *J. Atmos. Oceanic Technol.*, **12**, 643–648.

Jacobson, M. Z., 2005: *Fundamentals of Atmospheric Modeling*, 2nd ed. Cambridge University Press, 828 pp.

Jameson, A., 1985: Microphysical interpretation of multiparameter radar measurements in rain. Part III: Interpretation and measurement of propagation differential phase shift between orthogonal linear polarizations. *J. Atmos. Sci.*, **42**, 607–614.

Joe, P., M. Falla, P. V. Rijn, L. Stamadianos, T. Falla, D. Magosse, L. Ing, and J. Dobson, 2003: Radar data processing for severe weather in the National Radar Project of Canada. Preprints, *21st Conf. on Severe Local Storms,* San Antonio, TX, Amer. Meteor. Soc., 221–224.

Joe, P., and Coauthors, 2010: Weather services, science advances, and the Vancouver 2010 Olympic and Paralympic Winter Games. *Bull. Amer. Meteor. Soc.*, **91**, 31–36.

Jogalekar, P. and M. Woodside, 2000: Evaluating the scalability of distributed systems. *IEEE Trans. Parallel and Distributed Syst.*, **11**, 589–603.

Johnson, J. T., P. L. Mackeen, A. Witt, E. D. Mitchell, G. J. Stumpf, M. D. Eilts and K. W. Thomas, 1998: The storm cell identification and tracking algorithm: An enhanced WSR-88D algorithm. *Wea. Forecasting*, **13**, 263–276.

Johnson, S. G., and M. Frigo, 2007: A modified split-radix FFT with fewer arithmetic operations. *IEEE Trans. Signal Proc.*, **55**, 111–119.

Jones, G. L., and J. P. Hobert, 2002: Markov Chain Monte Carlo. *The Encyclopedia of Environmetrics*, A. H. El-Shaarawi and W. W. Piegorsch, Eds. Wiley, 1199–1207.

Junyent, F., and V. Chandrasekar, 2009: Theory and characterization of weather radar networks. *J. Atmos. Oceanic Technol.,* **26,** 474–491.

Junyent, F., V. Chandrasekar, D. McLaughlin, E. Insanić, and N. Bharadwaj, 2010: The CASA Integrated Project 1 networked radar system. *J. Atmos. Oceanic Technol.*, **27**, 61–78.

Krajewski, W. F., G. Villarini, and J. A. Smith, 2010: Radar-rainfall uncertainties. *Bull. Amer. Meteor. Soc.*, **91**, 87–94.

Kurose, J., E. Lyons, D. McLaughlin, D. Pepyne, B. Philips, D. Westbrook, and M. Zink, 2006: An end-user-responsive sensor network architecture for hazardous weather

detection, prediction, and response. *Proc. Second Asian Internet Engineering Conf.,* Pathumthani, Thailand, Asian Institute of Technology, 1–15.

Lakshmanan, V., 2000: Speeding up a large-scale filter. *J. Atmos. Oceanic Technol.*, **17**, 468–473.

Lakshmanan, V., R. Rabin, and V. DeBrunner, 2003: Multiscale storm identification and forecast. *J. Atmos. Res.*, **67**, 367–380.

Landolt, S., M. Tryhane, R. Rasmussen, and J. Cole, 2004: Characterization of wind flow in and around an alter shielded snowgauge. Preprints, *11th Conf. on Aviation, Range, and Aerospace Meteorology*, Hyannis, MA, Amer. Meteor. Soc., 7.3. [Available online at http://ams.confex.com/ams/pdfpapers/81894.pdf.]

Laroche S., and I. Zawadzki, 1994: A variational analysis method for retrieval of three-dimensional wind field from single-Doppler radar data. *J. Atmos. Sci.,* **51**, 2664–2682.

Lee, G. W., and I. Zawadzki, 2005: Variability of drop size distributions: Time-scale dependence of the variability and its effects on rainfall estimation. *J. Appl. Meteor.*, **44**, 241–255.

Li, L. W., W. Schmid, and J. Joss, 1995: Nowcasting of motion and growth of precipitation with radar over a complex orography. *J. Appl. Meteor.*, **34**, 1286–1299.

Li, P. W., and E. S. T. Lai, 2004: Short-range quantitative precipitation forecasting in Hong Kong. *J. Hydrol.*, **288**, 189–209.

Liu, Y., Y. Wang, V. Chandrasekar, and V. N. Bringi, 2007: Real-time three-dimensional radar mosaic in CASA IP1 testbed. *Proc. 2007 IEEE Int. Geoscience and Remote Sensing Symp.*, Barcelona, Spain, IEEE, 2754–2757.

Lorenz, E. N., 1973: On the existence of extended range predictability. *J. Appl. Meteor.*, **12**, 543–546.

Maddox, A. M., 2010: The importance of proper clutter filtering. *NEXRAD Now*, **19**, 8–12. [Available online at http://www.roc.noaa.gov/WSR88D/PublicDocs/NNOW/NNwinter093/ProperClutterFiltering.pdf.]

Maki, M. T., and Coauthors, 2008: X-band Polarimetric Radar Network in the Tokyo Metropolitan Area—X-NET, *Extended Abstracts*, *Fifth European Conf. on Radar in Meteorology and Hydrology*, Helsinki, Finland, Finnish Meteorological Institute, 3.7.

Mason, I. B., 1989: Dependence of the critical success index on sample climate and threshold probability. *Aust. Meteor. Mag.*, **37**, 75–81.

Mason, I. B., 2003: Binary events. *Forecast Verification—A Practitioner's Guide in Atmospheric Science*, I. T. Jolliffe and D. B. Stephenson, Eds., Wiley, 37–76.

Massacand, A. C., H. Wernli, and H. C. Davies, 1998: Heavy precipitation on the alpine south-side: An upper-level precursor. *Geophys. Res. Lett.,* **25,** 1435–1438.

Matrosov, S. Y., K. A. Clark, B. E. Martner, and A. Tokay, 2002: X-Band polarimetric radar measurements of rainfall. *J. Appl. Meteor.*, **41**, 941–952.

Matrosov, S. Y., R. Cifelli, P. C. Kennedy, S. W. Nesbit, S. A. Rutledge, V. N. Bringi, and B. E. Martner, 2006: A comparative study of rainfall retrievals based on specific differential phase shifts at X- and S-Band radar frequencies. *J. Atmos. Oceanic Technol.*, **23**, 952–963.

McLaughlin, D. J., and Coauthors, 2005: Distributed Collaborative Adaptive Sensing (DCAS) for improved detection, understanding, and predicting of atmospheric hazards. Preprints, *Ninth Symp. on Integrated Observing and Assimilation Systems for the Atmosphere, Oceans, and Land Surface,* San Diego, CA, Amer. Meteor. Soc., 11.3.

McLaughlin, D. J., and Coauthors, 2009: Short-wavelength technology and the potential for distributed networks of small radar systems. *Bull. Amer. Meteor. Soc.*, **90**, 1797–1817.

Mecklenburg, S., J. Joss, and W. Schmid, 2000: Improving the nowcasting of precipitation in an Alpine region with an enhanced radar echo tracking algorithm. *J. Hydrol.*, **239**, 46–68.

Megenhardt, D. L., C. Mueller, S. Trier, D. Ahijevych, and N. Rehak, 2004: NCWF-2 probabilistic forecasts. Preprints, *11th Conf. on Aviation, Range, and Aerospace Meteorology*, Hyannis, MA, Amer. Meteor. Soc., 5.2. [Available online at http://ams.confex.com/ams/pdfpapers/81993.pdf.]

Mesinger, F., 2008: Bias adjusted precipitation threat scores. *Adv. Geosci.*, **16**, 137–142.

Mitra, S. K., 2005: *Digital Signal Processing: A Computer-Based Approach,* 3rd ed. McGraw-Hill, 896 pp.

Mohr, C. G., and R. L. Vaughan, 1979: An economical procedure for Cartesian interpolation and display of reflectivity factor data in three-dimensional space. *J. Appl. Meteor.*, **18**, 661–670.

Mohr, C. G., L. J. Miller, R. L. Vaughan, and H. W. Frank, 1986: The merger of mesoscale datasets into a common Cartesian format for efficient and systematic analyses. *J. Atmos. Oceanic Technol.*, **3**, 143–161.

Montanari, L., A. Montanari, and E. Toth, 2006: A comparison and uncertainty assessment of system analysis techniques for short-term quantitative precipitation nowcasting based on radar images. *J. Geophys. Res.*, **111**, D14111.

Mueller, C., T. Saxen, R. Roberts, J. Wilson, T. Betancourt, S. Detling, N. Oien, and H. Yee, 2003: NCAR Auto-Nowcaster system. *Wea. Forecasting*, **18**, 545–561.

National Oceanic and Atmospheric Administration, cited 2010: National weather service glossary. [Available online at http://www.nws.noaa.gov/glossary/.]

National Research Council, 1995: *Assessment of NEXRAD Coverage and Associated Weather Services*, Washington, D. C.: National Academies Press, 104 pp.

National Research Council, 2002: *Weather Technology beyond NEXRAD*. Washington, D. C.: National Academies Press, 72 pp.

National Research Council, 2009: *Observing Weather and Climate from the Ground Up: A Nationwide Network of Networks*. Washington, D. C.: National Academies Press, 234 pp.

Novák, P., 2007: The Czech Hydrometeorological Institute's severe storm nowcasting system. *Atmos. Res.*, **83**, 450–457.

Orlanski, I., 1975: A rational subdivision of scales for atmospheric processes. *Bull. Amer. Meteor. Soc.*, **56**, 527–530.

Ostiguy, L., and J. P. R. Laprise, 1990: On the positivity of mass in commonly used numerical transport schemes. *Atmos.–Ocean,* **28,** 147–161.

Otsuka, K., O. Keihiro, S. Satoshi, H. Tsutomu, O. Toshinor, and I. Michihiro, 1999: Short-time local precipitation nowcasting system: MyWeather. *Trans. Info. Proc. Soc. Japan*, **40**, 1117–1126.

Palmer, T. N., 1993: Extended-range atmospheric prediction and the Lorenz model. *Bull. Amer. Meteor. Soc.*, **74**, 49–65.

Park, S. G., M. Maki, K. Iwanami, V. N. Bringi, and V. Chandrasekar, 2005: Correction of radar reflectivity and differential reflectivity for rain attenuation at X Band. Part II: Evaluation and application. *J. Atmos. Oceanic Technol.*, **22**, 1633–1655.

Pellarin, T., G. Delrieu, G.-M. Saulnier, H. Andrieu, B. Vignal, and J. D. Creutin, 2002: Hydrologic visibility of weather radar systems operating in mountainous regions: Case study for the Ardéche catchment (France). *J. Hydrometeor.*, **3**, 539–555.

Philips, B., and Coauthors, 2007: Integrating end user needs into system design and operation: The Center for Collaborative Adaptive Sensing of the Atmosphere (CASA).

Preprints, *16th Conf. on Applied Climatology*, San Antonio, TX, Amer. Meteor. Soc., 3.14. [Available online at http://ams.confex.com/ams/pdfpapers/119996.pdf.]

Phillips, B., D. Westbrook, D. Pepyne, J. Brotzge, E. J. Bass, and D. Rude, 2008: User evaluations of adaptive scanning patterns in the CASA Spring Experiment 2007. *Proc. 2008 IEEE Int. Geoscience and Remote Sensing Symp.*, Boston, MA, IEEE, V-156–V-159.

Pierce, C. E., C. G. Collier, P. J. Hardaker, and C. M. Haggett, 2000: GANDOLF: A system for generating automated nowcasts of convective precipitation. *Meteor. Appl.*, **8**, 341–360.

Pierce, C. E., A. W. Seed, M. Sleigh, C. G. Collier, N. I. Fox, N. Donaldson, J. W. Wilson, R. Roberts, and C. K. Mueller, 2004: The nowcasting of precipitation during Sydney 2000: An appraisal of the QPF algorithms. *Wea. Forecasting*, **19**, 7–21.

Rasmussen, R., M. Dixon, F. Hage, J. Cole, C. Wade, J. Tuttle, S. McGettigan, T. Carty, L. Stevenson, W. Fellner, S. Knight, E. Karplus, and N. Rehak, 2001: Weather Support to Deicing Decision Making (WSDDM): A winter weather nowcasting system. *Bull. Am. Meteor. Soc.*, **82**, 579–595.

Rasmussen, R., M. Dixon, S. Vasiloff, F. Hage, S. Knight, J. Vivekanandan, and M. Xu, 2003: Snow nowcasting using a real-time correlation of radar reflectivity with snow gauge accumulation. *J. Appl. Meteor.*, **42**, 20–36.

Rew, R. K. and G. P. Davis, 1990a: NetCDF: An interface for scientific data access. *IEEE Computer Graphics Appl.*, **10**, 76–82.

Rew, R. K. and G. P. Davis, 1990b: Distributed data capture and processing in a local area network. Preprints, *Sixth Int. Conf. on Interactive Information and Processing Systems for Meteorology, Oceanography and Hydrology*, Anaheim, CA, Amer. Meteor. Soc., 69–72.

Rinehart, R. E., and E. T. Garvey, 1978: Three-dimensional storm motion detection by conventional weather radar. *Nature*, **273**, 287–289.

Rinehart, R. E., 1981: A pattern-recognition technique for use with conventional weather radar to determine internal storm motions. *Atmos. Technol.*, **13**, 119–134.

Robert, A., 1981: A stable numerical integration scheme for the primitive meteorological equations. *Atmos.-Ocean*, **19**, 35-46.

Roberts, N. M., H. W. Lean, 2008: Scale-selective verification of rainfall accumulations from high-resolution forecasts of convective events. *Mon. Wea. Rev.*, **136**, 78–97.

Rood, R. B., 1987: Numerical advection algorithms and their role in atmospheric transport and chemistry models. *Rev. Geophys.,* **25**, 71–100.

Ruzanski, E., Y. Wang, and V. Chandrasekar, 2009: The CASA nowcasting system. *Extended Abstracts, World Meteorological Organization Symp. on Nowcasting*, Whistler, British Columbia, World Weather Research Programme, CD-ROM, 5.4.

Ryzhkov, A. V., S. E. Giangrande, and T. J. Schuur, 2005: Rainfall estimation with a polarimetric prototype of WSR-88D. *J. Appl. Meteor.*, **44**, 502–515.

Sachidananda, M., and D. S. Zrnić, 1986: Differential propagation phase shift and rainfall rate estimation. *Radio Sci.*, **21**, 235–247.

Sawyer, J. S., 1963: A semi-Lagrangian method for solving the vorticy advection equation. *Tellus*, **15**, 336-342.

Schaefer, J. T., 1990: The critical success index as an indicator of warning skill. *Wea. Forecasting*, **5**, 570–575.

Schertzer, D., S. Lovejoy, F. Schmitt, Y. Chigirinskaya, and D. Marsan, 1997: Multifractal cascade dynamics and turbulent intermittency. *Fractals,* **5,** 427–471.

Schleiss, M. A., A. Berne, R. Uijlenhoet, 2009: Geostatistical simulation of two-dimensional fields of raindrop size distributions at the meso-γ scale. *Water Resour. Res.*, **45**, W07415, doi:10.1029/2008WR007545.

Schmeits, M. J., K. J. Kok, D. H. P. Vogelezang, and R. M. V. Westrhenen, 2008: Probabilistic forecasts of (severe) thunderstorms for the purpose of issuing a weather alarm in the Netherlands. *Wea. Forecasting*, **23**, 1253–1267.

Seed, A. W., 2003: A dynamic and spatial scaling approach to advection forecasting. *J. Appl. Meteor.,* **42**, 381–388.

Seliga, T. A., and V. N. Bringi, 1978: Differential reflectivity and differential phase shift: Applications in radar meteorology. *Radio Sci.*, **13**, 271–275.

Shannon, C. E., 1949: Communication in the presence of noise. *Proc. Inst. Radio Eng.*, **37**, 10–21.

Sinclair, S., and G. G. S. Pegram, 2005: Empirical Mode Decomposition in 2-D space and time: A tool for space-time rainfall analysis and nowcasting. *Hydrol. Earth Syst. Sci.*, **9**, 127–137.

Smalley, D. J., B. J. Bennett, and M. L. Pawlak, 2003: New products for the NEXRAD ORPG to support FAA critical systems. Preprints, *19th Conf. on Interactive Information Processing Systems in Meteorology, Oceanography, and Hydrology*

Long Beach, CA, Amer. Meteor. Soc., 14.12. [Available online at http://ams.confex.com/ams/pdfpapers/57174.pdf.]

Staniforth A., and J. Cote, 1991: Semi-Lagrangian integration schemes for atmospheric models—a review. *Mon. Wea. Rev*., **119**, 2206–2223.

Stefl, B. A., and K. F. George, 1992: Anitfreezes and deicing fluids. *Kirk-Othmer Encyclopedia of Chemical Technology*, Wiley, 22 950 pp.

Steinheimer, M., and T. Haiden, 2007: Improved nowcasting of precipitation based on convective analysis fields. *Adv. Geosci.*, **10**, 125–131.

Stensrud, D. J., and M. S. Wandishin, 2000: The correspondence ratio in forecast evaluation. *Wea. Forecasting*, **15**, 593–602.

Stephenson, D. B., B. Casati, C. A. T. Ferro, and C. A. Wilson, 2008: The extreme dependency score: A non-vanishing measure for forecasts of rare events. *Meteor. Appl.*, **15**, 41–50.

Stull, R., 1997: *An Introduction to Boundary Layer Meteorology*. Kluwer Academic, 670 pp.

Su, L. K., and N. T. Clemens, 2003: The structure of fine-scale scalar mixing in gas-phase planar turbulent jets. *J. Fluid Mech.*, **488**, 1–29.

Tartaglione, N., 2010: Relationship between precipitation forecast errors and skill scores of dichotomous forecasts. *Wea. Forecasting*, **25**, 355–365.

Thurai, M., and V. N. Bringi, 2005: Drop axis ratios from a 2D video disdrometer. *J. Atmos. Oceanic Technol.*, **22**, 966–978.

Tomassetti, B., F. S. Marzano, M. Montopoli, and M. Verdecchia, 2008: Rainfall radar nowcasting using a neural-network cascade approach. *Proc. Fifth European Conf. on Radar in Meteorology and Hydrology*, Helsinki, Finland, Finnish Meteorological Institute, P11.8. [Available online at http://erad2008.fmi.fi/proceedings/extended/erad2008-0078-extended.pdf.]

Tsai, D.-M., and C.-T. Lin, 2003: Fast normalized cross correlation for defect detection. *Pattern Recognit. Lett.*, **15**, 2625–2631.

Tsonis, A. A., and G. L. Austin, 1981: An evaluation of extrapolation techniques for the short-term prediction of rain amounts. *Atmos.-Ocean*, **19**, 54–65.

Turner, B. J., I. Zawadzki, and U. Germann, 2004: Predictability of precipitation from continental radar images. Part III: Operational nowcasting implementation (MAPLE). *J. Appl. Meteor.*, **43**, 231–248.

Tuttle, J. D., and G. B. Foote, 1990: Determination of the boundary layer airflow from a single Doppler radar. *J. Atmos. Oceanic Technol.*, **7**, 218–232.

Ulichney, R. A., 1988: Dithering with blue noise. *Proc. IEEE*, **76**, 56–79.

Venugopal, V., E. Foufoula-Georgiou, and V. Sapozhnikov, 1999: Evidence of dynamic scaling in space–time rainfall. *J. Geophys. Res.,* **104** (D24), 31 599–31 610.

Van Horne, M. P., E. R. Vivoni, D. Entekhabi, R. N. Hoffman, and C. Grassotti, 2006: Evaluating the effects of image filtering in short-term radar rainfall forecasting for hydrological applications. *Meteor. Appl.*, **13**, 289–303.

Vivoni, E. R., D. Entekhabi, and R. N. Hoffman, 2007: Error propagation of radar rainfall nowcasting fields through a fully distributed flood forecasting model. *J. Appl. Meteor. Climatol.*, **46**, 932–940.

Wang, Y. T., and V. Chandrasekar, 2009: Algorithm for estimation of the specific differential phase. *J. Atmos. Oceanic Technol.*, **26**, 2565–2578.

Wang, Y. T., and V. Chandrasekar, 2010: Quantitative precipitation estimation in the CASA X-band dual-polarization radar network. *J. Atmos. Oceanic Technol.*, **27**, 1665–1676.

Walser, A., D. Lüthi, and C. Schar, 2004: Predictability of precipitation in a cloud-resolving model. *Mon. Wea. Rev.,* **132,** 560–577.

Weisman, M. L., and J. B. Klemp, 1986: Characteristics of isolated convective storms. *Mesoscale Meteorology and Forecasting*, P. S. Ray, Ed., Amer. Meteor. Soc., 331–358.

Wesson, S. M., and G. G. S. Pegram, 2006: Improved radar rainfall estimation at ground level. *Nat. Hazards Earth Syst. Sci.*, **6**, 323–342.

Weygandt, S. S., A. F. Loughe, S. G. Benjamin, J. L. Mahoney, 2004: Scale sensitivities in model precipitation skill scores during IHOP. Preprints, *22nd Conf. on Severe Local Storms*, Hyannis, MA, Amer. Meteor. Soc., 16A.8. [Available online at: http://ams.confex.com/ams/pdfpapers/81986.pdf].

Weygandt, S. S., T. G. Smirnova, S. G. Benjamin, K. J. Brundage, S. R. Sahm, C. R. Alexander, and B. E. Schwartz, 2009: The High Resolution Rapid Refresh (HRRR): An hourly updated convection resolving model utilizing radar reflectivity assimilation from the RUC/RR. Preprints, *23rd Conf. on Weather Analysis and Forecasting/19th Conf. on Numerical Weather Prediction*, Omaha, NE, Amer. Meteor. Soc., 15A.6.

Whittaker, E. T., 1915: On the functions which are represented by the expansions of the interpolation theory. *Proc. Roy. Soc. Edinburgh*, **35A**, 181–194.

Wilks, D. S., 2006: *Statistical Methods in the Atmospheric Sciences,* 2nd ed. Elsevier Academic Press, 627 pp.

Wilson, J. W., 1966: Movement and predictability of radar echoes. *Final Report 7471–204*. The Travelers Weather Research Center, Hartford, CT.

Wilson, J. W., N. A. Cook, C. K. Mueller, J. Sun, and M. Dixon, 1998: Nowcasting thunderstorms: A status report. *Bull. Am. Meteor. Soc.*, **79**, 2079–2099.

Wilson, J. W., 2004: Precipitation nowcasting: Past, present, and future. Preprints, *Sixth Int. Symp. of Hydrological Applications of Weather Radar,* Melbourne, Australia, Amer. Meteor. Soc.

Wilson, J. W., E. E. Ebert, T. R. Saxen, R. D. Roberts, C. K. Mueller, M. Sleigh, C. E. Pierce, and A. Seed, 2004: Sydney 2000 Forecast Demonstration Project: Convective storm nowcasting. *Wea. Forecasting*, **19**, 131–150.

Wilson, J. W., R. Roberts, and J. Sun, 2009: Nowcasting challenges during the Beijing Olympics: Successes, failures and implications for future nowcasting systems. Preprints, *34th Conf. on Radar Meteorology*, Williamsburg, VA, Amer. Meteor. Soc., 3B.2.

Wolfson, M. M., B. E. Forman, R. G. Hallowell and M. P. Moore, 1999: The growth and decay storm tracker. Preprints, *Eighth Conf. on Aviation, Range, and Aerospace Meteorology*, Dallas, TX, Amer. Meteor. Soc., 58–62.

Wolfson, M. M., W. J. Dupree, R. M. Rasmussen, M. Steiner, S. G. Benjamin, and S. S. Weygandt, 2008: Consolidated Storm Prediction for Aviation (CoSPA). Preprints, *13th Conf. on Aviation, Range, and Aerospace Meteorology*, New Orleans, LA, Amer. Meteor. Soc., J6.5. [Available online at http://ams.confex.com/ams/pdfpapers/132981.pdf].

Xu, G., and V. Chandrasekar, 2005: Radar storm motion estimation and beyond: A spectral algorithm and radar observation based dynamic model, *Extended Abstracts, World Meteorological Organization Symp. on Nowcasting*, Toulouse, France, World Weather Research Programme, 2.41.

Xu, K., C. K. Wikle, and N. I. Fox, 2005: A kernel-based spatio-temporal dynamical model for nowcasting weather radar reflectivities. *J. Amer. Stat. Soc.*, **100**, 1134–1144.

Zawadzki, I., 1973: Statistical properties of precipitation patterns. *J. Appl. Meteor.*, **12**, 459–472.

Zawadzki, I., J. Morneau, and R. Laprise, 1994: Predictability of precipitation patterns: An operational approach. *J. Appl. Meteor.*, **33**, 1562–1571.

Zhang, R., and X. Shen, 2008: On the development of the GRAPES—a new generation of the national operational NWP system in China. *Chinese Sci. Bull.*, **53**, 3429–3432.

Zink, M., D. Westbrook, S. Abdallah, B. Horling, V. Lakamraju, E. Lyons, V. Manfredi, J. Kurose, and K. Hondl, 2005: Meteorological command and control: An end-to-end architecture for a hazardous weather detection sensor network. *Proc. 2005 Workshop End-to-end, Sense-and-respond Systems, Applications and Services*, Seattle, WA, USENIX Assoc., 37–42.

Zwillinger, D., 1997: *Handbook of Differential Equations,* 3rd ed. Academic Press, 801 pp.